ANALYSIS AND DESIGN
OF
LINEAR INDUCTION MACHINES

Thesis presented to the University of London
for the award of the degree of Ph.D.

By

Jafar Hamid Hasan ALWASH, B.Sc. (Eng.) Hons.

Department of Electrical Engineering,
Imperial College of Science and Technology,
London, S. W. 7.

August, 1972

Abstract

The thesis begins with a study of a new form of tubular motor in which the flux takes transverse rather than longitudinal paths. An appropriate theory using multi-layer techniques in cylindrical coordinates is presented.

The subsequent chapters present new forms of analysis for linear and arc-stator induction machines. In chapter 4 a form of analysis using permeance and excitation harmonics is presented. A multi-layer theory applicable to thick plate linear motors is given in chapter 5. This theory uses excitation harmonics in both the longitudinal and transverse directions. All the theories given in the thesis are supported by results from experimental models.

Acknowledgements

The author wishes to express his sincere gratitude to his Supervisor, Dr. J.F. Eastham, for his help, guidance and encouragement.

He also wishes to thank Dr. E.M. Freeman for his guidance during the first year of the work and his continuous support and helpful discussion.

Thanks are also due to the workshop staff, in particular Mr. C. Johnson, for considerable help during the construction of experimental apparatus.

Thanks are due to the Baghdad University for providing the opportunity to take up the award of the Calouste Gulbenkian Foundation.

Finally, the author gratefully acknowledges helpful suggestions from so many fellow students and members of staff, too numerous to name individually.

INDEX

List of principal symbols

E	=	electrical field strength, V/m
H	=	magnetic field strength, A/m
f	=	supply frequency, Hz.
J'	=	amplitude of line current density, J_θ, A/m
λ	=	wave length of exciting wave, in the direction of field travel, m
k	=	wave length factor = $2\pi/\lambda$
Z_{in}	=	input surface impedance, Ω
ω	=	$2\pi f$
s	=	slip
r,z,θ	=	subscripts for cylindrical coordinates
ρ	=	resistivity
σ	=	conductivity
N	=	total number of layers considered in the mathematical models of chapters 2 and 5
P_{in}	=	power input per unit length in the direction of field travel, W/m
F_a	=	axial force per metre of axial length, N/m
I_n, K_n	=	modified Bessel functions of general complex argument
r_g	=	current sheet radius in cylindrical geometry analysis, m

θ,g z,g θ,m z,m) double subscripts, the first identifies
$\theta,N-1$ $z,N-1$ $\theta,m-1$ $z,m-1$) the cylindrical coordinates and the
$\theta,1$ $z,1$ z,s θ,s) second the region considered

N_1	=	effective number of turns per pole per phase at the working pole pitch

p_1	=	pole pitch in the axial direction, m
$\hat{I}$	=	peak of phase current, A
$\hat{H}_z, \hat{E}_z$, $\hat{H}_\theta, \hat{E}_\theta$	=	the peak value of the respective quantities, which is a function of coordinate r only
n,m	=	integers
B	=	magnetic flux density
μ_o	=	permeability of free space
μ_r	=	relative permeability
μ	=	$\mu_o \mu_r$
x,y,z	=	subscripts for Cartesian coordinates
P_w	=	the winding pole pitch, m
P_n	=	the pole pitch, for the n^{th} excitation harmonic
k_p	=	total number of pole pairs around the machine
q	=	the number of pole pairs in the excited region
N_p	=	2q
V	=	rotor speed, m/sec.
V_S	=	$2P_w f$ = synchronous speed, m/sec.
ρ_r	=	rotor surface resistivity, Ω
ℓ_r	=	rotor surface leakage inductance, H
B_g	=	air-gap flux density, T
P_o	=	pole pitch outside the excited region, m
B_{go}	=	air-gap flux density outside the excited region, m
ρ_{rn}, V_{sn}, ℓ_{rn}, B_{gn}, S_n	=	the values of the respective quantities, for the n^{th} excitation harmonic

g = the magnetic air-gap, for the uniform gap machine, m

g_i, g_o = the magnetic air-gap, inside and outside the excited region respectively, m

$\beta = \frac{g_o}{g_i}$ = air-gap ratio for a stepped gap machine

$B_{g.s.s}$ = the steady state value of B_g

R = the rotor radius, m

$\hat{J}_S$ = amplitude of stator line current density, A/m

$\hat{J}_R$ = amplitude of rotor line current density, A/m

$\hat{J}_{Ro}$ = the value of $\hat{J}_R$ outside the excited region

N_2 = the total number of bars in the squirrel-cage rotor

h = rotor width, m

G = goodness factor

$\mathcal{R}(\;)$ = real part of the quantity enclosed in brackets

$\mathcal{J}(\;)$ = imaginary part of the quantity enclosed in brackets

CHAPTER ONE

GENERAL INTRODUCTION

The outstanding feature of an induction motor is that it can produce force on a movable secondary without either physical or electrical contact being necessary. It is this feature alone which has led to its immense popularity as a rotating machine, in which form it has a high power to weight ratio and efficiency.

Linear forms of induction motor have been known for perhaps the last 70 years. They have, however, only recently found favour. This is mainly due to a shifting of emphasis in recent times from efficiency <u>per se</u> to the assessment of overall system economics. This assessment includes such factors as reliability and flexibility of application.

Linear motors may be loosely divided into three main groups; force machines, energy machines and power machines. The criteria by which the quality of the motor is judged are different for each division. In the force machine case, that is, a machine which produces force on a mechanism with either a limited or no movement, the efficiency is clearly virtually zero since the output power is small. Accordingly the quality of such machines is judged in terms of quantities like force per weight or force per input power.

Force machines have been manufactured commercially for a number of years, notably in the United States, Sweden and in this country by Lintrol Ltd., who make a large range of linear stators. The range of application of these machines has been extremely diverse; probably their widest use has been in a crane drive system, although many apt uses in the general materials handling field have also been found.

The conventional tubular form of linear motor is commonly used for force applications. This form of construction is described in chapter 2. The chapter goes on to show that the core flux density is a design limitation in the case of conventional tubular motors and further describes how the coil arrangements can be modified so that the situation is alleviated.

An energy machine is employed to produce kinetic energy. The range of application of these machines has so far been limited. However, two large energy machines are at present in use in this country. One machines is in use at the East Kilbride National Engineering Laboratory as a rope snatch tester. The second is used to accelerate test vehicles for crash test purposes at the Motor Industry Research Association's Laboratory at Nuneaton. Both these machines, each of which requires a supply of about 2 MVA, have been extremely successful in operation providing reliable and repeatable test conditions.

The range of application of power machines is almost wholly confined to transport systems. One of the first suggested applications of a linear machine was its use in a railway. This scheme was the idea of the Mayor of Pittsburgh in 1890. At the present time intensive research into hovercraft running on prepared tracks is going on in many countries, principally in the U.S.A., Japan, Germany, France and the United Kingdom. Most of the schemes use linear induction machines as the drive system.

Whilst the range of linear motor sizes and shapes is extremely large, the analytical treatment required for design purposes is, of course, common to most of them. To date the majority of the analysis used for design purposes has been performed on what may be termed a one-dimensional basis. That is to say, the width of the machine has been assumed to be infinite so that the effects in the plane transverse to motion have been ignored. In addition, tangential components of the air-gap field have been assumed to be zero. In some design procedures the leakage reactance of the secondary has been ignored, in others the effect has been included, but only by use of an approximate method for calculating the parameter. Chapter 3 presents a simple harmonic approach to the analysis which is supported by experimental findings. The analysis is strictly one-dimensional. It includes leakage reactance as a parameter, but again, as in the earlier analysis, an approximation to this quantity is necessary. However, the method is simple in computation and application, and it is hoped that it will be of value for design purposes.

The treatment given for the effects at the exit-edge of the machine is extremely approximate in this method. However, chapter 4 confirms the value of these approximations by using again in one-dimensional form a new analysis using permeance harmonic techniques. This analysis will be of value in assessing some proposed techniques of gap-shaping at the exit-edge of linear motors.

In chapter 5, an analysis is presented which uses multi-layer theory to predict the performance of a thick plate linear motor. This analysis is two-dimensional; it includes the effects in plane transverse to the motion. This approach is the most rigorous in the thesis and it gives extremely good results. It is hoped that it could in future work be used to find the effective rotor parameters so that tables could be computed to facilitate the design process.

CHAPTER TWO

TRANSVERSE FLUX TUBULAR MOTORS

2.1 Introduction

The form of a conventional tubular motor may be explained with the aid of Fig. 2.1 [2.1]. Fig. 2.1a shows the instantaneous pole pattern of a planar linear motor. If this pattern is rolled about an axis parallel to its line of action the pole pattern of a tubular motor is produced, as shown at Fig. 2.1b.

The primary coil construction may be explained in a similar manner with the aid of Fig. 2.2. Fig. 2.2a shows one phase winding of the planar motor. In order to convert this into the tubular form it is rolled into a cylindrical shape by joining AA to BB and omitting the end windings. Each conductor of the original winding forms one circular coil, as shown in Fig. 2.2b.

It is shown in an earlier paper [2.2] that transverse flux linear motors have advantage over the more conventional type of flat machine, especially in that the flux density of a core of a given thickness is independent of the pole pitch and these machines are specially advantageous in high speed motors designed to run from 50 Hz supplies.

It is the object of this chapter to examine some new transverse

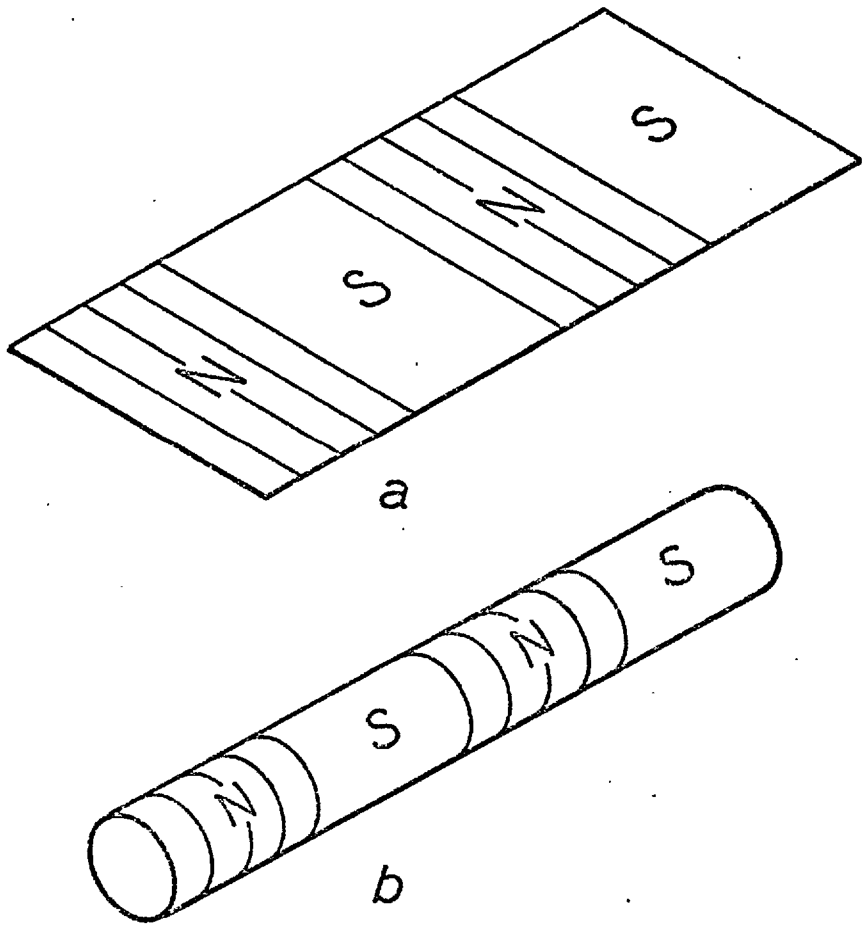

Fig. 2.1 The development of a conventional tubular motor

(a) Instantaneous pole pattern of a planar motor
(b) The planar motor rolled to form a tube

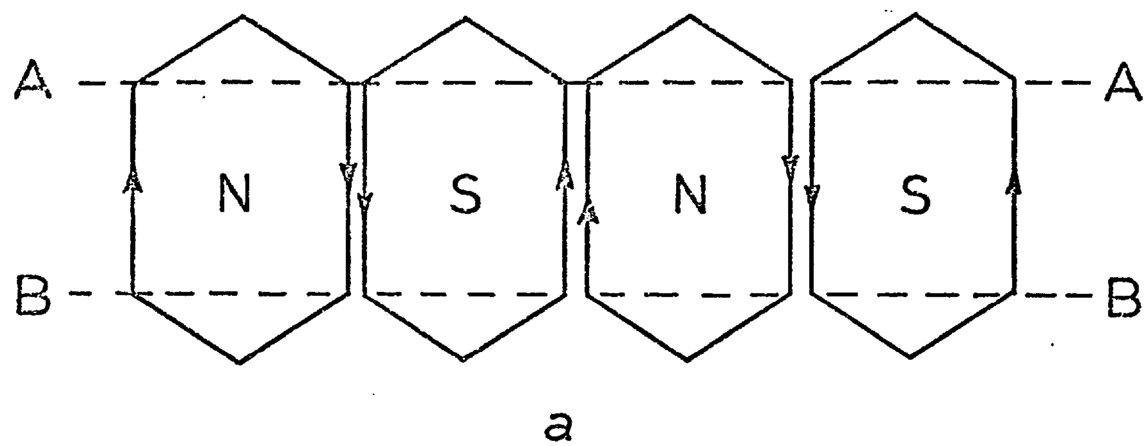

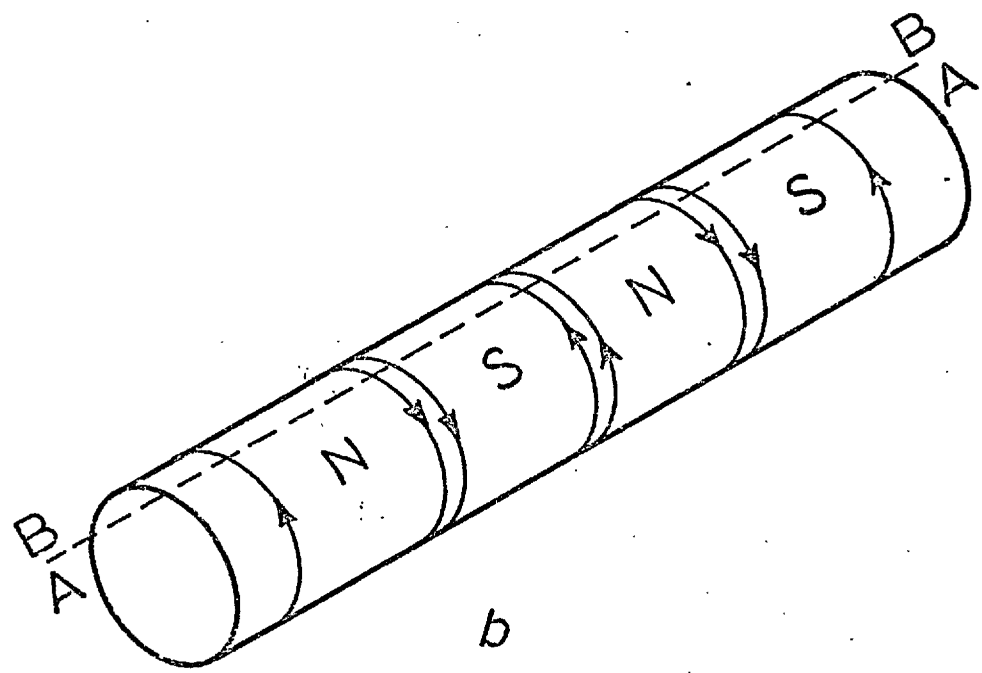

Fig. 2.2 Primary coil construction for one phase of a conventional tubular motor

(a) Coil structure of a planar motor
(b) Coil structure of a tubular motor

flux machines in which the construction is tubular in that the primary coils completely surround the secondary conductor, not so much because they may be required to have large pole pitches but because the basic change of magnetic circuit axis enables a simpler form of laminated core to be used.

So far commercial tubular motors have been restricted to small sizes and low powers so that a solid steel core could be used without incurring severe penalties. With expansion of the range of commercially manufactured linear motors it is now important to investigate the design of high powered tubular motors and it is hoped that this chapter is seen to represent a first step in the right direction.

2.2 The new machines

2.2.1 Primary winding arrangements using coils

The construction of the new machines may be explained by first considering a flat structure with two windings sets. This is shown at Fig. 2.3. As in the case of the conventional machine this can be rolled to form a cylinder. However, this time the end windings are not omitted so that CC lies on DD. On the first coils of the winding sets one coil side is shown by a heavy line. When the windings are rolled up the points XX' will coincide. Thus, since the points YY' are also

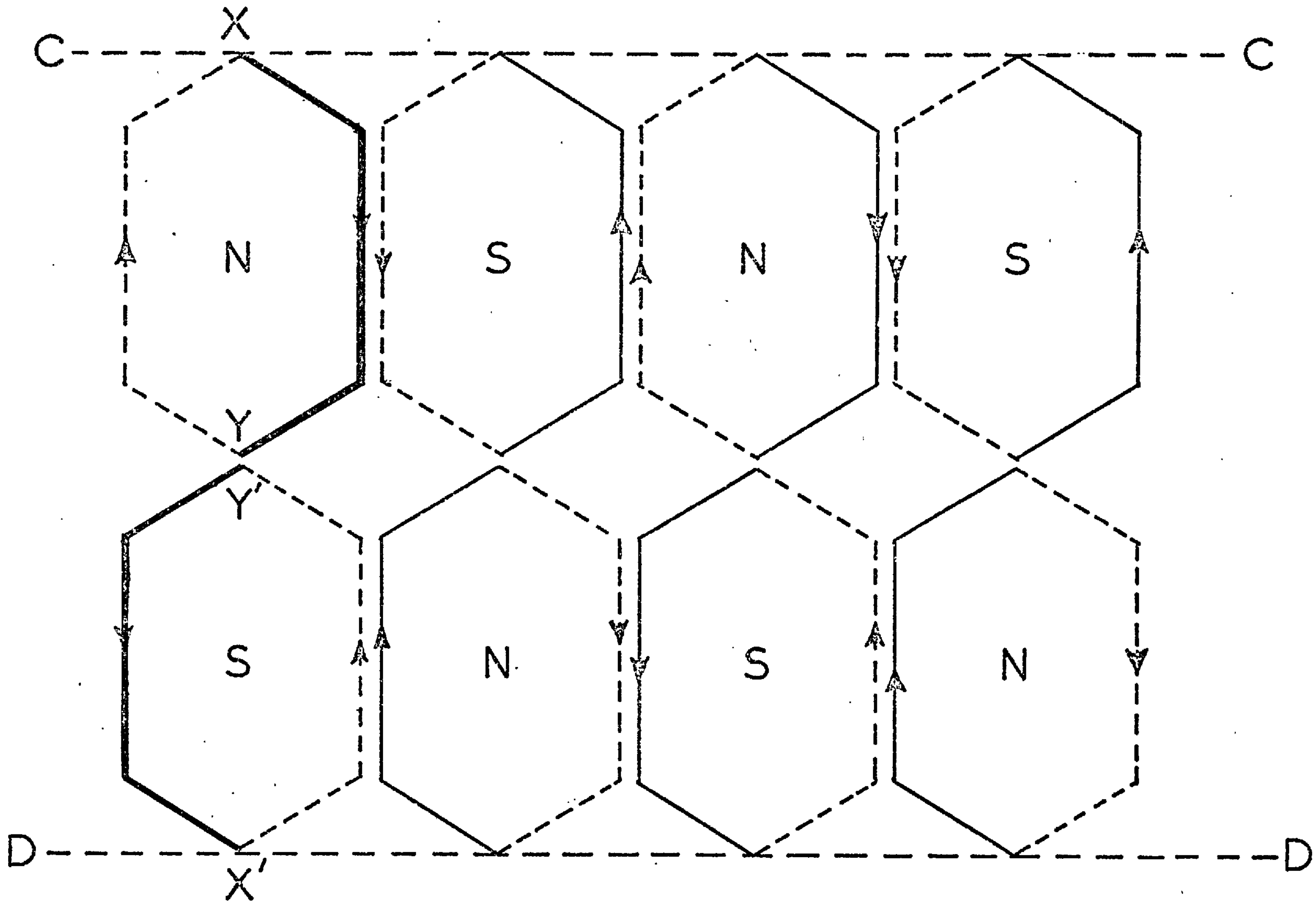

Fig. 2.3 Illustrating the development of the primary winding structure, using coils, of one phase of the transverse flux machine.

coincident the winding conductors XY and Y'X' can form a coil in the tubular form. This coil will be skewed with respect to the tube axis. Similar coils can be formed by using, in pairs, the conductors shown in plain lines. These coils form one layer of the final winding. The dotted conductors again taken together in pairs form the second winding layer which is skewed in the opposite direction to the first. Fig. 2.4 shows a pair of skewed coils suitable for the first coil of the winding layers.

The windings so far illustrated are single phase. Polyphase windings can of course be constructed following the same princ-iples. Fig. 2.5 shows a one slot per pole and phase version in which the virtual coil pitch is two-thirds of a pole pitch. It will be appreciated that any virtual double layer winding may be formed using this coil construction. By the technique used in developing these new windings it will be understood that they correspond with a combination of two conventional windings so arranged that the "end turns" are coupled more closely with the secondary. In terms of surface windings it will be noted that whilst the system has been described in terms of original windings having coils of conventional shape, any original coil shape is in fact possible.

2.2.2 Primary winding arrangements using spirals

The arrangement of Fig. 2.3 uses conventionally shaped coils. Fig. 2.6 shows in dotted lines a similar construction in which the coils are diamond shaped. The plain line marked AH on this

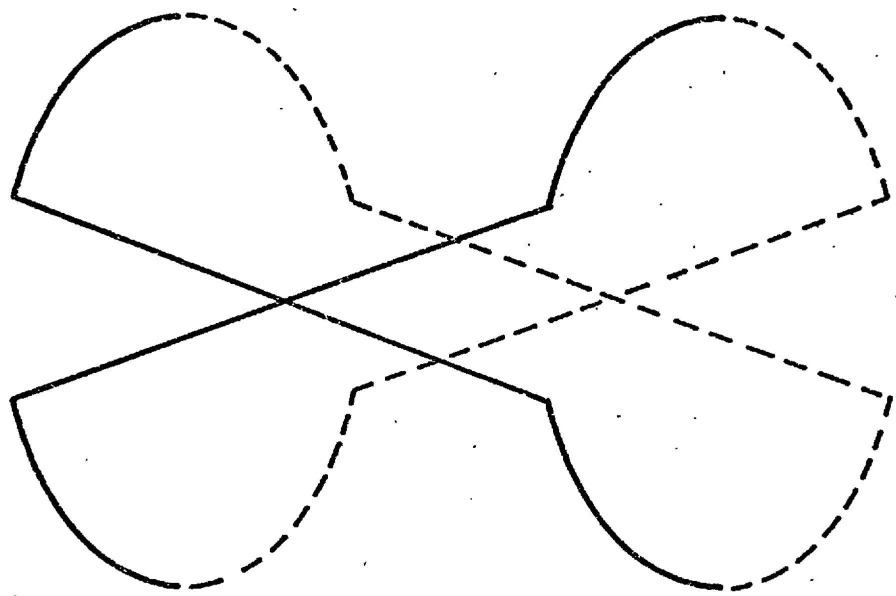

Fig. 2.4 Skewed coils used to construct the transverse flux motor primary.

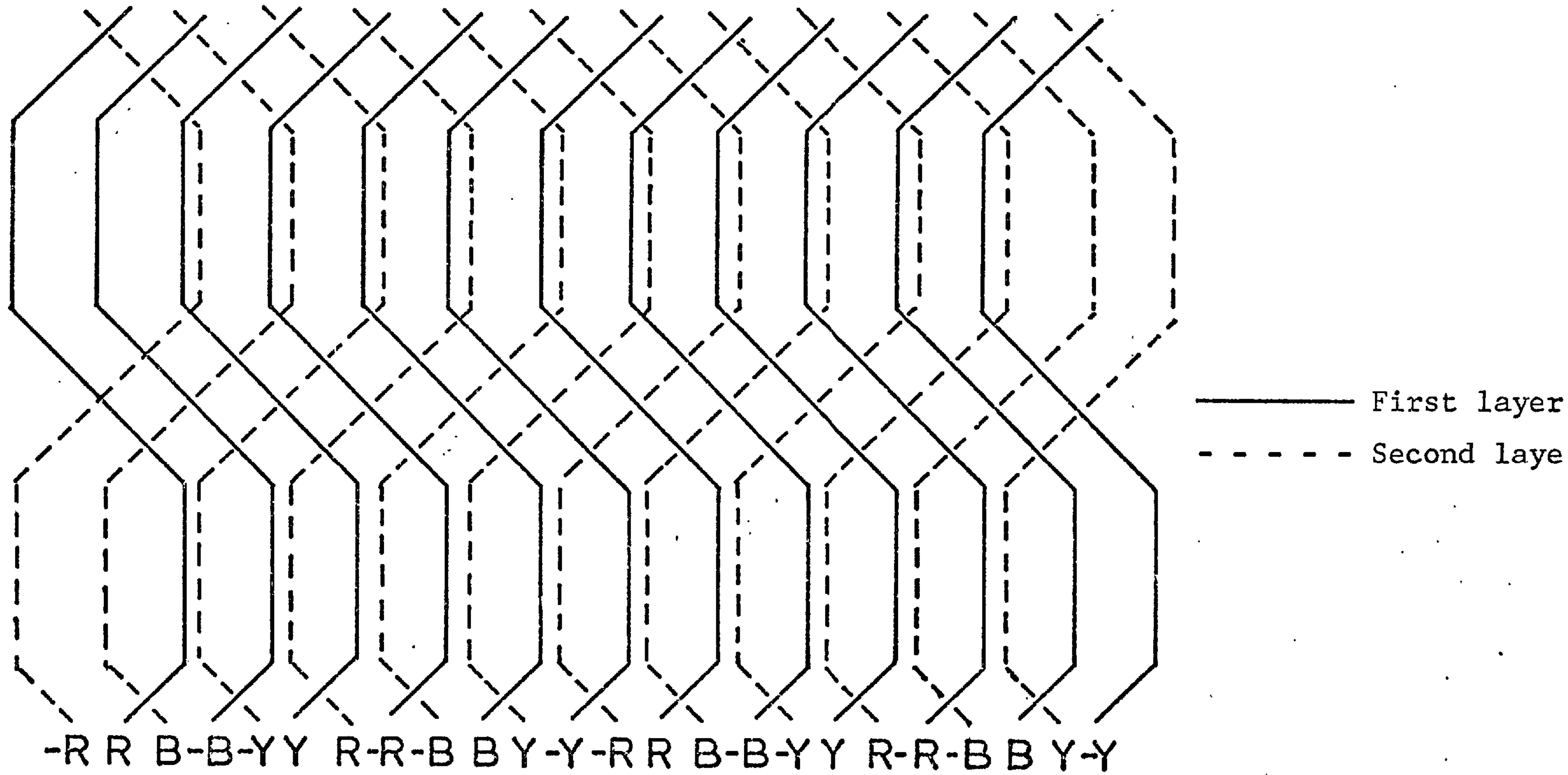

Fig. 2.5 A three phase version of the winding using coils

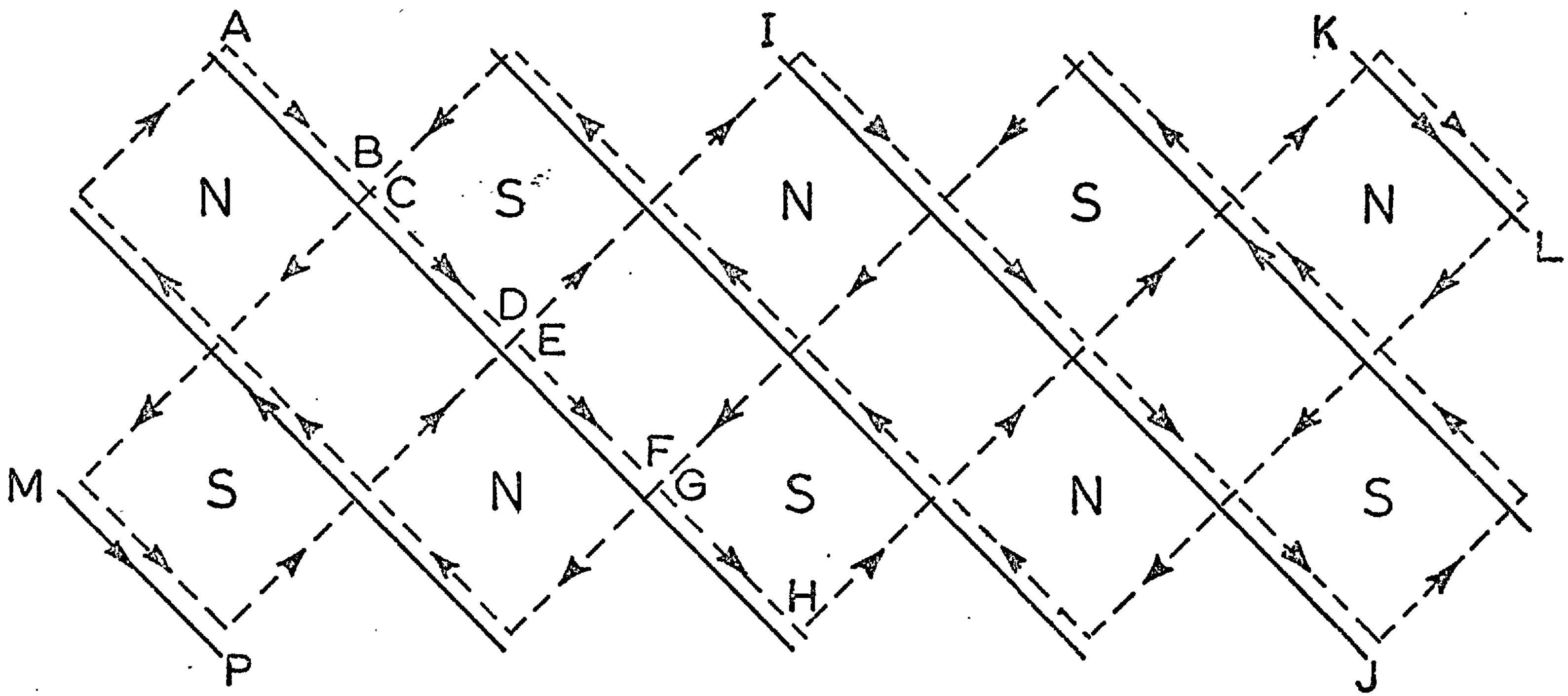

Fig. 2.6 Development of a double helical winding

figure represents a conductor which could replace the coil sides marked A, B; C, D; E, F; G, H. The conductor marked IJ could similarly replace a further four coil sides. When the arrangement is rolled into tubular form H lies on I. This means that AHIJ could be a single conductor. This conductor is helical in shape since it is at the same angle with respect to an axial line at all points in its travel. By the same argument the same helical conductor could be extended at each end to form MP and KL. A second helix of the same angle and pitch but with its current oppositely directed could replace further coil sides as indicated on the diagram. All the coil sides which slope down from left to right have now been replaced; the pair of helices so formed comprise the first winding layer. The coil sides which slope down from right to left may be replaced by a second pair of helical conductors. These will have the same pitch as the first pair but will be angled in the opposite direction to form the second winding layer.

Polyphase versions of the windings may of course be arranged. Fig. 2.7 shows an unrolled 3 phase configuration, the two layers to be superimposed are shown on different diagrams for clarity. Fig. 2.8 shows a sketch of the conductor shape for one layer. The winding is in the form of a six start thread.

The spiral windings have been described in terms of single

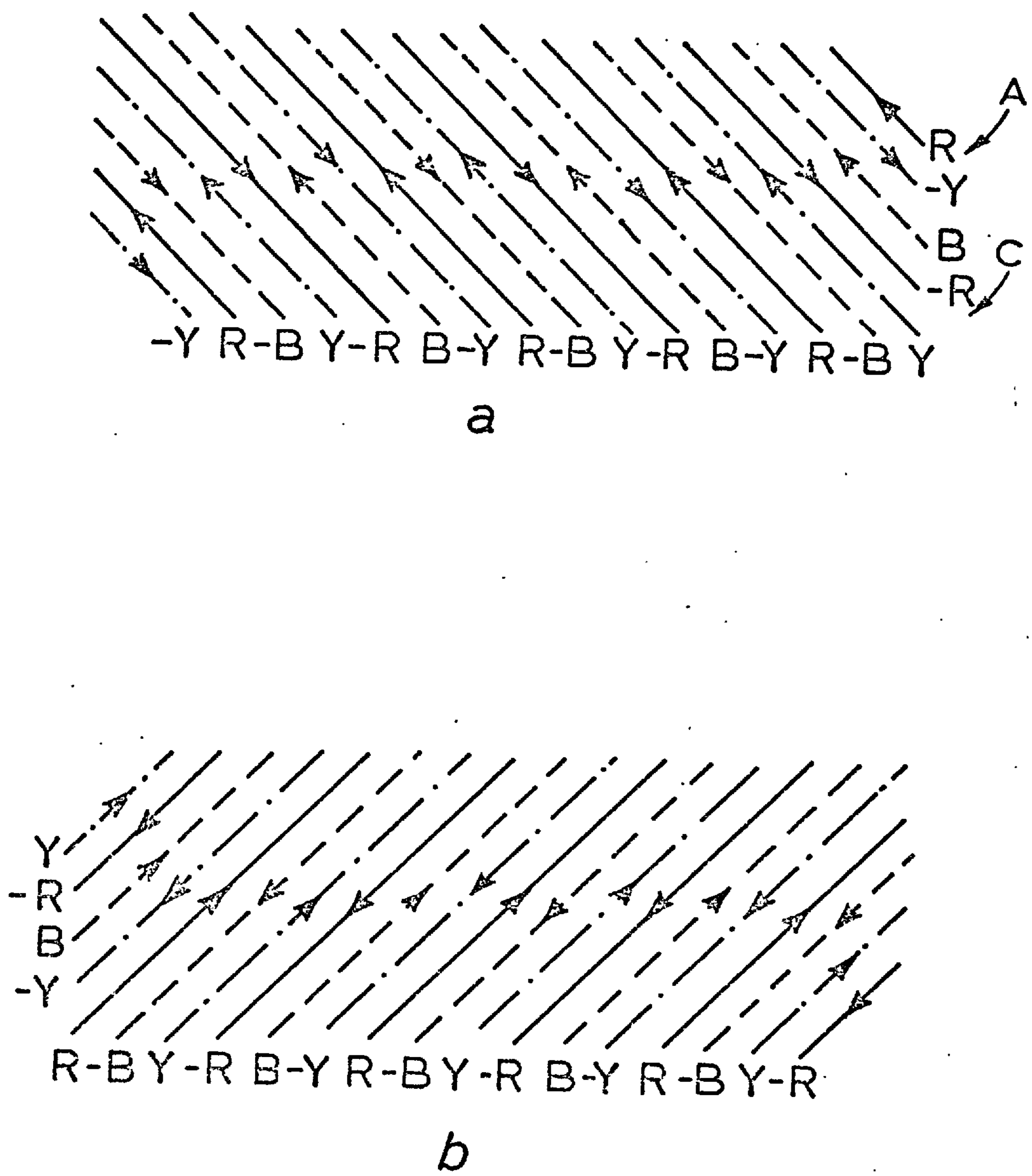

<u>Fig. 2.7</u> Three phase helical winding arrangement

(a) First layer
(b) Second layer

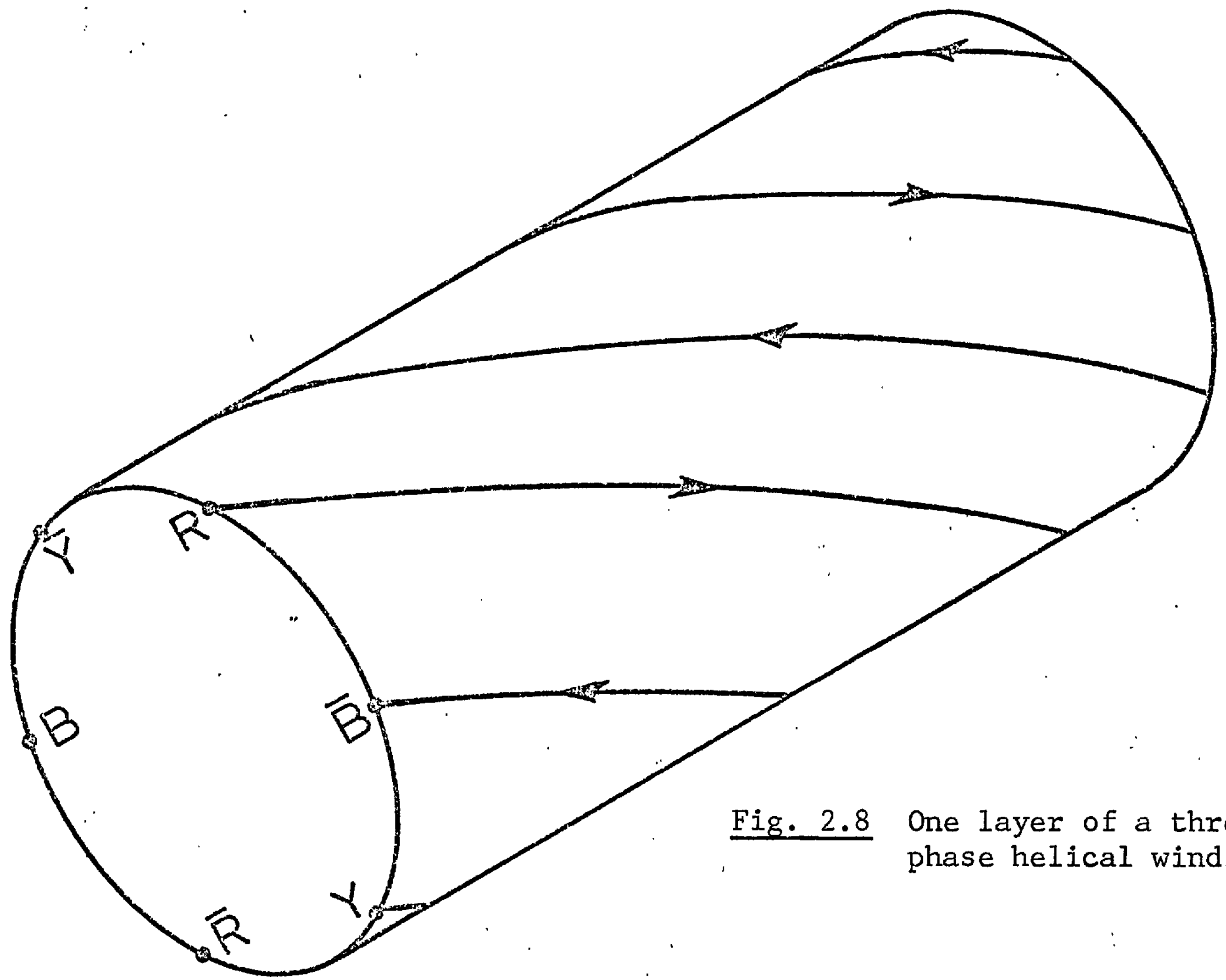

Fig. 2.8 One layer of a three phase helical winding

conductors. The construction using phase bands of conductors to increase the effective turn number is the same but in this case the conductors must be inter-connected at each end of the machine; each conductor as it emerges from say A in the red phase on Fig. 2.7a must be connected to a conductor at C. This leads to two possibilities. First, the conductors may be formed in spirals and then each individual wire connected, or secondly, a long coil can be made and twisted to produce both the negative and the positive conductors of one winding layer.

The spiral winding has another feature which could be of value; if only one winding layer is used, then the secondary will be subjected to a torque as well as a translatory force.

The windings described in Sections 2.2.1 and 2.2.2. have two poles in the circumferential direction. The system is not limited to these cases. By starting with say four winding sets on Fig. 2.3, machines with four poles in the circumferential direction can be produced.

2.2.3 The magnetic circuit

Bearing in mind the original winding of Fig. 2.3 it will be noted that the pole flux enters the tube over one part of the periphery and leaves over a diametrically opposite area. At any one section the flux lines appear as shown in Fig. 2.9. It will be seen that the flux paths in the machine may now be restricted to radial and circumferential directions, that is, the flux lies in planes transverse to the direction of motion, as did the flux in the planar machines described in ref. (2.2). Simple disc laminations may be used for the secondary. If a surface winding construction is to be used, annular laminations suffice for the primary.

The use of surface windings implies a larger magnetic gap. However, it is possible to provide a virtual "tooth and slot" structure in the primary iron circuit. Fig. 2.10 shows a constructional drawing corresponding to a section of the diagram of Fig. 2.5. Here, in the sloping portions, the coils are in close proximity. Thus if the coil width remains the same, spaces are left in between the straight portions. This construction of course corresponds with normal practice in machine windings.

The shape of lamination required to form the primary magnetic circuit is shown in Fig. 2.11a. A general view of the construction is shown in Fig. 2.11b, the windings are omitted in this diagram. It will be appreciated, however, that the sloping portions of the windings fit in the arcs labelled X-X on Fig. 2.11a with the straight portions lying between the lamination packets.

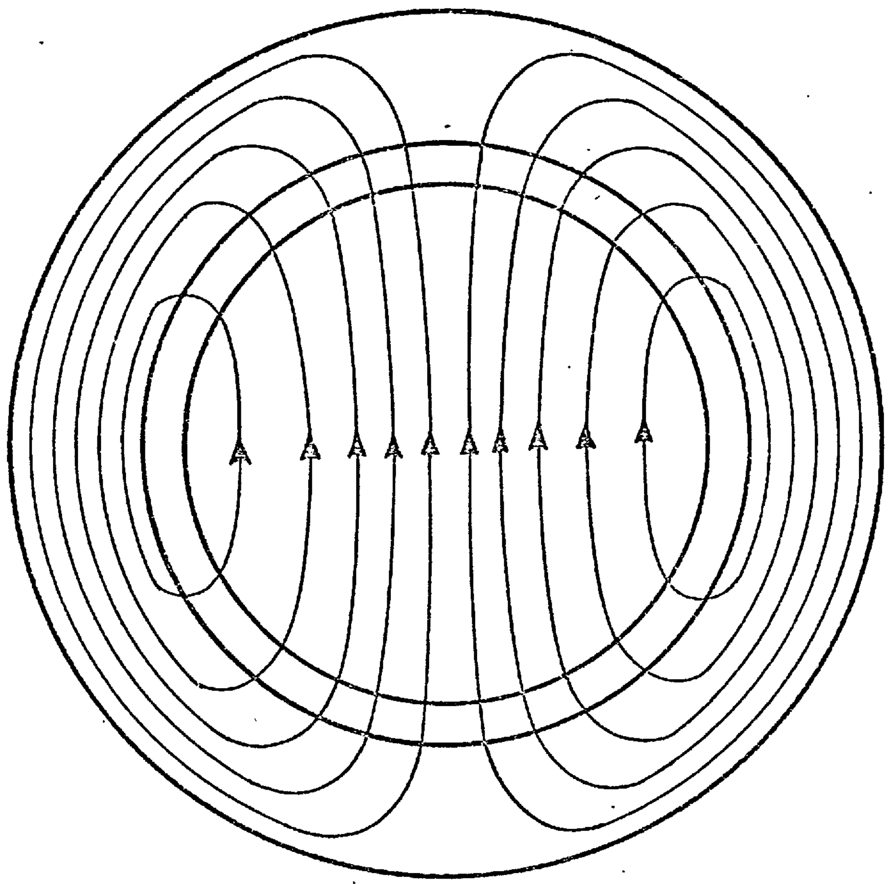

Fig. 2.9 Pulsating "two-pole" transverse flux distribution

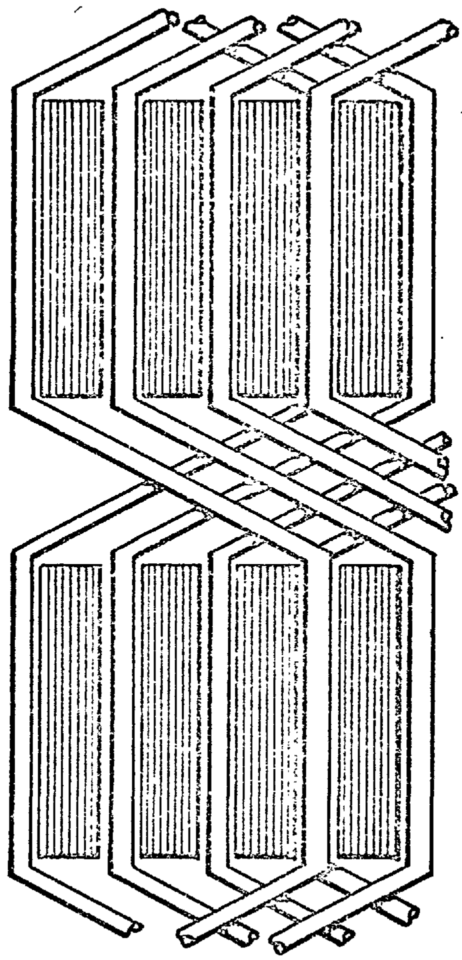

Fig. 2.10 Primary lamination structure for the winding of Fig. 2.5

Fig. 2.11 Transverse flux motor primary lamination structure

(a) Lamination shape to form the magnetic circuit of (b)
(b) Magnetic circuit
(c) Lamination shape if further laminations are used between the lamination packets of (b)

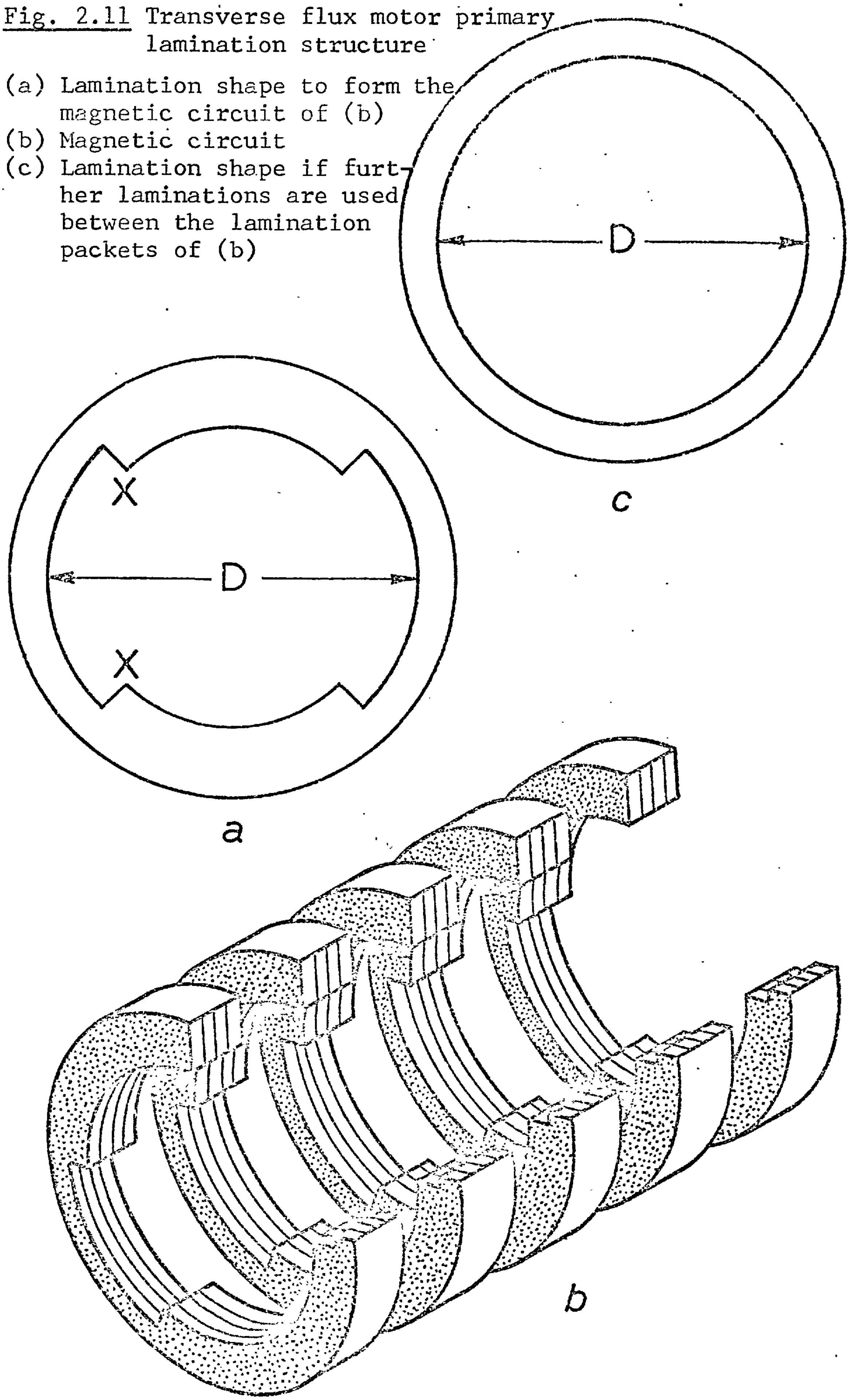

The construction of Fig. 2.11b could be modified by including further annular packets of laminations between those shown. These would be dimensioned as indicated at Fig. 2.11c. They would assist in carrying the circumferential flux. This would enable the outside diameter of the machine to be reduced.

The above configurations have been developed in terms of the primary arrangement which uses coils, however the arguments also apply to the spiral case.

The magnetic circuits so far suggested for the new machines use laminations transverse to the direction of motion. Other lamination systems are possible, for example Fig. 2.12 shows a machine in which axial lamination planes are used for the secondary magnetic circuit. Clearly the use of this hybrid system enables the flux to take either axial or transverse secondary paths, or both. Tubular actuators in industrial use commonly have solid steel secondary circuits. These again provide both axial and transverse flux paths. Hybrid secondary magnetic circuits may be used either with machines with no primary iron circuit or with the transversely laminated circuits so far described. Hybrid primary circuits are also possible as shown at Fig. 2.13. In this arrangement slotted axial lamination packets are used to contain the primary winding. The annular punchings which surround the machine provide transverse flux

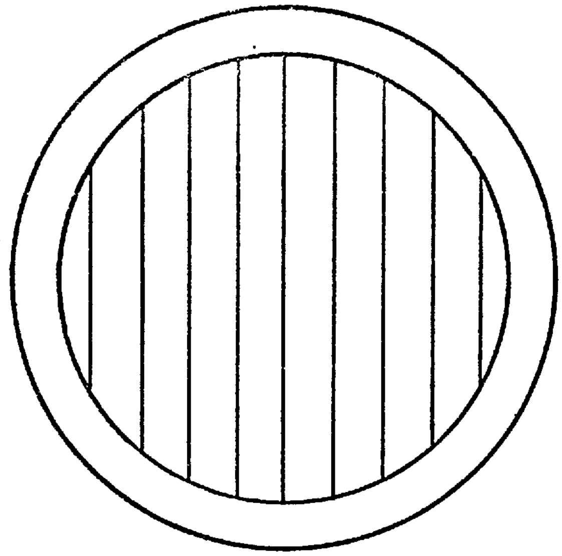

Fig. 2.12 Axial secondary laminations to provide both axial and transverse flux paths

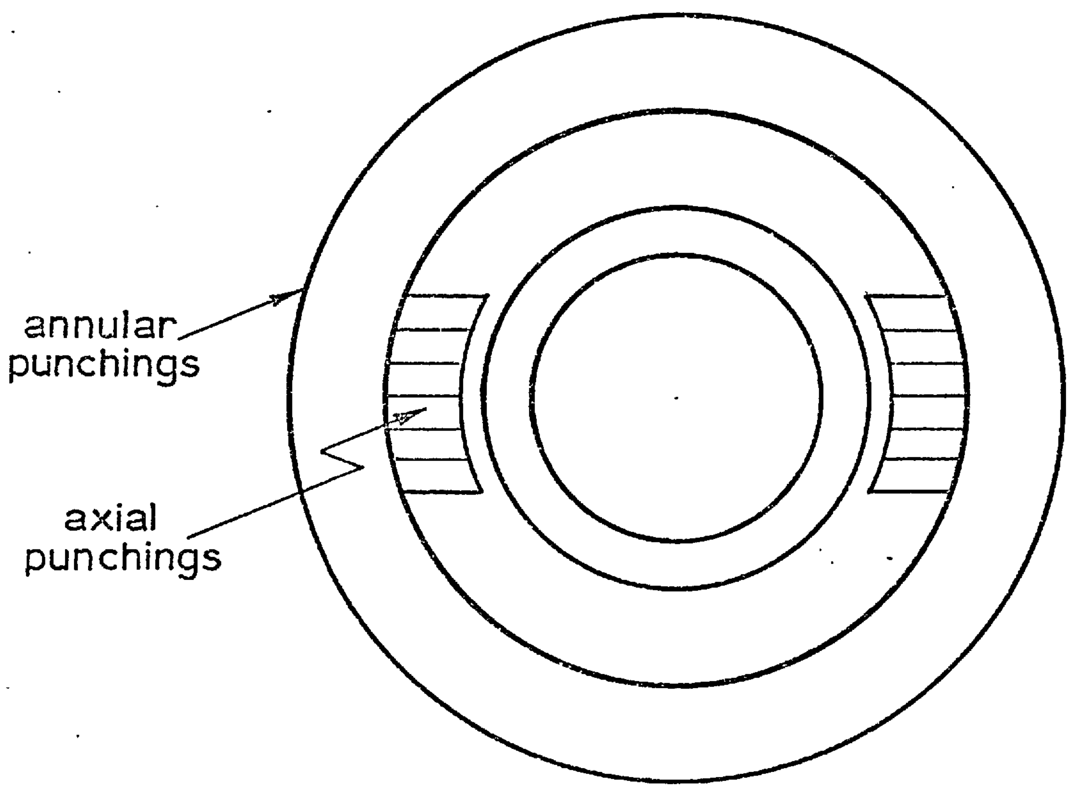

Fig. 2.13 Primary magnetic circuit with axial and transverse flux paths

paths. It is therefore possible for flux to take either transverse or axial paths.

2.3 A comparison between the new machines and conventional machines

In conventional tubular motors the electric circuits are perfect in that no axial currents exist. That is to say, the secondary currents have circular paths only and no end-turns are required in the primary winding. However, the magnetic circuit becomes more difficult. At any section of the tube the flux crosses the rotor conductor radially, and its direction is the same at all points on the periphery. Thus the flux from one pole of the machine must pass axially to the next pole and the area of the rotor magnetic circuit limits the pole flux. This limitation is severe when the pole pitch is long compared with the radius. The core flux limitation implies that the air-gap flux density must reduce as the pole-pitch increases.

In the new machines the flux has no axial component in the secondary core and the air-gap density is therefore independent of pole pitch. The flux passes transversely through the secondary as shown in Fig. 2.9 and no constriction is imposed on the flux path. The magnetic circuit is therefore improved. However, the electric circuits are inferior in the new machines. First the windings have virtual end-turns, that is the primary conductors have axial components.

Secondly, the rotor currents are constrained to paths of the form of those shown in Fig. 2.14. Therefore the apparent resistivity of the secondary viewed from the primary will be increased compared with that which would be obtained in the conventional case, due to extra path lengths involved.

Thus as far as the ratio of the forces produced at constant core flux is concerned, as the pole pitch increases there is a trade-off between a reduced gap-density on the one hand and an increased effective rotor resistance on the other. However, it was felt that the new machines should be better over a range of parameters and it was therefore considered to be worthwhile to test the machines both practically and analytically. In the result, as may be seen from the following sections, substantial increases in force can be produced.

2.4 Theoretical analysis

2.4.1 The primary current density

The primary winding considered consisted of two superimposed helical distributions, corresponding to the arrangement shown in Fig. 2.7. It is assumed that the windings produce perfect sinusoidal travelling waves.

The current density then consists of two components,

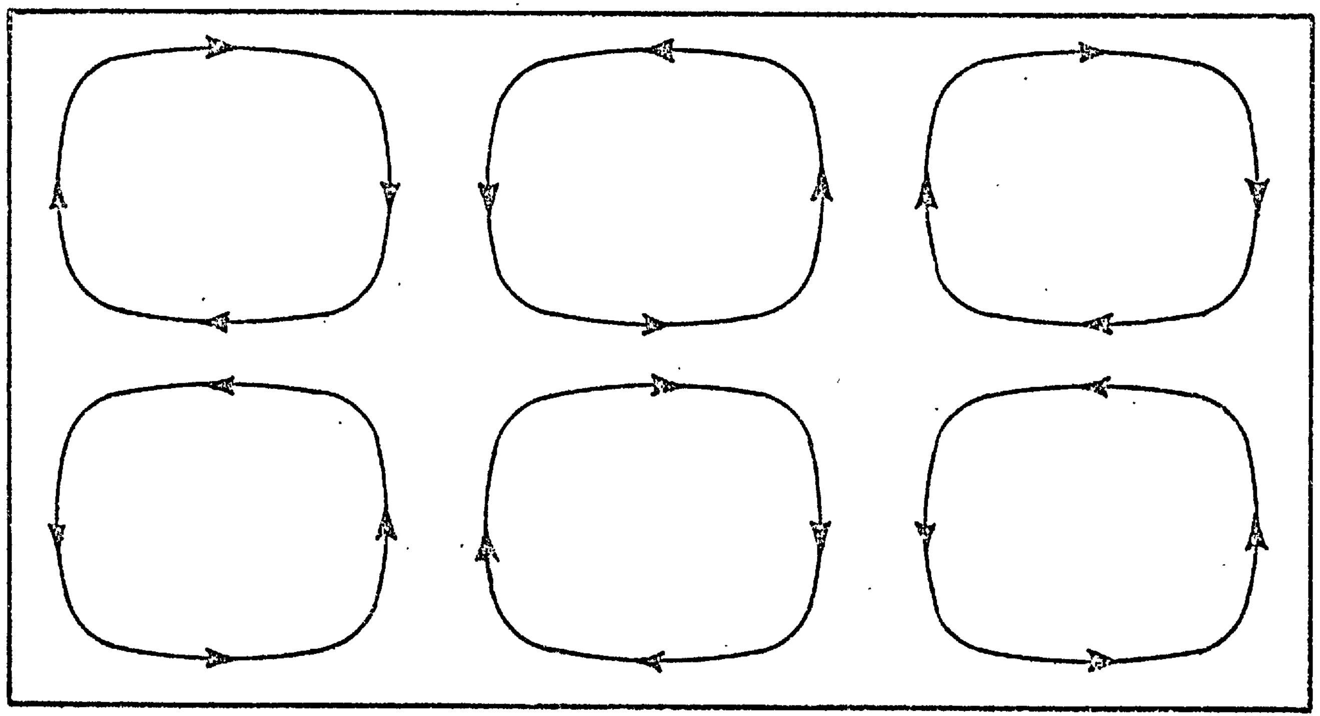

Fig. 2.14 Secondary current patterns in transverse flux tubular motors

$$J_1 = \mathcal{R}\left[\frac{N_1 \hat{I}}{2L} \exp(j\phi) \exp j(\omega t - kz + n\theta)\right]$$

$$J_2 = \mathcal{R}\left[\frac{N_1 \hat{I}}{2L} \exp j(\pi - \phi) \exp j(\omega t - kz - n\theta)\right]$$

where ϕ is the angle of the winding with respect to a line parallel to the motor axis and is given by,

$$\phi = \tan^{-1}\left(\frac{k r_g}{n}\right)$$

and $L = p_1 \sin \phi/3$

The resultant current density can be represented by two components,

$$J_z = \mathcal{R}[j J' \cos \phi \sin(n\theta) \exp j(\omega t - kz)]$$

$$J_\theta = \mathcal{R}[J' \sin \phi \cos(n\theta) \exp j(\omega t - kz)] \qquad \text{.............(2.1)}$$

where $J' = N_1 \hat{I}/L$ ....(2.2)

2.4.2 Mathematical model

A general multi-region problem is analysed. The model is taken to be a set of infinitely long concentric cylinders, with a radially infinitesimally thin and axially infinite current sheet excitation at radius r_g.

In order to simplify the problem it is assumed that the resistivity in the radial direction is infinite. In particular this can be taken to imply that any conducting region is perfectly laminated, by being constructed from infinitely thin insulated concentric cylinders. Displacement currents are assumed negligible and magnetic saturation is neglected.

Maxwell's equations for any region in the model are,

$$\text{curl } H = J \quad \ldots\ldots \quad (2.3) \qquad \text{curl } E = -\frac{\partial B}{\partial t} \quad \ldots\ldots \quad (2.4)$$

$$\text{div } B = 0 \quad \ldots\ldots \quad (2.5) \qquad \text{div } J = 0 \quad \ldots\ldots \quad (2.6)$$

$$\text{div } E = 0 \quad \ldots\ldots \quad (2.7) \qquad J = \sigma E \quad \ldots\ldots \quad (2.8)$$

$$B = \mu H \quad \ldots\ldots \quad (2.9)$$

and from the initial assumptions we have $J_r = 0$ ....(2.10)

The boundary conditions are:

(a) The radial flux density is continuous across a boundary

(b) The axial component of magnetic field strength is continuous across a boundary, but allowance must be made for the current sheet, in the manner shown in Section 2.4.4.

2.4.3 The field equations of a general region

As a first step in the analysis the field components of a general region are derived.

Assuming that all the fields vary as $\exp\left[j(\omega t - kz)\right]$ and omitting this factor for shortness, from all the field expressions that follow, we have from equations (2.1) and (2.8)

$$E_\theta = \hat{E}_\theta \cos(n\theta) \qquad \ldots\ldots\ldots\ldots\ldots\ldots\ldots(2.11)$$

Using equations (2.6), (2.8) and (2.11), it is shown in Appendix 2.8.1 that for $n \neq 0$,

$$E_z = \hat{E}_z \sin(n\theta) \qquad \ldots\ldots\ldots\ldots\ldots\ldots\ldots(2.12)$$

$$\text{and} \quad \hat{E}_z = \frac{jn}{kr} \hat{E}_\theta \qquad \ldots\ldots\ldots\ldots\ldots\ldots\ldots(2.13)$$

Appendix 2.8.1 further shows that:

$$E_z = \left[A\, I_n(\alpha r) + D\, K_n(\alpha r)\right] \sin(n\theta) \qquad \ldots\ldots\ldots\ldots(2.14)$$

$$\text{where } \alpha^2 = k^2 + j\omega\mu\sigma \qquad \ldots\ldots\ldots\ldots\ldots\ldots\ldots(2.15)$$

I_n and K_n are modified Bessel functions of order n, and of general complex argument [2.3]. A and D are arbitrary constants to be determined from the boundary conditions.

Using equations (2.13), (2.14) and (2.11), for $n \neq 0$

$$E_\theta = \frac{-jrk}{n} (A\, I_n(\alpha r) + D\, K_n(\alpha r)) \cos(n\theta) \qquad \ldots\ldots\ldots(2.16)$$

Using equations (2.4), (2.11), (2.12) and (2.13), Appendix 2.8.2 shows that

$$H_r = \frac{-(n^2 + k^2 r^2)}{\omega\mu r^2 k} E_\theta \qquad \ldots\ldots\ldots\ldots\ldots\ldots\ldots(2.17)$$

The appendix further shows at equations (2.59),(2.58) and (2.64) that

$$\hat{H}_\theta = \frac{-jn}{rk}\hat{H}_z \qquad \text{.........................(2.18)}$$

$$H_\theta = \hat{H}_\theta \sin(n\theta) \qquad \text{.........................(2.19)}$$

and
$$H_z = \frac{kr}{n\omega\mu}\left[\left(\frac{2rk^2}{n^2 + r^2k^2} - \frac{n}{r}\right)(A\ I_n(\alpha r) + D\ K_n(\alpha r)) + \alpha(A\ I_{n-1}(\alpha r) - D\ K_{n-1}(\alpha r))\right]\cos(n\theta) \qquad \text{.....(2.20)}$$

2.4.4 Field calculations at the region boundaries

Fig. 2.15a shows a general region m, where $E_{\theta,m}$ and $H_{z,m}$ are the field components at the upper boundary of the region, and $E_{\theta,m-1}$ and $H_{z,m-1}$ are the equivalent values at the lower boundary.

From equations (2.16) and (2.20),

$$E_{\theta,m} = \frac{-jr_mk}{n}\left[A\ I_n(\alpha_m r_m) + D\ K_n(\alpha_m r_m)\right]\cos(n\theta) \qquad \text{......(2.21)}$$

$$H_{z,m} = \frac{k\ r_m}{n\omega\mu_m}\left[\left(\frac{2r_mk^2}{n^2 + r_m^2k^2} - \frac{n}{r_m}\right)(A\ I_n(\alpha_m r_m) + D\ K_n(\alpha_m r_m)) + \alpha_m(A\ I_{n-1}(\alpha_m r_m) - D\ K_{n-1}(\alpha_m r_m))\right]\cos(n\theta)$$

$$\text{....................(2.22)}$$

Equivalent expressions for $E_{\theta,m-1}$ and $H_{z,m-1}$ can be formed by replacing r_m in the above equations by $r_{(m-1)}$.

Now for the regions when $m \neq 1$ or N, we can put,

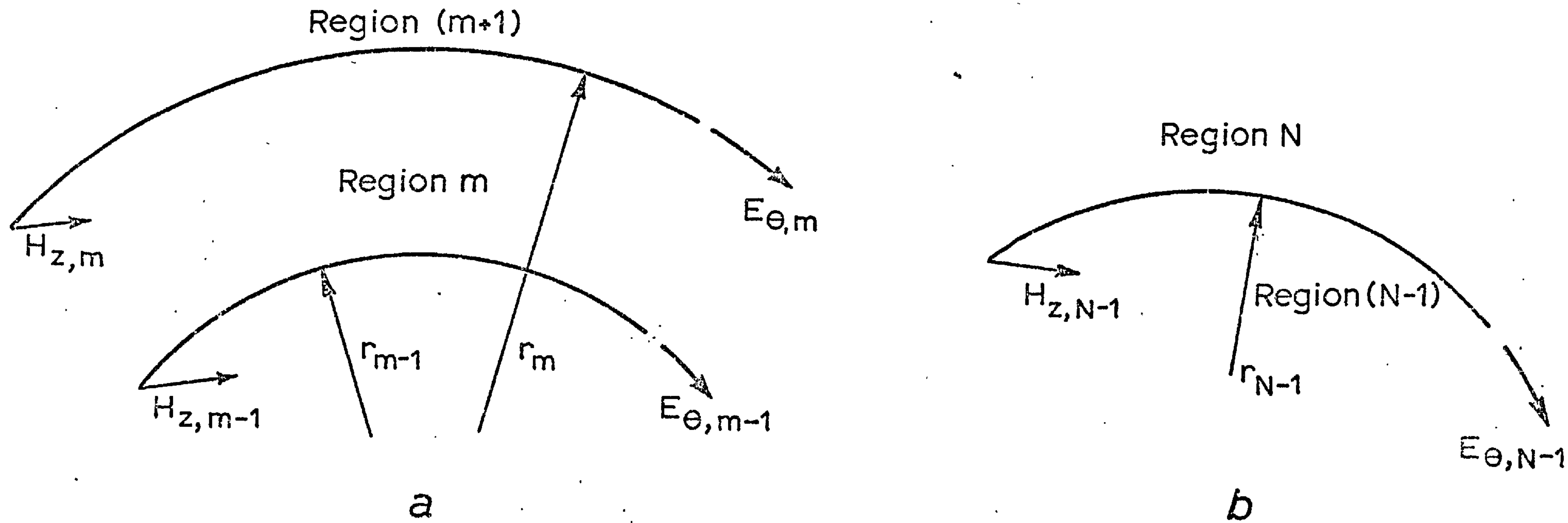

Fig. 2.15 Illustrating the mathematical model

$$\begin{bmatrix} E_{\theta,m} \\ \\ H_{z,m} \end{bmatrix} = \begin{bmatrix} \\ T_m \\ \\ \end{bmatrix} \begin{bmatrix} E_{\theta,m-1} \\ \\ H_{z,m-1} \end{bmatrix} \qquad \ldots\ldots\ldots\ldots\ldots\ldots\ldots(2.23)$$

where $\begin{bmatrix} T_m \end{bmatrix}$ is the transfer matrix (2.4)(2.5) for region m, and is given by,

$$\begin{bmatrix} \\ T_m \\ \\ \end{bmatrix} = \begin{bmatrix} a_m & b_m \\ \\ c_m & d_m \end{bmatrix} \qquad \ldots\ldots\ldots\ldots\ldots\ldots\ldots(2.24)$$

Expressions for a_m, b_m, c_m and d_m are derived in Appendix 2.8.3.

Hence given the values of E_θ and H_z at the lower boundary of a region, the values of E_θ and H_z at the upper boundary can be found using this transfer matrix. At the boundaries where no excitation current sheet exists, we have continuity of H_z and E_θ, thus for example if two regions are considered with no current sheet at the common boundary, knowing H_z and E_θ at the beginning of the first region, H_z and E_θ at the end of the second region may be calculated by successive use of the two transfer matrices. Considering the current sheet to be at radius r_g, then:

$$H'_{z,m} = H_{z,m} \qquad \text{when } m \neq g \qquad \ldots\ldots\ldots\ldots(2.25)$$

$$\text{and} \quad H'_{z,m} = H_{z,m} - J_\theta \qquad \text{when } m = g \qquad \ldots\ldots\ldots\ldots(2.26)$$

where $H_{z,m}$ is the axial magnetic field strength immediately below a boundary, and $H'_{z,m}$ is the axial magnetic field strength immediately above a boundary.

Bearing in mind the boundary conditions, it is apparent then that for the model considered, we can write,

$$\begin{bmatrix} E_{\theta,N-1} \\ H_{z,N-1} \end{bmatrix} = \begin{bmatrix} T_{N-1} \end{bmatrix} \begin{bmatrix} T_{N-2} \end{bmatrix} \cdots \begin{bmatrix} T_{g+1} \end{bmatrix} \begin{bmatrix} E_{\theta,g} \\ H_{z,g} - J_\theta \end{bmatrix} \quad \ldots\ldots(2.27)$$

and
$$\begin{bmatrix} E_{\theta,g} \\ H_{z,g} \end{bmatrix} = \begin{bmatrix} T_g \end{bmatrix} \begin{bmatrix} T_{g-1} \end{bmatrix} \cdots \begin{bmatrix} T_2 \end{bmatrix} \begin{bmatrix} E_{\theta,1} \\ H_{z,1} \end{bmatrix} \quad \ldots\ldots\ldots\ldots(2.28)$$

If region N is now considered (Fig. 2.15b) then, as $r \longrightarrow \infty$

$$I_n(\alpha r) \longrightarrow \infty$$

Therefore, from equations (2.21) and (2.22),

$$A = 0$$

$$E_{\theta,N-1} = \frac{-j\, r_{N-1} k}{n}\; D\, K_n(\alpha_N\, r_{N-1}) \cos(n\theta) \quad \ldots\ldots\ldots\ldots(2.29)$$

and

$$H_{z,N-1} = \frac{k\, r_{N-1}}{n\omega\mu_N} \left[\left(\frac{2r_{N-1}k^2}{n^2 + r_{N-1}^2\, k^2} - \frac{n}{r_{N-1}} \right) D\, K_n(\alpha_N r_{N-1}) - \alpha_N\, D\, K_{n-1}(\alpha_N r_{N-1}) \right] \cos(n\theta) \quad \ldots\ldots(2.30)$$

Considering region (1) we have,

as $r \longrightarrow 0$

$$K_n(\alpha r) \longrightarrow \infty$$

Therefore from equations (2.21) and (2.22),

$$D = 0$$

$$E_{\theta,1} = \frac{-j\, r_1\, k}{n} A\, I_n\, (\alpha_1 r_1)\, \cos(n\theta) \qquad \text{..................(2.31)}$$

and

$$H_{z,1} = \frac{k\, r_1}{n\omega\mu_1} \left[\left(\frac{2r_1\, k^2}{n^2 + r_1^2\, k^2} - \frac{n}{r_1} \right) A\, I_n\, (\alpha_1 r_1) + \alpha_1 A\, I_{n-1}(\alpha_1 r_1) \right] \cos(n\theta) \qquad \text{..................(2.32)}$$

It will be appreciated that these equations for the field components at the "end" region boundaries of the model still contain arbitrary constants A and D. However, to solve the problem it is only the ratio of E to H, which has been defined elsewhere as the surface impedance (2.6, 2.7, 2.8, 2.9, 2.10, 2.11, 2.12), that is required for the regions 1 and N. Using these ratios and equations (2.27) and (2.28), all the field components and hence the power and the force may be determined (2.6, 2.11, 2.12). Alternatively the surface impedance concept may be used at all the region boundaries as shown in the following sections.

2.4.5 Surface impedance calculations

The surface impedance looking outwards at a boundary radius r_s is defined as,

$$Z_{s+1} = \frac{E_{\theta,s}}{H'_{z,s}} \qquad \text{..............................(2.33)}$$

and the surface impedance looking inwards is,

$$Z_s = - \frac{E_{\theta,s}}{H_{z,s}} \qquad \text{..............................(2.34)}$$

Thus from equations (2.33) and (2.25),

$$Z_N = \frac{E_{\theta,N-1}}{H_{z,N-1}} \qquad \text{.........................(2.35)}$$

Substituting for $E_{\theta,N-1}$ and $H_{z,N-1}$ from equations (2.29) and (2.30) respectively,

$$Z_N = -j\omega\mu_N \frac{K_n(\alpha_N r_{N-1})}{\left[\left(\frac{2r_{N-1}k^2}{n^2 + r_{N-1}^2 k^2} - \frac{n}{r_{N-1}}\right)K_n(\alpha_N r_{N-1}) - \alpha_N K_{n-1}(\alpha_N r_{N-1})\right]}$$

$$\text{.........................(2.36)}$$

This gives the surface impedance of the Nth region uniquely since it contains no arbitrary constants.

The surface impedance of the other regions going towards the current sheet may now be calculated successively using the following expressions.

From equation (2.73), Appendix 2.8.4,

$$Z_{N-1} = \frac{b_{N-1} - Z_N d_{N-1}}{c_{N-1}Z_N - a_{N-1}} \qquad \text{.....................(2.37)}$$

Similarly $$Z_{N-2} = \frac{b_{N-2} - Z_{N-1}d_{N-2}}{c_{N-2}Z_{N-1} - a_{N-2}}$$

$$\vdots$$

$$Z_{g+1} = \frac{b_{g+1} - Z_{g+2}d_{g+1}}{c_{g+1}Z_{g+2} - a_{g+1}} \qquad \text{.....................(2.38)}$$

The surface impedance looking inwards from the current sheet can be calculated as follows:

From equation (2.34)

$$Z_1 = \frac{-E_{\theta,1}}{H_{z,1}} \quad \text{..............................(2.39)}$$

Substituting for $E_{\theta,1}$ and $H_{z,1}$ from equations (2.31) and (2.32) respectively,

$$Z_1 = j\omega\mu_1 \frac{I_n(\alpha_1 r_1)}{\left[\left(\frac{2r_1 k^2}{n^2 + r_1^2 k^2} - \frac{n}{r_1}\right) I_n(\alpha_1 r_1) + \alpha_1 I_{n-1}(\alpha_1 r_1)\right]} \quad \text{...(2.40)}$$

Again this now contains no arbitrary constants and a similar chain of calculations can be performed to find Z_g.

From equation (2.74), Appendix 2.8.4,

$$Z_2 = \frac{b_2 - a_2 Z_1}{c_2 Z_1 - d_2} \quad \text{..............................(2.41)}$$

and hence

$$Z_g = \frac{b_g - a_g Z_{g-1}}{c_g Z_{g-1} - d_g} \quad \text{..............................(2.42)}$$

The input surface impedance at the current sheet, Z_{in} is given by the effective impedance of a parallel combination of Z_g and Z_{g+1}, hence

$$Z_{in} = \frac{Z_g Z_{g+1}}{Z_g + Z_{g+1}} \quad \text{..............................(2.43)}$$

Substituting for Z_g and Z_{g+1} using equations (2.34) and (2.33) respectively, and rearranging,

$$Z_{in} = \frac{-E_{\theta,g}}{H_{z,g} - H'_{z,g}} \quad \ldots\ldots\ldots\ldots\ldots\ldots\ldots\ldots\ldots (2.44)$$

From equation (2.26),

$$H'_{z,g} = H_{z,g} - J_\theta$$

Substitute this in equation (2.44),

$$Z_{in} = \frac{-E_{\theta,g}}{J_\theta}$$

Thus, the input impedance at the current sheet has been determined. This means that using the relationship,

$$E_{\theta,g} = -J_\theta \, Z_{in} \quad \ldots\ldots\ldots\ldots\ldots\ldots\ldots\ldots\ldots (2.45)$$

all the field components can be found by making use of equations (2.45), (2.42), (2.34), (2.27) and (2.28).

2.4.6 Power calculations

The time average power, flowing through a boundary is given by the equation,

$$P = \mathcal{R}\left[\frac{1}{2\pi} \int_0^{\pi} (\hat{E}_\theta \hat{H}_z^* \cos^2(n\theta) - \hat{E}_z \hat{H}_\theta^* \sin^2(n\theta))\,d\theta\right] \mathrm{w/m^2} \quad \ldots\ldots (2.46)$$

Substituting for $\hat{E}_z$ and $\hat{H}_\theta^*$ from equations (2.13) and (2.18) respectively, and integrating,

$$P = 0.25\left(1 + \frac{n^2}{k^2 r^2}\right) \mathcal{R}(\hat{E}_\theta \hat{H}_z^*) \quad \mathrm{w/m^2} \quad \ldots\ldots\ldots\ldots\ldots\ldots (2.47)$$

Now, at the current sheet, the powers flowing outward and inward are given by the equations,

$$P_{in,out} = 0.25\left(1 + \frac{n^2}{k^2\, r_g^2}\right) \mathcal{R}(\hat{E}_{\theta,g}\; \hat{H}'^{*}_{z,g}) \quad w/m^2$$

$$P_{in,in} = -0.25\left(1 + \frac{n^2}{k^2\, r_g^2}\right) \mathcal{R}(\hat{E}_{\theta,g}\; \hat{H}^{*}_{z,g}) \quad w/m^2$$

Thus, the total power flowing from the current sheet $P_{in,T}$ is given by the equation,

$$P_{in,T} = P_{in,out} + P_{in,in}$$

$$= 0.25\left(1 + \frac{n^2}{k^2\, r_g^2}\right) \mathcal{R}(\hat{E}_{\theta,g}\; (\hat{H}'^{*}_{z,g} - \hat{H}^{*}_{z,g})) \quad w/m^2$$

This expression may be re-expressed in terms of the input surface impedance, whence substituting for $\hat{H}'^{*}_{z,g}$ and $\hat{E}_{\theta,g}$ from equations (2.26) and (2.45) respectively, and rearranging,

$$P_{in,T} = 0.25\left(1 + \frac{n^2}{k^2\, r_g^2}\right)/J'/^2\, \mathcal{R}\,(Z_{in}) \qquad w/m^2$$

or $$P_{in} = 0.5\pi\, r_g\left(1 + \frac{n^2}{k^2 r_g^2}\right)/J'/^2\, \mathcal{R}\,(Z_{in}) \qquad w/m \quad \ldots\ldots\ldots(2.48)$$

The axial force, F_a, is given by,

$$F_a = \frac{P_{in}}{\lambda f} \quad \text{Newton/unit axial length} \qquad \ldots\ldots\ldots\ldots\ldots\ldots(2.49)$$

2.4.7 Computation

The method outlined above can be readily programmed for digital computer use and has been used to calculate the axial force and the core flux density for the experimental model.

In this case, n is taken to be 1, which means that only the fundamental component in the θ direction is considered. However, the method is of course general; any number of harmonics in the θ direction can be considered in turn (by changing n to the appropriate harmonic number with the exception of n = 0) to calculate the harmonic power. Since linear magnetic conditions are assumed, the total power input can be taken to be the sum of the power harmonic components, and the total axial force is then given by,

$$F_a = \frac{\sum_n P_{in}}{\lambda f} \quad N/m \qquad \text{.........................(2.50)}$$

2.4.8 Calculation of the core flux density

The rotor core can be represented by say region (1) of the model. If it is assumed that this region is made of infinitely laminated iron, then the contribution of $H_{z,1}$ and $H_{\theta,1}$ to the core flux density can be neglected. This leaves the radial component $B_{r,1}$ only to be considered. This component is cosinusoidally distributed in the circumferential direction, and

It will be appreciated that since $H_{z,1}$ and $H_{\theta,1}$ are negligible the whole of the flux from one transverse pole passes across a diameter of the core section. Thus since the average flux density is given by $\frac{2}{\pi}\hat{B}_{r,1}$, then the flux per metre crossing the diameter is $\frac{2}{\pi}\hat{B}_{r,1}\pi r_1 = 2r_1\hat{B}_{r,1}$ so that the core flux density assuming that the flux is evenly distributed across the diameter is given by $\hat{B}_c = 2r_1\hat{B}_{r,1}/2r_1 = \hat{B}_{r,1}$ ....(2.51)

2.4.9 Comparison with existing theoretical approaches for a planar model

If a model is chosen so that the thickness of each layer is very small compared with the radius, then it may be analysed as a planar model.

The results for such a model were obtained with the layer thicknesses of the order 10^{-3} of the radii, first from the analysis mentioned above (sections 2.4.1 to 2.4.7) and secondly from a planar theory using the Preston and Reece [2.13] model for one harmonic and employing for this the surface impedance method suggested in reference 2.14. The results obtained by the two methods were found to be numerically within 1% for the particular case calculated.

A conventional simple analysis assuming that the flux density does not vary across the machine gap was also attempted. This again gave results consistent with the main analysis for the model considered above.

2 4.10 Theoretical analysis for the conventional tubular motor

The power input, force and flux components have been derived using the analysis given in reference 2.12.

The core flux density is then calculated as follows. The excitation in this case is constant in the circumferential direction; the flux has the same direction instantaneously at all points on a circumferential line. Thus the flux from one pole must pass axially to the adjacent poles. If the tubular motor had no ends then conventional machine conditions would apply. That is one half of the flux from a particular pole would pass axially down the core to the preceding pole while the second half would pass axially to the following pole. Nix and Laithwaite [2.1] showed that providing a model having planar geometry could be assumed, the actual core densities, when end effects are accounted for, have values which are greater than the conventional value (of the order of 1.1 - 1.3). They also showed that the force calculated would be less than the conventional force by a factor between 0.85 and 0.95. In order to produce an optimistic view of the conventional machine for comparison purposes and in the absence of a cylindrical geometry analysis that accounts for end effects, it was decided to treat the core flux and force on the conventional basis. Thus if region (1) of the model is infinitely laminated iron, then the core density may be calculated from the radial flux density component using the expression,

$$\hat{B}_c = \frac{2p_1}{\pi r_1} \hat{B}_{r,1} \qquad \text{.........................(2.52)}$$

2.5 Experimental machines

In order to compare the performance of the new machines with conventional tubular machines, and in order to verify the analysis described in the previous section, two models were made. The first of these used the coil form of construction explained in Section 2.2.1. The second was a tubular motor equivalent to the first using circular coils.

2.5.1 The model of the new machine

This model used a surface primary winding which was formed on a tube made from an insulating material and having a diameter d_a = 70 mm. The skewed coils forming the winding were made to simulate an original winding having diamond shaped coils. The coil sides were skewed at 45° with respect to the motor axis. Fig. 2.16 shows a photograph of one of the coils. Twelve of these were used to form each winding layer. The surface axial length of each coil was arranged so that three coils extended over a

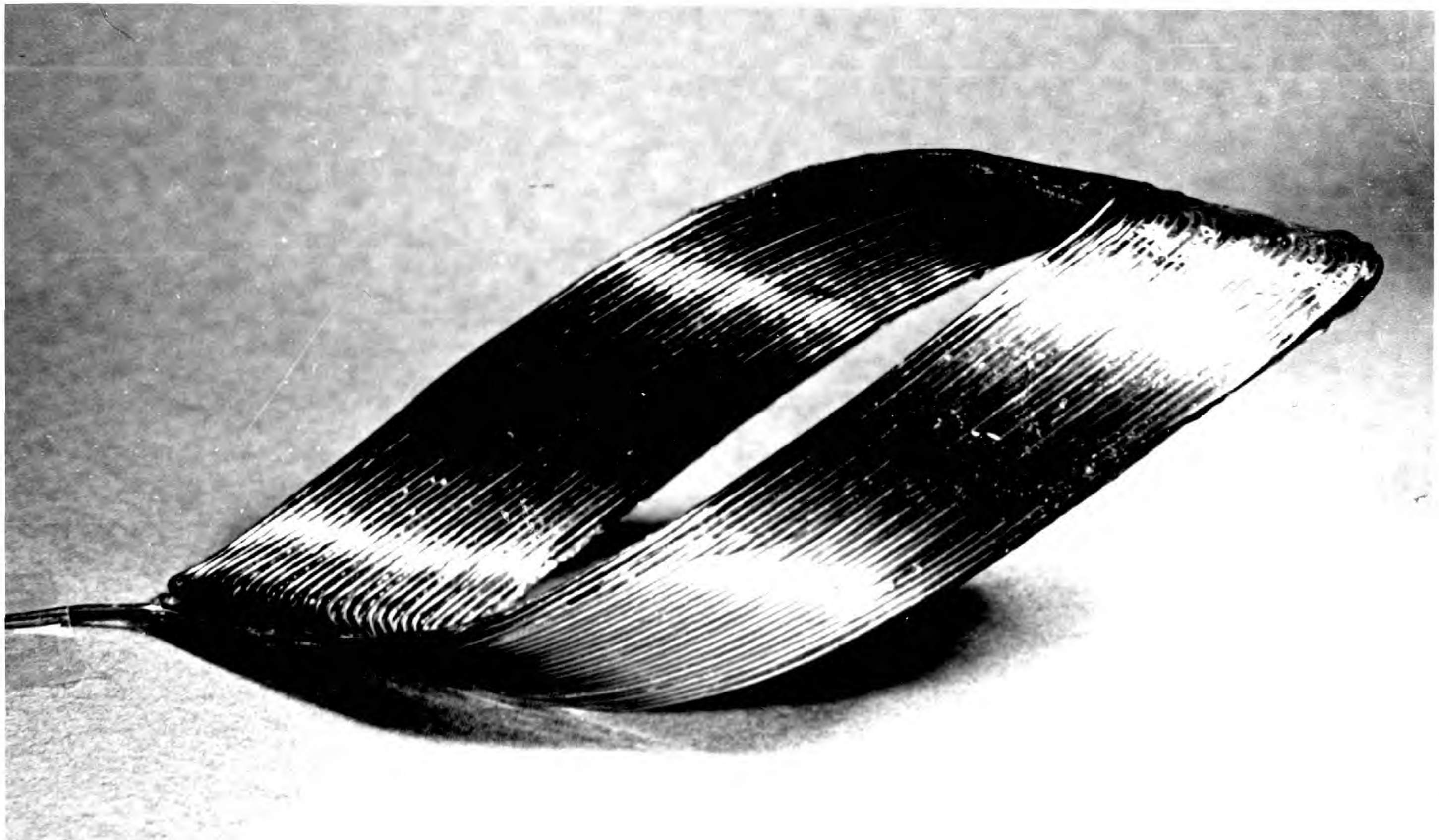

Fig. 2.16 One coil used in the transverse flux experimental motor

distance equal to $\pi d_a/2$. The winding may be connected for either two or four poles by using either two coils or one coil per pole and phase. When the machine is connected for four poles it also simulates a helical winding. Connection as a two pole machine results in a virtual chording factor of 0.707 since the winding is simulating an original structure in which the coil pitch is one half the pole pitch. No primary iron circuit was provided. The secondary member consisted of disc shaped laminations contained inside a copper tube. The outside and inside diameters of this were 63.2 and 57.3 mm. respectively.

The analysis assumes an infinitely thin current sheet excitation. This cannot of course be achieved practically. The thickness of the windings of the model is appreciable and not completely uniform. Thus the average diameter of the excitation is used in the calculations.

2.5.2 The conventional tubular motor

This machine was constructed so that it was equivalent to the new machine model. That is, the axial coil length and the number of the circular coils was identical. The rotor dimensions were the same, but in this case the rotor core was axially laminated as shown in Fig. 2.12.

2.6 Experimental results

2.6.1 Flux measurements on the new machine

In order to verify that the excitation produced by the winding was as calculated in Section 2.4.1 the windings were excited and the three flux components B_r, B_θ and B_z were measured in the absence of the secondary. These values were found to vary by only a small percentage (approximately 5%) along the majority of the tube length. The average values measured were found to be within 5% of the predicted value.

Measurements were then taken with the rotor present. It was anticipated that the axial component of core flux would be negligible. That is, the pole flux was thought to pass transversely across the core. The analysis confirmed this prediction. In order to verify the point practically a coil of the shape shown in Fig. 2.17 was inserted between the rotor disc laminations. This coil should measure any flux of the form shown in the figure. Measurements made using this coil confirmed that the axial flux was negligible along the tube length. Thus in order to find the core flux density, coils on the surface of the rotor core of the form also shown in Fig. 2.17 may be used. As may be seen from the figure, five coils covering half the stator length were provided. With the field travelling in a first direction four sets of readings were taken from the coils, the rotor being displaced by one quarter of the search coil pitch between

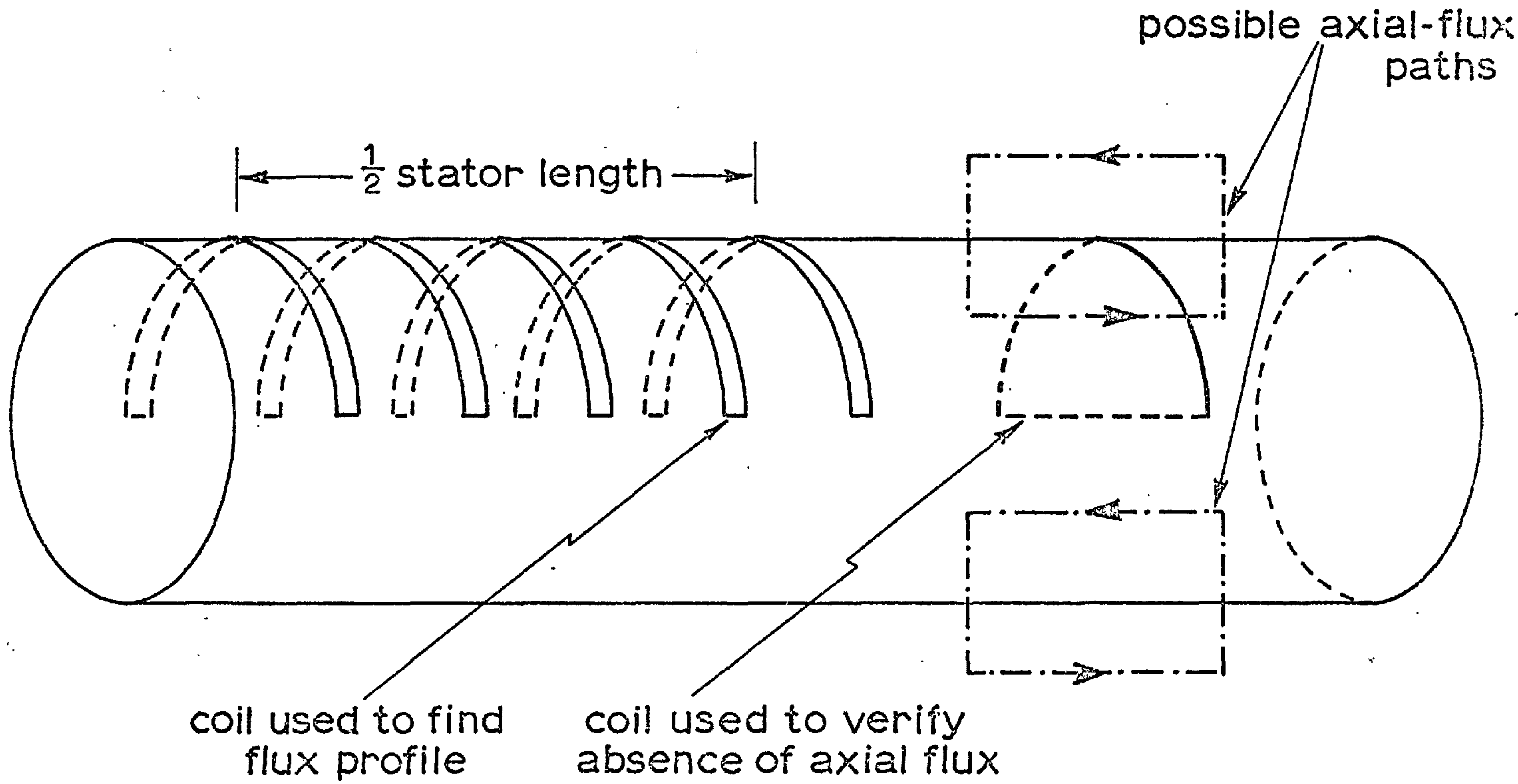

Fig. 2.17. Search coil arrangements

successive sets. This of course gives readings which may be interleaved to provide a detailed flux profile over half the machine length. The process was then repeated with the field travel reversed. Fig. 2.18 shows the results obtained from this procedure for the case of the two pole connection at a frequency of 70 Hz. It will be observed that the flux is affected by the phase bands of the excitation. The dotted line shown on the figure is a suggested average value of the core flux neglecting the values at the ends of the machine. The solid line shows the predicted result from the analysis. This process was repeated for various frequencies for both the two and the four pole connections. Figs. 2.19 and 2.20 show the measured and predicted values for the two and the four pole connections respectively. It will be observed that reasonable agreement is obtained.

2.6.2 Flux measurements on the conventional machine

Five circular coils around the rotor core were provided in the same relative positions as those for the new machine and sets of results were taken in the same manner. Fig. 2.18 shows a sample flux profile for one case. Again the dotted line represents a suggested average flux while the solid line shows the predicted value. The process was repeated for a set of frequencies for both the two and the four pole connections. Fig. 2.21 shows the calculated and measured values for the two pole connection plotted against frequency. Again the agreement is found to be reasonable.

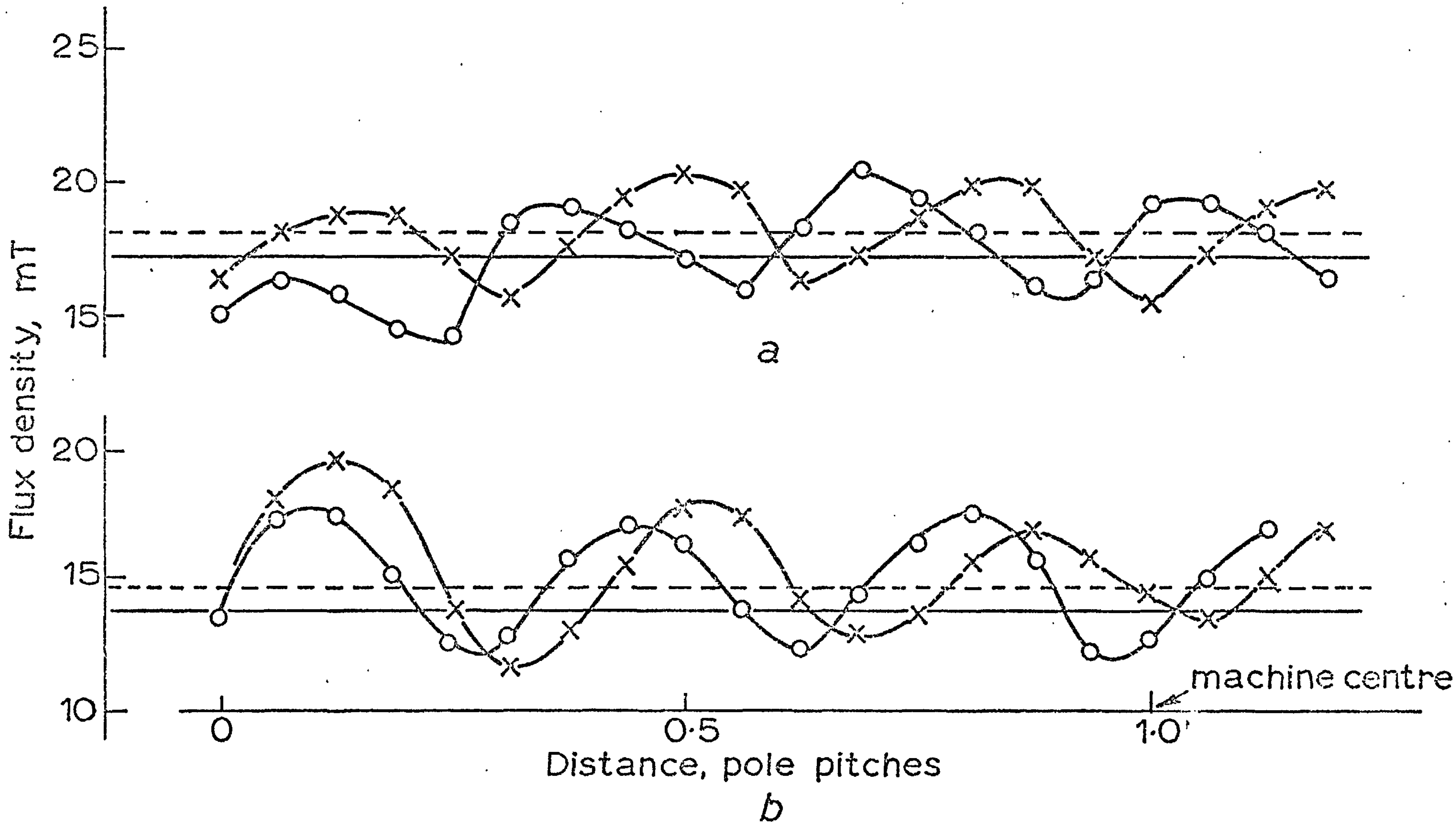

Fig. 2.18 Flux profiles at 70 Hz, two-pole connection

(a) Conventional machine
(b) Transverse flux machine

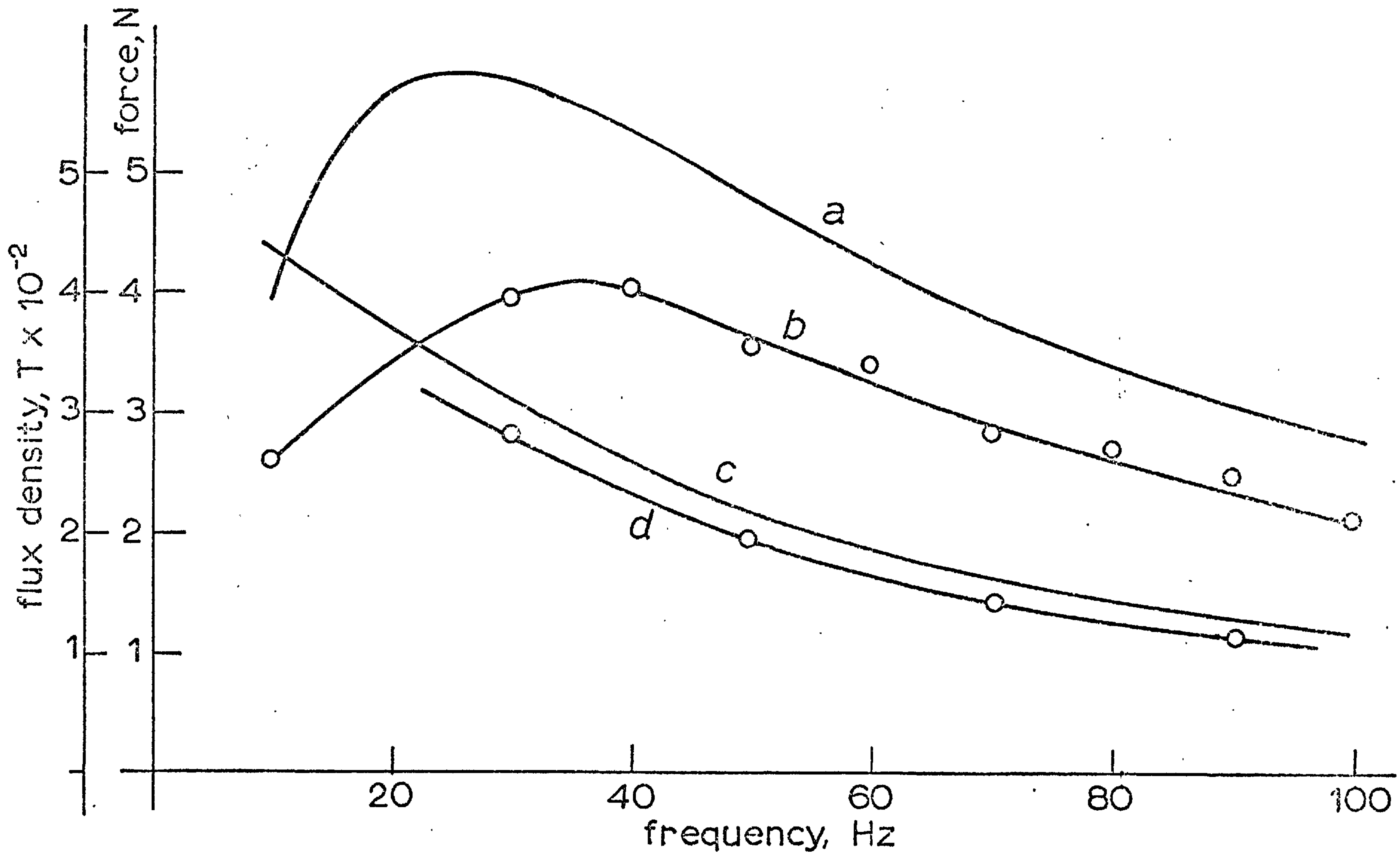

Fig. 2.19 Force and core flux density at constant current, transverse flux machine two-pole connection

(a) Theoretical force
(b) Measured force
(c) Theoretical flux density
(d) Measured flux density

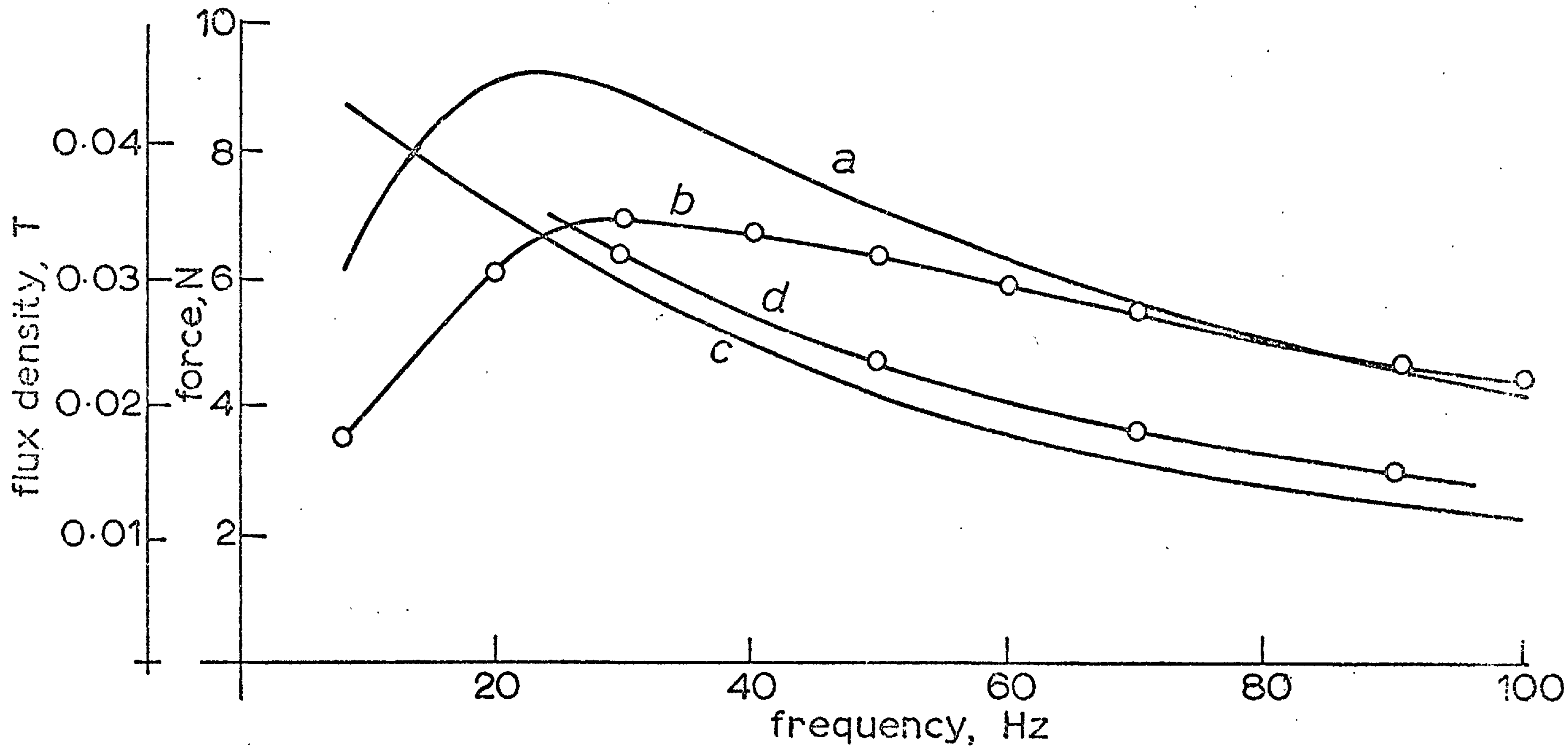

Fig. 2.20 Force and core flux density at constant current, transverse flux machine four-pole connection

(a) Theoretical force
(b) Measured force
(c) Theoretical flux density
(d) Measured flux density

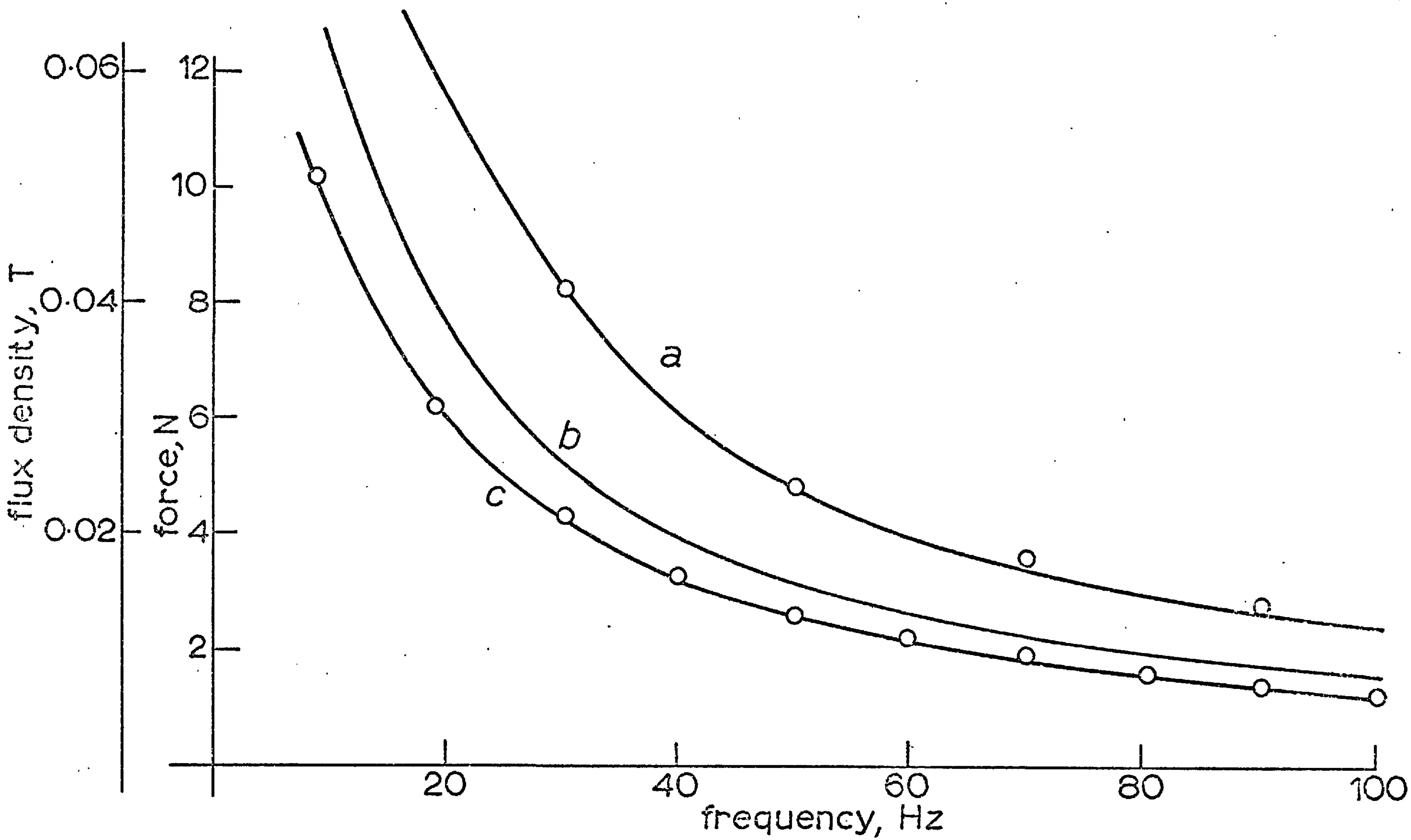

Fig. 2.21 Force and core flux density at constant current, conventional machine two-pole connection

(a) Flux density, line shows theoretical values, points show measured results
(b) Theoretical force (c) Measured force

2.6.3 Area correction factor for the new machine

It will be appreciated that the ends of the windings produce sections which are not complete. This may be appreciated with the aid of Fig. 2.22 which shows a developed view of the windings.

In order to assess the effect of the ends an experiment was performed in which the excitation length was successively shortened. The pole pitch used corresponded to the four pole condition. Fig. 2.23 shows the standstill force produced at 50 Hz plotted against the number of coils omitted from each layer at one end of the winding. The theoretical force assuming that the length of excitation was $2\pi d_a$ in the complete winding case is also plotted on the figure. It will be observed that the measured force is deficient by an amount which could be considered to be constant. This is to be expected since as the excitation length is reduced the sections of incomplete winding become relatively more important. The ratio of the measured and calculated forces for full length excitation corresponds approximately to the ratio of the area covered by the complete excitation to $2(\pi d_a)^2$. It was therefore felt that all the calculated results should be multiplied by this area ratio to allow for the ends. It must be emphasised that the confirmatory experimental results have been performed at only one frequency and the factor must be applied with some caution.

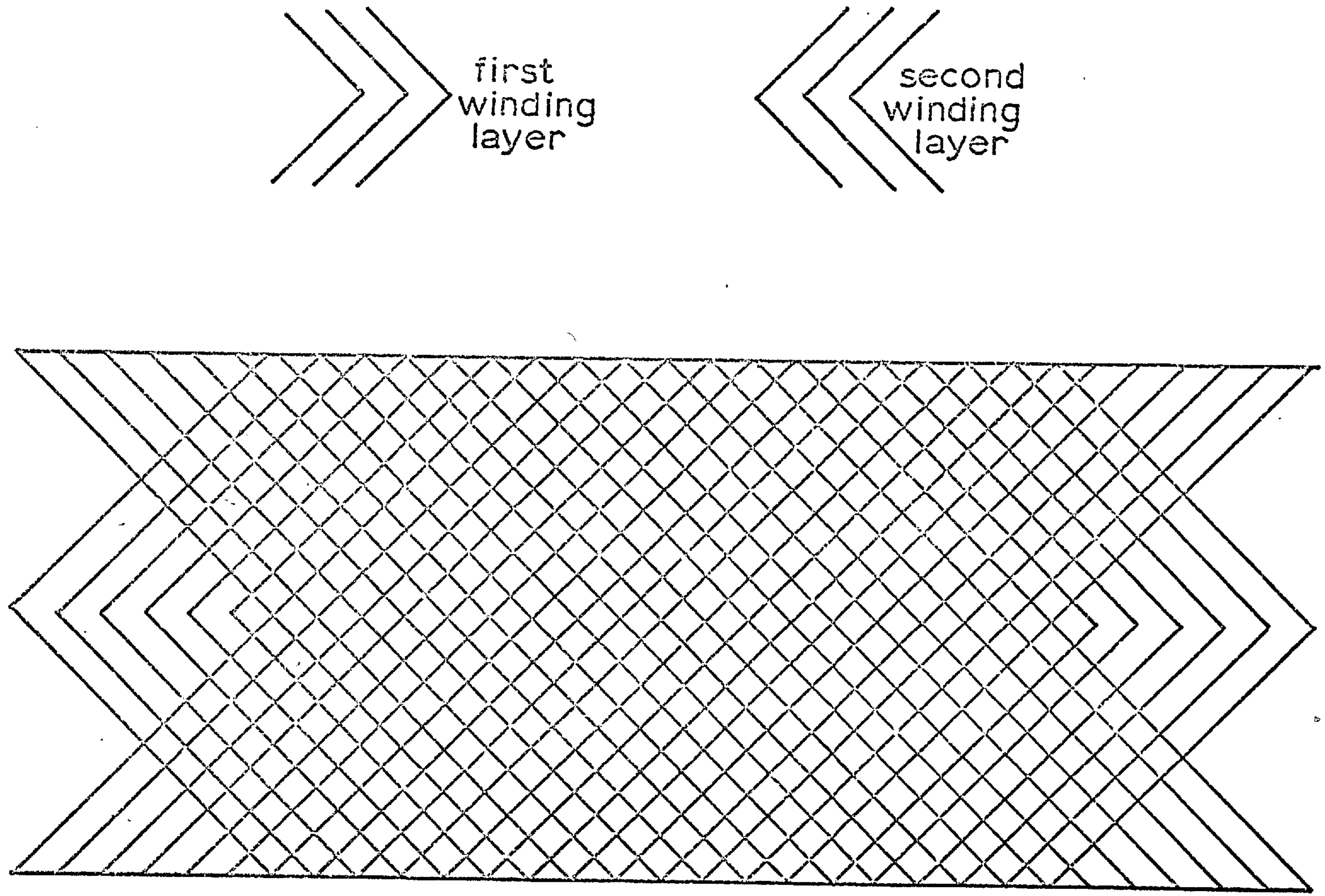

Fig. 2.22 Developed view of the winding layers in the transverse motor

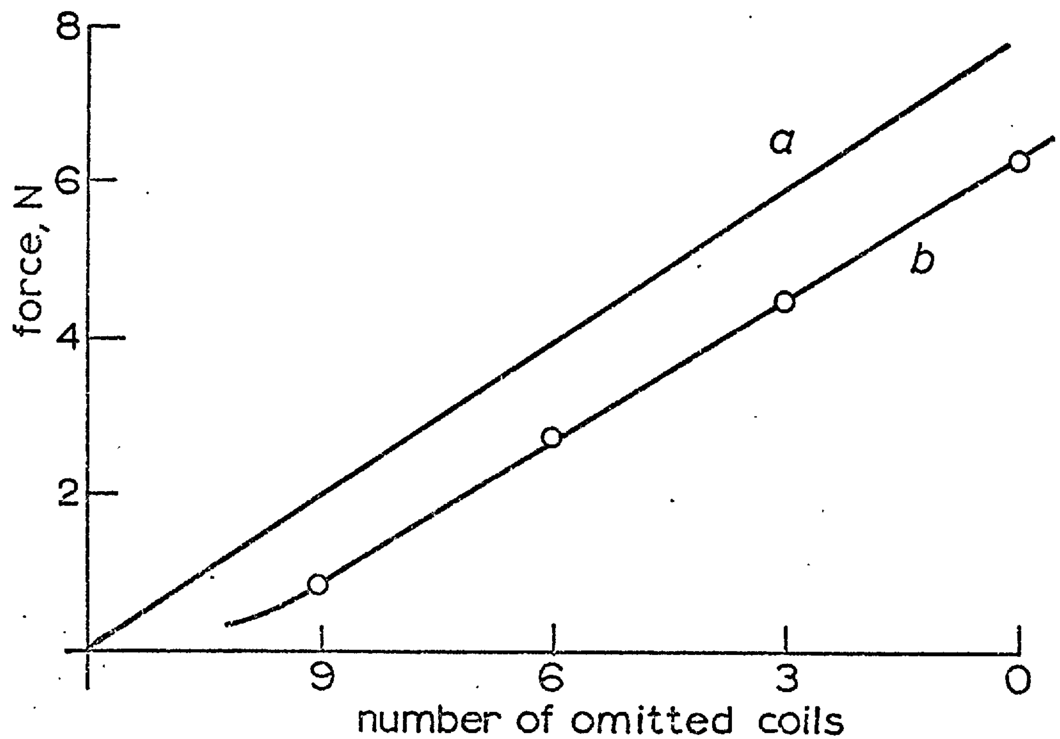

<u>Fig. 2.23</u> Forces with omitted coils, transverse flux four-pole connection, 50 Hz.

(a) Theoretical
(b) Measured

2.6.4 Force measurements on the two models

The measured and predicted standstill forces at constant excitation current for various arrangements are shown on Figs. 2.19, 2.20 and 2.21.

In order to compare the performance of the two machines at a given core flux density the forces were scaled to a constant core flux density using the previous results. The comparison between the forces in the four pole connections showed that the performance of the two machines was about the same, however in the two pole connection the transverse flux motor produced about twice the force of the conventional as shown in Fig. 2.24 which also shows the theoretical value.

2.7 Conclusions

The new machines are useful when the core flux is the limiting design factor. In the comparisons attempted in this chapter only standstill forces have been considered. It will be appreciated that this is the most pessimistic comparison so far as the new machines are concerned; the core fluxes are of course at their lowest values at standstill for a particular current loading.

The analysis was performed on the assumption of sinusoidal conditions in the axial direction, that is for an infinite

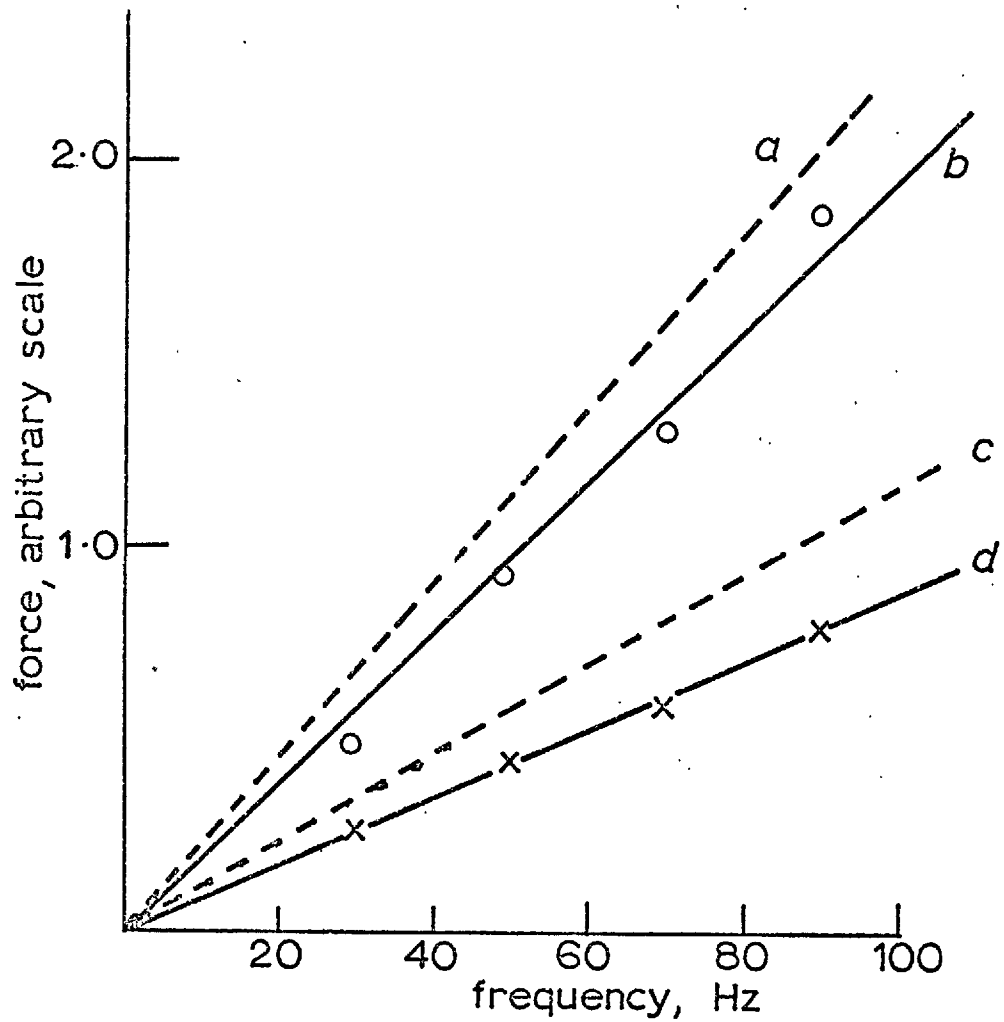

Fig. 2.24 Force at constant core flux density, two-pole connection

(a) Transverse, theoretical (b) Transverse, measured
(c) Conventional, theoretical (d) Conventional, measured

length. The predicted fluxes agreed more closely than the forces with the experimental results. This is thought to be due to the end winding effects. It is possible that if the true force per $(\text{metre})^2$ could be measured locally at the middle of the tube as could the flux, then this would show a better agreement with theory.

2.8 Appendix

2.8.1 Derivation of the electric field strength

From equation (2.6)

$$\operatorname{div} J = \frac{1}{r}\frac{\partial(rJ_r)}{\partial r} + \frac{1}{r}\frac{\partial J_\theta}{\partial \theta} + \frac{\partial J_z}{\partial z} = 0$$

$$J_r = 0 \text{ because } \sigma_r = 0$$

then, assuming $\sigma_z = \sigma_\theta = \sigma$, and $n \neq 0$, using equations (2.8) and (2.11) gives

$$\hat{E}_z = \frac{jn}{kr}\hat{E}_\theta \qquad \text{.................................(2.53)}$$

and $E_z = \hat{E}_z \sin(n\theta)$ ....(2.54)

From equations (2.4) and (2.9)

$$(\text{curl curl } E)_z = -js\omega\mu\,(\text{curl } H)_z$$

Then substituting for curl H from equation (2.3) and using equation (2.8)

$$(\text{curl curl } E)_z = -\,js\omega\mu\,\sigma\,E_z$$

Then using equations (2.7) and (2.12)

$$\frac{\partial^2 E_z}{\partial r^2} + \frac{1}{r}\frac{\partial E_z}{\partial r} - E_z\left(\frac{n^2}{r^2} + \alpha^2\right) = 0$$

where $\alpha^2 = k^2 + js\omega\mu\sigma$

Thus the general solution for E_z is

$$E_z = \left[A\ I_n(\alpha r) + D\ K_n(\alpha r)\right] \sin(n\theta) \quad \text{..............(2.55)}$$

2.8.2 Derivation of the magnetic field strength

From equation (2.4)

$$(\text{curl } E)_r = -\ j\omega\mu H_r$$

Using equations (2.11), (2.12) and (2.13)

$$H_r = \frac{-(n^2 + k^2r^2)}{\omega\mu r^2\ k}\ E_\theta \quad \text{........................(2.56)}$$

then from equation (2.3)

$$(\text{curl } H)_\theta = J_\theta$$

and using equations (2.1), (2.17) and (2.11)

$$H_z = \hat{H}_z \cos(n\theta) \quad \text{........................(2.57)}$$

From equations (2.3) and (2.10)

$$(\text{curl } H)_r = J_r = 0$$

i.e. $\dfrac{1}{r}\dfrac{\partial H_z}{\partial\theta} - \dfrac{\partial H_\theta}{\partial z} = 0$

then substituting for H_z from equation (2.57)

$$H_\theta = \hat{H}_\theta \sin(n\theta) \qquad \text{.............................(2.58)}$$

where $\hat{H}_\theta = \frac{-jn}{rk} \hat{H}_z$ ....(2.59)

From equation (2.5)

$$\text{div } B = 0$$

and assuming $\mu_z = \mu_r = \mu_\theta = \mu$

$$\text{div } H = 0$$

that is

$$\frac{\partial (r\, H_r)}{\partial r} + \frac{\partial\, H_\theta}{\partial \theta} + r\, \frac{\partial\, H_z}{\partial z} = 0 \qquad \text{................. (2.60)}$$

substituting for H_θ from (2.59) and using (2.57) and (2.58),

$$H_z = \frac{-jkr}{(n^2 + k^2r^2)} \cdot \frac{\partial (rH_r)}{\partial r} \qquad \text{..................(2.61)}$$

From equation (2.17)

$$H_r = \frac{-(n^2 + k^2r^2)}{\omega \mu r^2 k} E_\theta$$

Therefore

$$\frac{\partial (rH_r)}{\partial r} = \frac{(n^2 - k^2r^2)}{\omega \mu r^2 k} E_\theta - \frac{(n^2 + k^2r^2)}{\omega \mu rk} \frac{\partial E_\theta}{\partial r} \qquad \text{.......(2.62)}$$

Then using this expression and equation (2.16) we have

$$\frac{\partial (rH_r)}{\partial r} = \frac{-jk}{\omega \mu rk} \Big[(n^2 + k^2r^2 - \frac{2k^2r^2}{n})(A\, I_n(\alpha r) + D\, K_{n-1}(\alpha r)) - \frac{r(n^2+k^2r^2)}{n} \alpha (A\, I_{n-1}(\alpha r) - D\, K_{n-1}(\alpha r)) \Big] \cos(n\theta) \qquad \text{....(2.63)}$$

Substituting for $\dfrac{\partial(rH_r)}{\partial r}$ from equation (2.63) into equation (2.61),

$$H_z = \frac{kr}{n\omega\mu}\left[\left(\frac{2rk^2}{(n^2 + r^2k^2)} - \frac{n}{r}\right)(A\ I_n(\alpha r) + D\ K_n(\alpha r)) + \alpha(A\ I_{n-1}(\alpha r) - D\ K_{(n-1)}(\alpha r))\right]\cos(n\theta) \quad \text{........(2.64)}$$

2.8.3 Calculation of the transfer matrix elements

From equations (2.21), (2.22), (2.23) and (2.24),

$$a_m = -r_m\Big[Y_2(K_n(\alpha_m r_{m-1})I_n(\alpha_m r_m) - I_n(\alpha_m r_{m-1})K_n(\alpha_m r_m)) - \alpha_m(K_n(\alpha_m r_m)I_{n-1}(\alpha_m r_{m-1}) + I_n(\alpha_m r_m)K_{n-1}(\alpha_m r_{m-1}))\Big] \quad \text{.(2.65)}$$

$$b_m = -j\omega\mu_m r_m\Big[I_n(\alpha_m r_m)K_n(\alpha_m r_{m-1}) - K_n(\alpha_m r_m)I_n(\alpha_m r_{m-1})\Big] \quad \text{....(2.66)}$$

$$c_m = \frac{-jr_m}{\omega\mu_m}\Big[Y_1Y_2(I_n(\alpha_m r_m)K_n(\alpha_m r_{m-1}) - K_n(\alpha_m r_m)I_n(\alpha_m r_{m-1})) + Y_2\alpha_m(I_{n-1}(\alpha_m r_m)K_n(\alpha_m r_{m-1}) + K_{n-1}(\alpha_m r_m)I_n(\alpha_m r_{m-1})) - Y_1\alpha_m(K_{n-1}(\alpha_m r_{m-1})I_n(\alpha_m r_m) + K_n(\alpha_m r_m)I_{n-1}(\alpha_m r_{m-1})) + \alpha_m^2(K_{n-1}(\alpha_m r_m)I_{n-1}(\alpha_m r_{m-1}) - K_{n-1}(\alpha_m r_{m-1})I_{n-1}(\alpha_m r_m))\Big]$$

......................(2.67)

$$d_m = r_m\Big[Y_1(I_n(\alpha_m r_m)K_n(\alpha_m r_{m-1}) - K_n(\alpha_m r_m)I_n(\alpha_m r_{m-1})) + \alpha_m(I_{n-1}(\alpha_m r_m)K_n(\alpha_m r_{m-1}) + K_{n-1}(\alpha_m r_m)I_n(\alpha_m r_{m-1}))\Big]$$

......................(2.68)

where $$Y_1 = \frac{2r_mk^2}{n^2 + r_m^2k^2} - \frac{n}{r_m} \quad \text{......................(2.69)}$$

and $$Y_2 = \frac{2r_{m-1}k^2}{n^2 + r_{m-1}^2k^2} - \frac{n}{r_{m-1}} \quad \text{......................(2.70)}$$

2.8.4 Surface impedance calculations

From equation (2.35),

$$Z_N = \frac{E_{\theta,N-1}}{H_{z,N-1}}$$

Substituting for $E_{\theta,N-1}$ and $H_{z,N-1}$ from equations (2.23) and (2.24)

$$Z_N = \frac{a_{N-1}E_{\theta,N-2} + b_{N-1}H_{z,N-2}}{c_{N-1}E_{\theta,N-2} + d_{N-1}H_{z,N-2}} \quad \text{.........................(2.71)}$$

Now from equations (2.33) and (2.25),

$$Z_{N-1} = \frac{E_{\theta,N-2}}{H_{z,N-2}} \quad \text{.........................(2.72)}$$

Substituting for $E_{\theta,N-2}$ from equation (2.72) into equation (2.71),

$$Z_N = \frac{a_{N-1}Z_{N-1} + b_{N-1}}{c_{N-1}Z_{N-1} + d_{N-1}}$$

Rearranging this,

$$Z_{N-1} = \frac{b_{N-1} - d_{N-1}\,Z_N}{c_{N-1}\,Z_N - a_{N-1}} \quad \text{.........................(2.73)}$$

From equation (2.34),

$$Z_2 = \frac{-E_{\theta,2}}{H_{z,2}}$$

Substituting for $E_{\theta,2}$ and $H_{z,2}$ from equations (2.23) and (2.24)

$$Z_2 = - \frac{(a_2 \; E_{\theta,1} + b_2 \; H_{z,1})}{(c_2 \; E_{\theta,1} + d_2 \; H_{z,1})}$$

Substituting for $E_{\theta,1}$ from equation (2.39) and rearranging,

$$Z_2 = \frac{b_2 - a_2 \; Z_1}{c_2 \; Z_1 - d_2} \qquad \text{.............................(2.74)}$$

CHAPTER THREE

ONE-DIMENSIONAL ANALYSIS OF SHORT-STATOR MACHINES

3.1 Introduction

There are two types of machine in which the stator is shorter than the rotor; the first of these is the short arc-stator machine, and the second is the short primary linear motor. This second type commonly uses a plate secondary. Fig. (3.1) shows the construction of these machines. The short arc-stator type has been used as a fixed pole pitch machine in Russia [(3.1)(3.2)(3.3)(3.4)] and has also been investigated as a variable pole pitch machine at Manchester University [(3.5)(3.6)(3.7)(3.8)]. Linear machines are currently being used as actuators for low speed or standstill purposes [(3.9)(3.10)] and are also being actively considered as the means of propulsion for high speed ground transport [(3.11)(3.12)(3.13)]. They also find use as liquid metal pumps [(3.14)(3.15)].

The analysis of these machines falls into two categories according to whether the rotor current paths are defined. That is, whether the rotor is a squirrel-cage or a simple plate. In the case of the squirrel-cage arrangement, a one-dimensional analysis is sufficient because the rotor bars ensure defined current paths transversely to the direction of motion, and the use of relatively short magnetic air-gap associated with the slotted rotor means

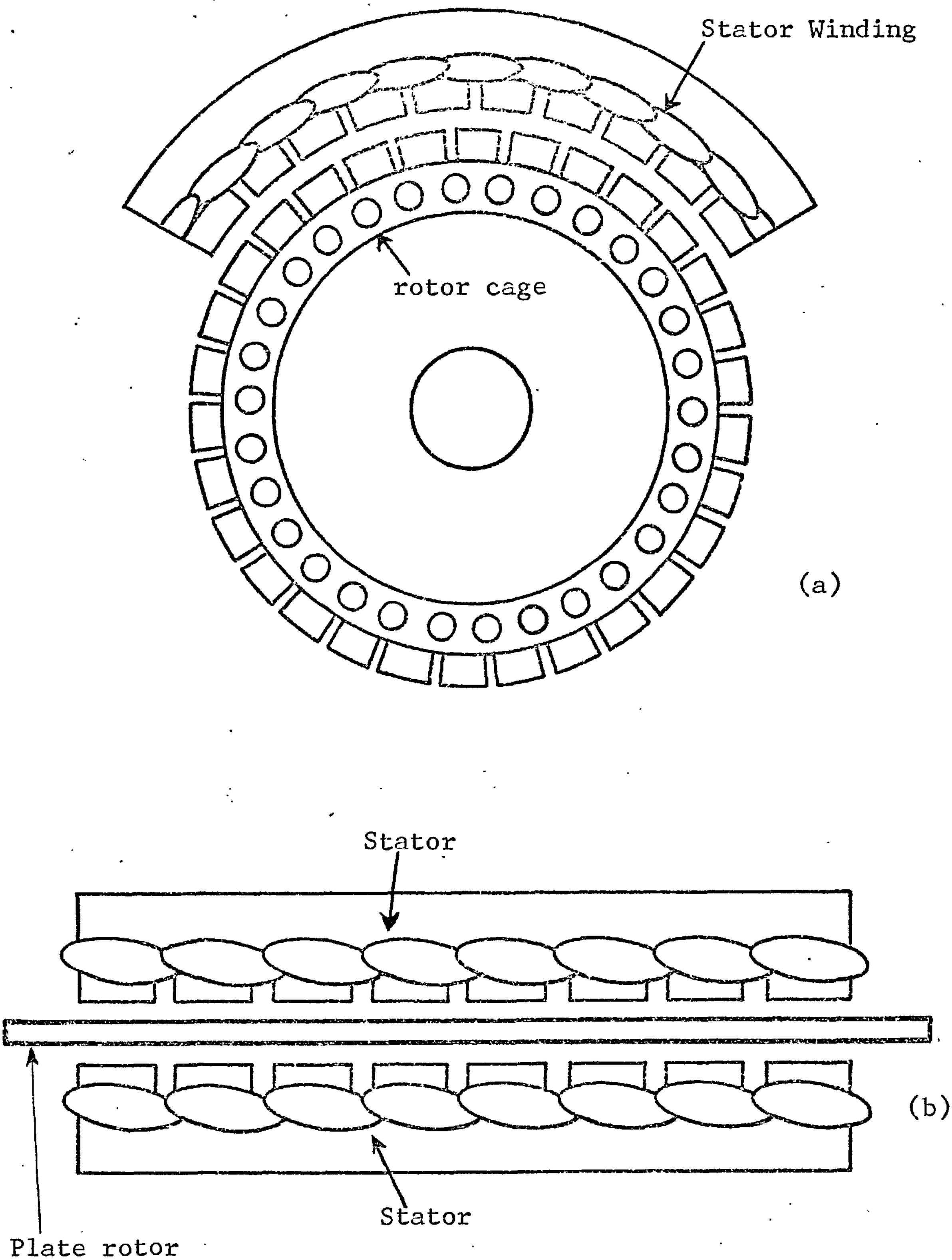

Fig. 3.1 Short stator machine

(a) Short arc stator induction motor with squirrel-cage rotor

(b) Linear motor with plate secondary

that variations of the fields in the radial direction can be neglected. These conditions do not, of course, hold for the sheet rotor linear motors since firstly the sheet imposes no restriction on the current paths so that longitudinal as well as transverse currents can flow, and secondly the magnetic air-gap is relatively large to accommodate the sheet rotor. It follows from the above considerations that a two-dimensional analysis is required in the plate rotor case.

3.2 A review of some existing analyses

A first relatively simple analysis was attempted in two early papers [3.6][3.7] concerned with machines using arc-stators. This analysis neglected the rotor leakage reactance and gave reasonable results when applied to machines with highly resistive rotors.

The analysis assumes that the flux density is zero at the entry edge of the excitation. That is, on entering the excited section a rotor loop is assumed to acquire a current equal and opposite to the instantaneoue stator current at that point. It was further assumed that this "transient" rotor current would decay as the loop proceeded under the stator, down to steady state value. The decay rate was tentatively assumed to be the rotor coupled time constant calculated for sinusoidal excitation conditions. The wave length of the rotor transient depends on the rotor speed. Thus the sinusoidal stator flux beats with the rotor flux to produce flux density patterns of the form shown in Fig. (3.2). In this figure the flux is divided into components in phase and in quadrature with the stator current, and the peak values plotted against distance. It will be appreciated that the flux distribution is very different from that of a conventional motor.

The analysis went on to use this calculated flux to work out the external characteristics of machines. Fig. (3.3) shows as an example of these calculations the force-speed characteristic for a four pole block at constant current. The family of curves corresponds to different values of t_s/T where t_s is the transit time of a point on the rotor under the excitation and T is the rotor coupled time constant. The dotted lines on the curves correspond to conventional induction motors with the same rotor coupled time constants. It can be seen that the short-stator machine gives approximately the same output as the conventional up to slips of about $1/(N_p + 1)$ where N_p is the pole

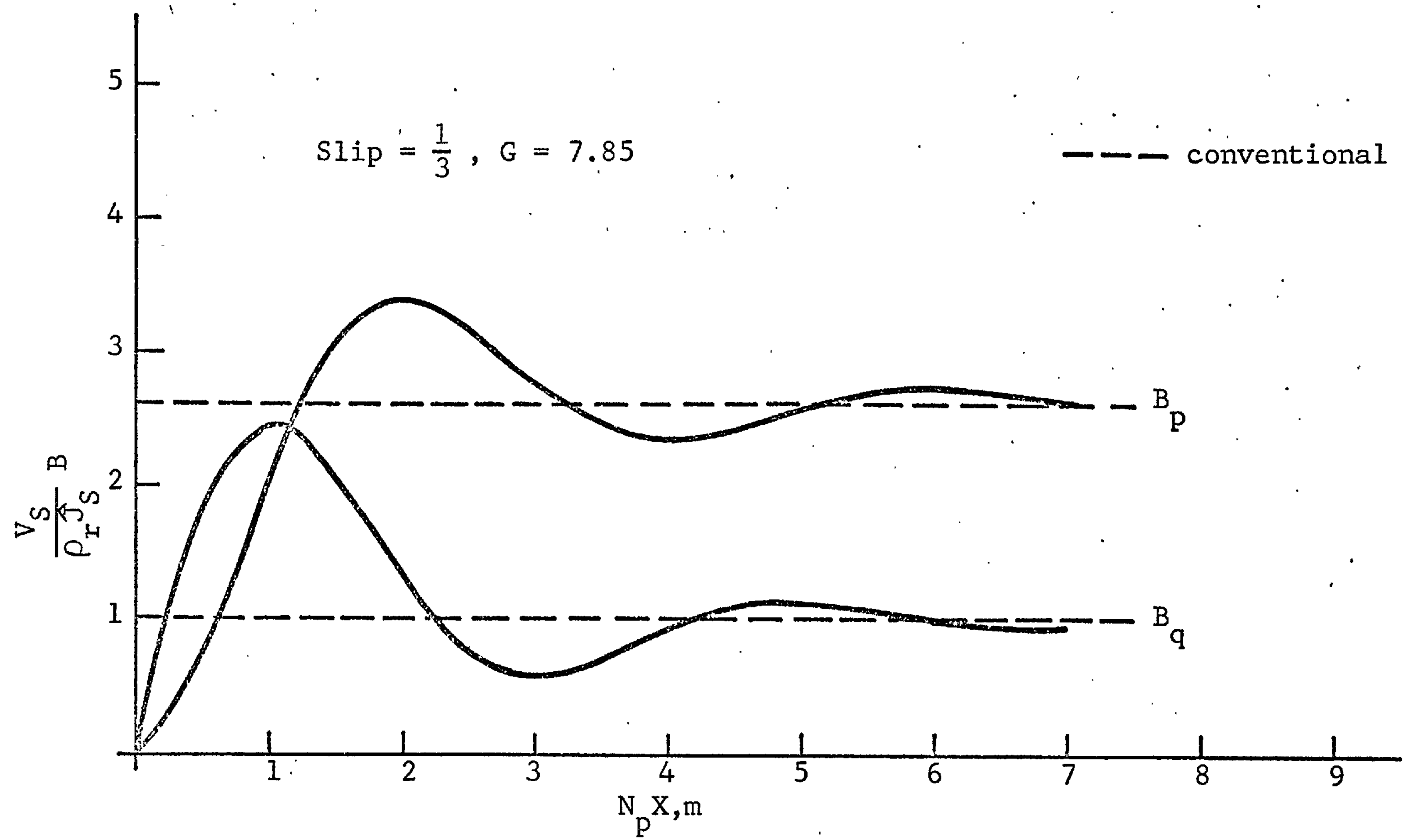

Fig. 3.2 The flux profile of a short stator machine plotted for G = 7.85 and a slip of one third.

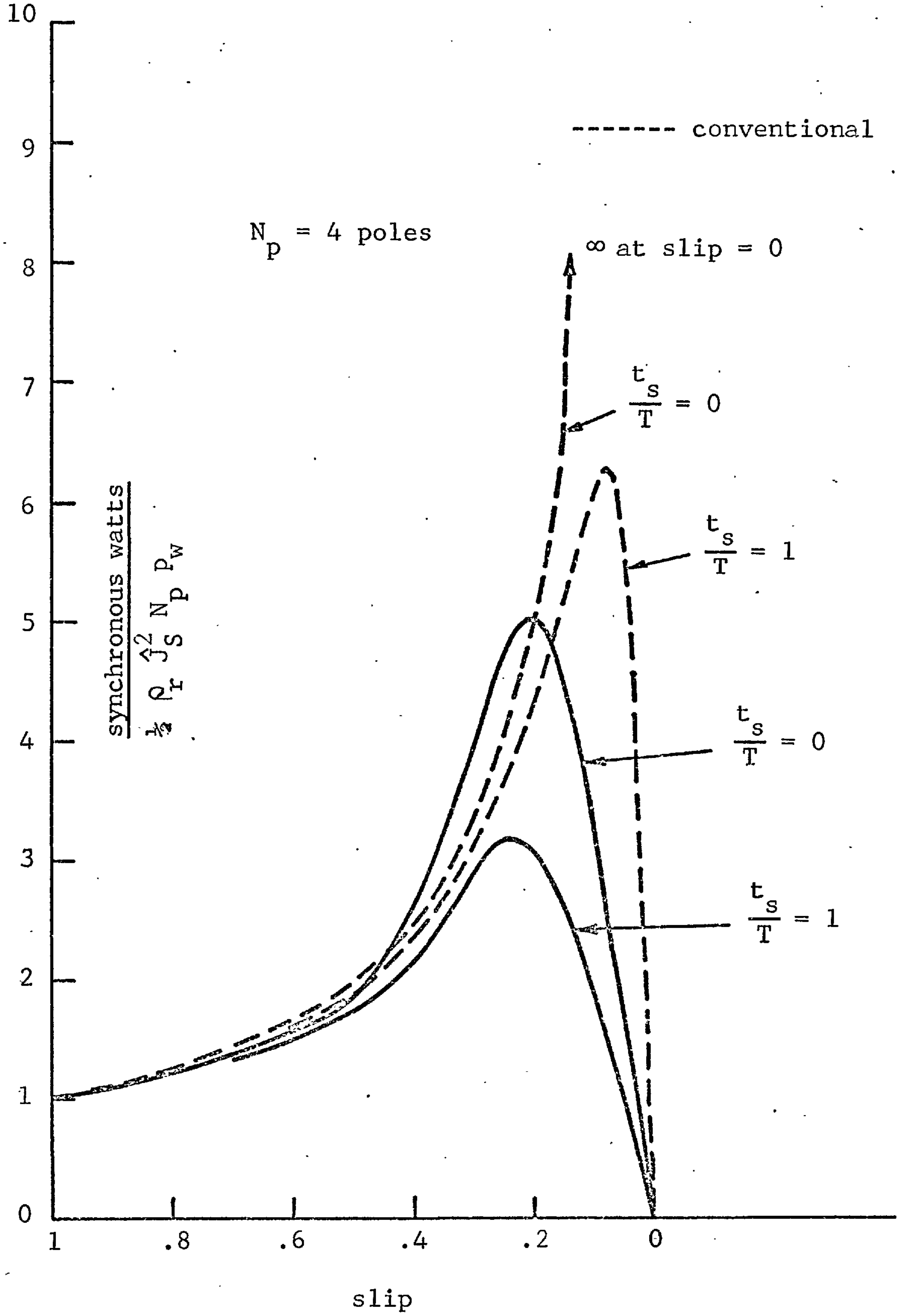

Fig. 3.3 Force-speed characteristics of a short stator machine plotted for four poles of excitation

number. Whilst the curves are drawn specifically for $N_p = 4$, the analysis shows that the $1/(N_p + 1)$ condition is in fact a rule which applies to all pole numbers, and it follows that the number of poles in a short-stator machine should be as large as possible from the point of view of getting conventional outputs. Machines of say 20 poles could run at conventional slips. It may be deduced from the output curves that non-conventional rotor losses occur in short-stator machines. These were termed "excess rotor copper losses" in the references (3.6)(3.7). Fig. (3.4) plots these excess losses and reinforces the argument about the desirability of using a large pole number; it can be seen from the figure that the excess rotor losses are minimal for slips greater than $1/(N_p + 1)$. If this were the whole picture then the penalties for short-stator working would seem to be wholly confined to the normal penalties incurred when using high slip conditions. However, the considerations so far have been limited to the input edge and the excitation region. If the core structure carries on past the excitation so that the stored energy in the rotor is dissipated at a rate which is decided by the same time constant as applied under the excitation, then no further penalty is incurred. However, in the "arc-stator" form of machine it is necessary to increase the machine gap outside

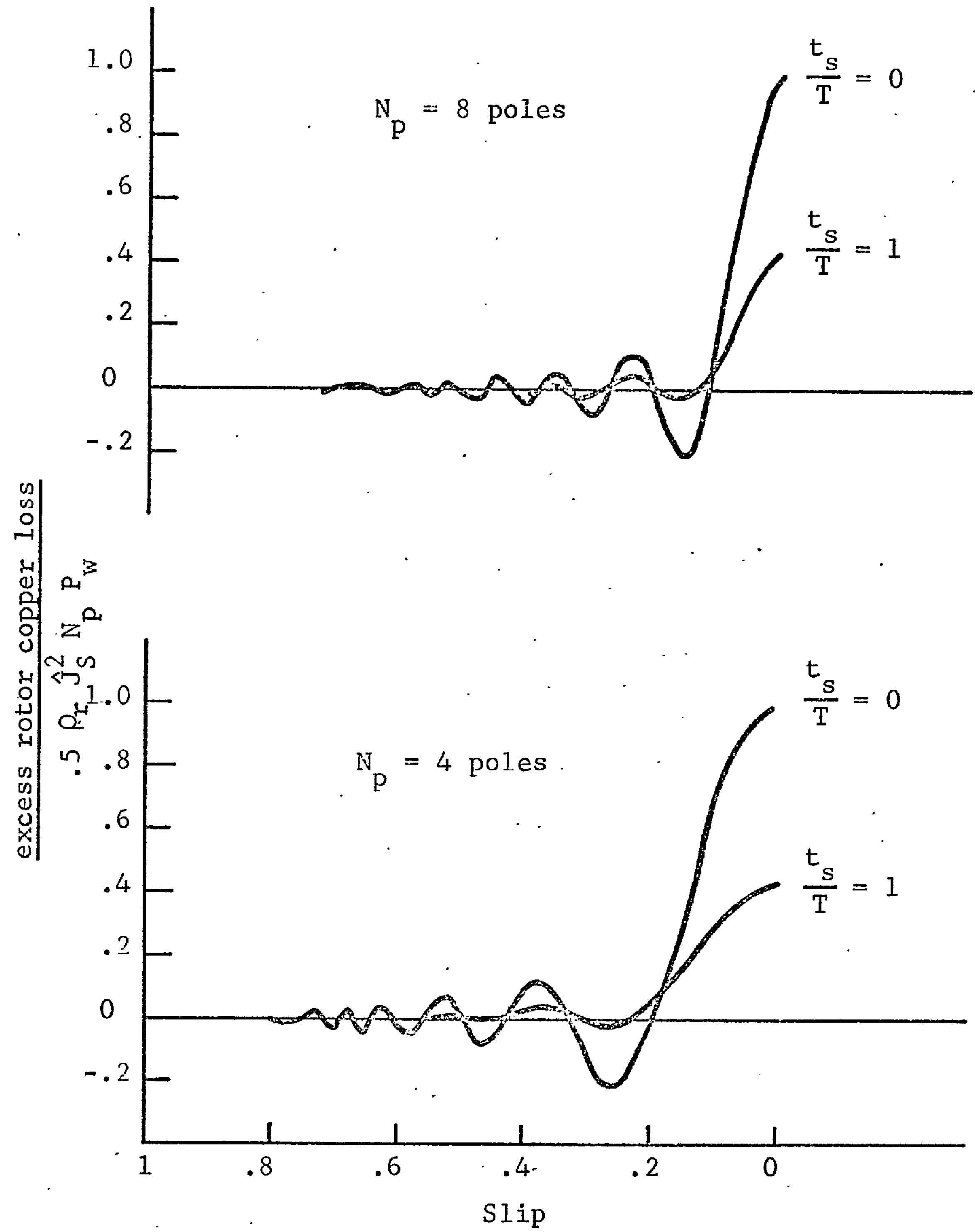

<u>Fig. 3.4</u> Excess rotor copper losses in short stator machines

the excited region or to provide a damper grid in the stator slots in order that the stored energy in the rotor shall be dissipated before the rotor re-enters the excitation [3.8]. If the gap is increased, then an "exit-edge loss" penalty is incurred. It is shown in references (3.6) and (3.7) that this loss may be calculated approximately by finding the energy transported from the excited region and by multiplying this by a factor (β - 1) where β is the air-gap ratio between the decay and the excited regions. Fig. (3.5) shows the exit-edge loss plotted against slip. It can be seen from these curves that the loss is not substantially zero until a slip of about $2/(N_p + 2)$ is reached. This again reduces the slip at which short-stator working is desirable.

The analysis in the references is performed mainly on a constant current basis. However, an attempt was made to calculate the voltage required to force this current at different slips and hence find the real and reactive intake power. The results of these calculations were disappointing. Laithwaite [3.16] showed that the resulting expressions did not power balance. The analysis was however shown to be a good guide by comparison with experimental results from machines having squirrel-cage rotors with low leakage reactance.

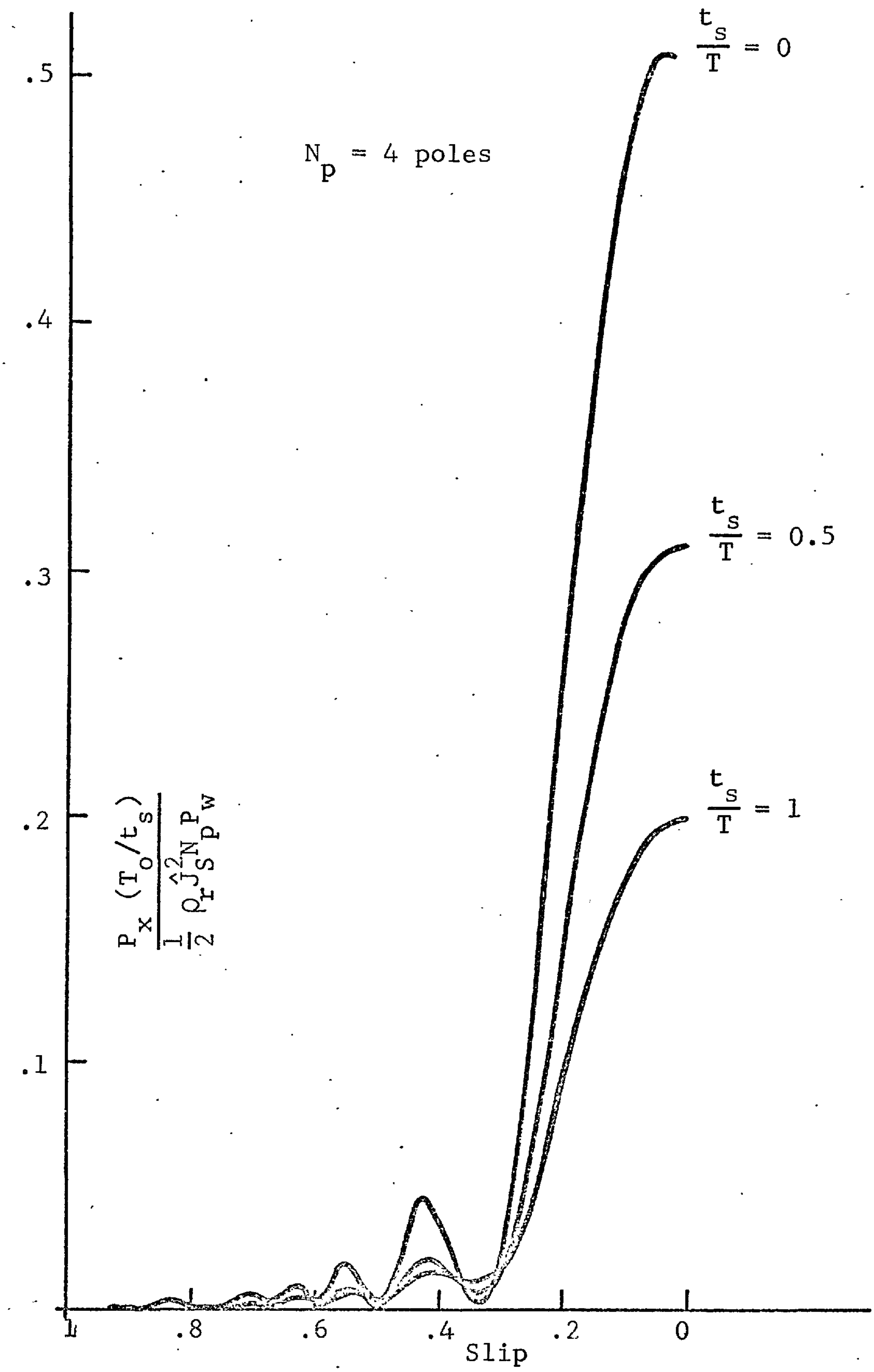

Fig. 3.5 Exit edge losses in short stator machines

This work was followed at Manchester University by a thesis by Tipping (3.17) which took rotor leakage reactance into account by using an electromagnetic model of the machine which was first suggested by Cullen and Barton (3.18). The model replaces the squirrel-cage rotor by an infinitesimally thin sheet of conducting material together with a "leakage flux" layer. The paramaters associated with these layers are arranged so that the surface resistivity ρ_r and the surface leakage inductance ℓ_r provide a rotor approximately equivalent to the squirrel-cage ignoring finite slotting effects. The model is shown in Fig. (3.6). It will be appreciated from the values of permeability shown on the figure that the flux has only radial components in the air-gap; peripheral components being excluded by making $\mu = 0$ in this direction. This assumption is, of course, valid for machines with small magnetic air-gaps. The analysis is strictly one-dimensional and therefore applies strictly only to squirrel-cage rotors. It was assumed initially that the excitation occurred over a short region of a complete stator core. The basis of the analysis abstracted from reference (3.17) is given below:-

Referring to Fig. (3.6) and applying Ampere's Law to loop 1 yields,

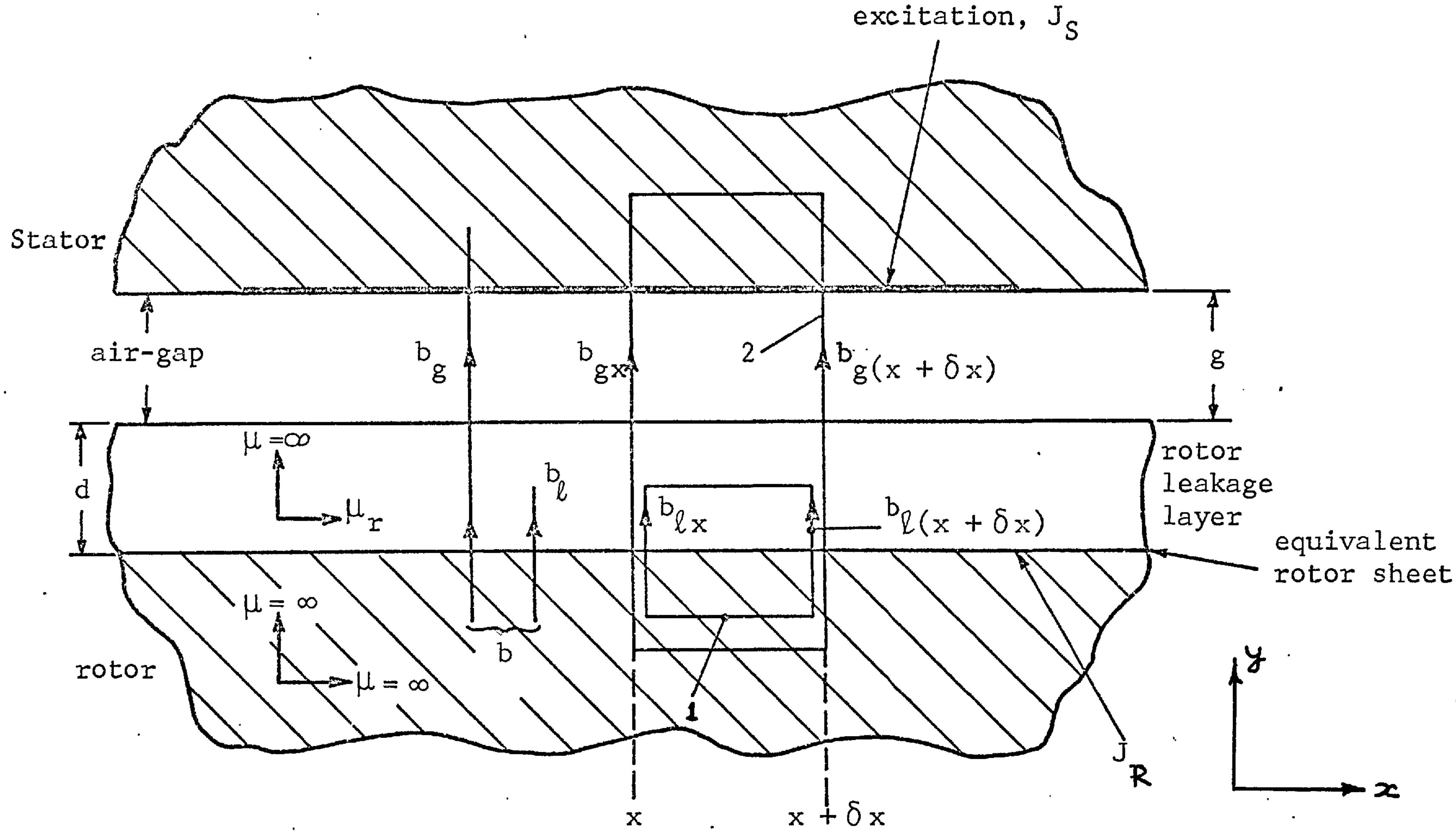

Fig. 3.6 The Cullen and Barton electro-magnetic model

$$- b_x = \mu_R J_R$$

Then since b_x is constant over the leakage layer depth ($\mu_y = \infty$)

$$b_\ell = d \frac{\partial bx}{\partial x}$$

$$\text{or} \quad b_\ell = - \mu_R \, d \frac{\partial J_R}{\partial x}$$

This is the leakage equation for the rotor and may be written as,

$$b_\ell = - \ell_r \frac{\partial J_R}{\partial x} \qquad \text{....................(3.1)}$$

where $\ell_R = \mu_R d$, is the surface leakage inductance of the equivalent sheet rotor.

From the figure it can be seen that,

$$b = b_g + b_\ell \qquad \text{....................(3.2)}$$

Again applying Ampere's law to loop 2 on Fig. (3.6) yields,

$$\frac{g}{\mu_o} \frac{\partial bg}{\partial x} = J_R + J_S \qquad \ldots\ldots\ldots\ldots\ldots\ldots\ldots(3.3)$$

Finally, Faraday's Law applied to an elementary loop taken in the plane of the rotor sheet gives the e.m.f. equation,

$$\rho_r \frac{\partial J_R}{\partial x} = V \frac{\partial b}{\partial x} + \frac{\partial b}{\partial t} \qquad \ldots\ldots\ldots\ldots\ldots\ldots\ldots(3.4)$$

The excitation is taken to be,

$$J_S = \hat{J}_S \exp(j(\omega t - \frac{\pi x}{P_w})) \qquad \ldots\ldots\ldots\ldots\ldots(3.5)$$

Then by assuming that the rotor is homogenous so that all the quantities vary as $\exp(j\omega t)$, the characteristic air-gap flux equation in complex form is,

$$T_1\omega \frac{P_w^3}{\pi^3} (1 - S) \frac{d^3B_g}{dx^3} + \frac{P_w^3}{\pi^2} (1 + jT_1\omega) \frac{d^2B_g}{dx^2}$$

$$- T\omega \frac{P_w}{\pi} (1 - S) \frac{dB_g}{dx} - jT\omega B_g$$

$$= - jT\omega \frac{\rho_r \hat{J}_S}{V_S} (1 - jST_1\omega) \exp(-j \frac{\pi x}{P_w}) \ldots\ldots\ldots\ldots(3.6)$$

where, $$T = \frac{P_w^2 \mu_o}{\pi^2 \rho_r g} \qquad \ldots\ldots\ldots\ldots\ldots\ldots\ldots(3.7)$$

is the rotor coupled time constant for sinusoidal conditions,

and, $$T_1 = \frac{\ell_r}{\rho_r} \qquad \ldots\ldots\ldots\ldots\ldots\ldots\ldots\ldots\ldots(3.8)$$

is the rotor leakage time constant.

The general solution of equation (3.6) is of the form,

$$B_g = B_{g.s.s} + C_1\exp(\alpha_1 x) + C_2\exp(\alpha_2 x) + C_3\exp(\alpha_3 x)\ldots(3.9)$$

where C_1, C_2 and C_3 are found from boundary conditions and $B_{g.s.s}$ is the steady-state value given by,

$$B_{g.s.s.} = \frac{\rho_r \hat{J}_S}{SV_S} \frac{(1 + jST_1\omega)}{\left[(1 + \frac{T_1}{T} + \frac{1}{jST\omega}\right]} \exp(-j\,\frac{\pi x}{P_w}) \ldots\ldots.(3.10)$$

and α_1, α_2, α_3 are the roots of the auxiliary equation.

$$T_1 \frac{\omega P_w^3}{\pi^3}(1 - S)\ \alpha^3 + \frac{P^2}{\pi^2}(1 + jT_1\omega)\alpha^2$$

$$- T\omega\frac{P_w}{\pi}(1 - S)\alpha \quad - jT\omega \ = \ 0 \ \ldots\ldots\ldots\ldots\ldots\ldots\ldots(3.11)$$

The steady state values of B_ℓ and B may be found from equations (3.9), (3.3), (3.1) and (3.2) to be,

$$B_{\ell.s.s} = \frac{-j\ \rho_r\ T_1 \omega\ \hat{J}_S}{V_S\left[(1 + \frac{T_1}{T}) + \frac{1}{jST\omega}\right]} \exp(-j\ \frac{\pi x}{P_w}) \quad ....(3.12)$$

and

$$B_{s.s} = \frac{\rho_r\ \hat{J}_S}{SV_S\left[(1 + \frac{T_1}{T}) + \frac{1}{jST\omega}\right]} \exp(-j\ \frac{\pi x}{P_w}) \quad ....(3.13)$$

The roots of equation (3.11) may be found in any particular case by using computer techniques, but Tipping also showed that the roots were approximately,

$$\alpha_1 \doteqdot \frac{-\pi}{P_w}\left[\frac{1}{T\omega\,(1-S)^3 + T_1\omega\,(1-S)} + j\ \frac{1}{(1-S)}\right]$$

$$\alpha_2 \doteqdot \frac{-\pi}{P_w}\sqrt{\frac{T}{T_1}} = -\ \alpha_3$$

for $T\omega \gg 1$ and $T_1\omega$ of the order of unity.

Now $C_1 \exp(\alpha_1 x + j\omega t)$ represents a wave travelling at rotor speed, having a pole pitch $P_w(1 - S)$ and decaying with a space content $TV_S(1 - S)^3 + T_1V_S(1 - S)$. Relative to an observer on the rotor this wave appears stationary, has a pole pitch $P_w(1 - S)$ and decays with time constant $T(1 - S)^2 + T_1$, which is the sum of the rotor leakage time constant and the rotor coupled time constant as modified to a pole pitch of $P_w\ (1 - S)$.

Examination of the α_2, α_3 roots indicates that for conventional machines where $\frac{T}{T_1} \gg 10$, the space constant given by the real parts of the roots is of the order of 1/10 pole pitch of the excitation. The action of the α_2 and α_3 components therefore confined to the boundaries between the excited and unexcited regions. Since the imaginary part is approximately zero, the phase change over the distance where the transients act is negligible. If these results are compared with the earlier analysis, (3.6)(3.7) it is apparent that the modification introduced by the second analysis is mainly due to the rotor leakage being accounted for, since in its absence T_1 becomes zero and the time constant of the transient mainly affecting the behaviour α_1 is the same as that used in the early work. However, whilst Tipping(3.17) showed that the transients α_2, α_3 did not affect the forces very much, they do provide a step in flux density at the input edge, whereas the simpler analysis sets this to zero.

The description of Tipping's analysis has so far been confined to the excited region. If the model considered is simply a constant gap machine with an unexcited region forming the "decay section", then the equation for this section will be the same as that for the excited part but with J_S set to zero. However, practical short-stator machines usually either have the core iron confined to the excited region or have a damping grid inserted in the stator slots over the unexcited region to increase the rate of flux decay over this part of the machine. Tipping did further analytical work (3.19) to include the effects of a region with a stator damper grid and further argued with some experimental evidence that if the damper grid resistance was low, then the performance of such a machine was very nearly the same as an equivalent machine with discontinuous core. Tipping also analysed machines with stepped gaps by providing appropriate boundary conditions.

A further form of transient analysis was offered in a report by the Garrett Corporation (3.11). This makes virtually the same assumptions as the first simple analysis (3.6) (3.7) but takes leakage reactance into account. However, no rigorous method of calculating the secondary reactance is included, even though a "sheet rotor" is analysed.

It is apparent that the one-dimensional analyses are not strictly appropriate for sheet rotor machines. However, the use of these analyses can give approximate results if the rotor sheet resistivity is corrected [3.20]. The plate rotor normally used has a dimension in the direction transverse to motion which is greater than the rotor core iron. This provides "end-rings". The apparent resistivity of such secondaries has been calculated by Russell and Norsworthy [3.21]. In this approach it is assumed that the gap flux density is radial and that the rotor sheet is thin enough to neglect rotor leakage effects. It is also assumed that all the fields are sinusoidal in the direction of motion.

The analyses described so far are of the transient form. It is apparent therefore that the resistivity calculations based on sinusoidal conditions in the longitudinal direction will be difficult to apply since the transients all have different pole pitches. The previous work mentioned earlier [3.20] used the stator pole pitch as a first approximation when calculating the apparent resistivity. However, if a harmonic form of analysis is used, then the resistivity presented to each harmonic could be calculated. Hesmondhalgh and Tipping [3.19] performed such an analysis again taking a strictly one-dimensional approach and using a shorting grid to simulate the effect of the discontinuous stator iron.

3.3 A new simple approach to the analysis of short stator machines

The earlier harmonic analysis (3.19) involved the solution of a large matrix to cope with the unknown damper grid currents. As was mentioned earlier, the model with the damper grid was intended to simulate a machine with open magnetic circuit outside the excited region. In the new approach, the model for the analysis is assumed to be a constant air gap machine with a short section of excitation and a "blank section" to complete the periphery. This model is used to calculate the forces and the flux profile under the excited and unexcited regions. In order to approximate to the open magnetic circuit case, the forces developed in the uniform gap case are reduced by an amount which was earlier referred to as the exit-edge loss. To calculate this, the rate of transportation of energy across the exit-edge is calculated and from this a retarding force is derived.

3.3.1 The excitation harmonics

Fig. (3.7) shows the model with the stator excitation extending between $\frac{-q\pi}{k_p}$ and $\frac{+q\pi}{k_p}$ radians, and having

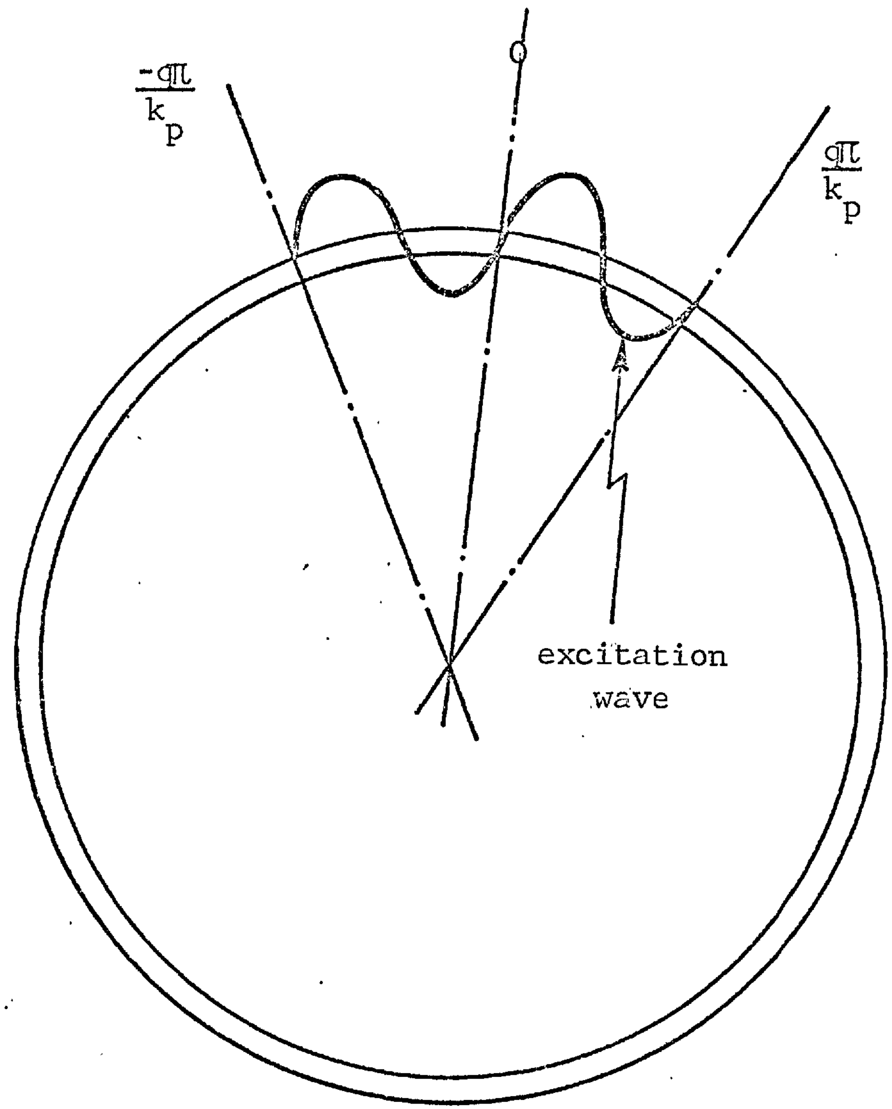

Fig. 3.7 Showing the excited region

the form $\hat{J}_S \exp\left[j(\omega t - \frac{\pi}{P_w}x)\right]$.

Using Fourier Analysis (Appendix 3.5.1) this excitation can be represented by,

$$J_S = \sum_n \hat{J}_n \exp\left[j(\omega t - \frac{\pi}{P_n}x)\right] \qquad \text{..............(3.14)}$$

where,

$$\hat{J}_n = \hat{J}_S \frac{q}{k_p} \frac{\sin \alpha_n}{\alpha_n} \qquad \text{........................(3.15)}$$

$$\alpha_n = (n - k_p)\frac{q\pi}{k_p} \qquad \text{........................(3.16)}$$

and the harmonic pole pitch,

$$P_n = \frac{k_p P_w}{n} \qquad \text{.......................... ...(3.17)}$$

$$n = \mp 1, \mp 2, \mp 3 \; .....$$

The harmonic spectrum is sketched at Fig. (3.8); it will be observed that the peak of the spectrum is at $n = k_p$ and that the pole pitch at this point is, of course, that of the original winding. Having found the excitation harmonics, the performance of the machine can be found by treating each

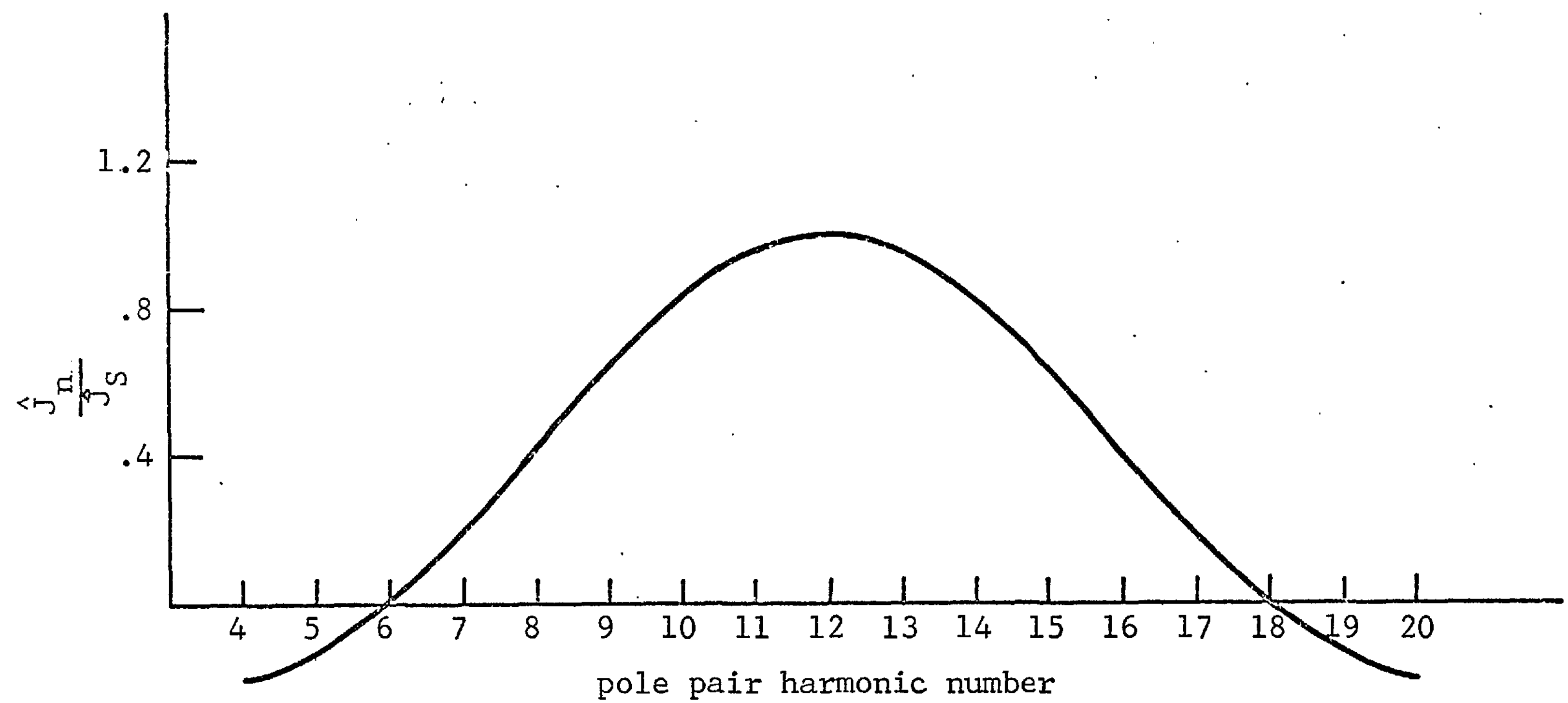

Fig. 3.8 The harmonic spectrum produced by the excitation of Fig. 3.7

excitation wave separately to find the harmonic fluxes and forces. From these the total flux and force can be found by summation.

3.3.2 The flux calculation

Using the same model as Tipping [(3.17)], that is, the Cullen and Barton model [(3.18)] shown in Fig. (3.6), the steady state flux densities on the n^{th} harmonic following equations (3.10), (3.12) and (3.13) are,

$$B_{gn} = \frac{\rho_{rn} \hat{J}_n}{S_n V_{sn}} \; \frac{(1 + jS_n T_{1n} \omega) \exp(\frac{-j\pi x}{P_n})}{\left[(1 + \frac{T_{1n}}{T_n}) + \frac{1}{jS_n T_n \omega} \right]} \qquad \text{..........(3.18)}$$

$$B_{\ell n} = - \frac{j \; \rho_{rn} \; T_{1n} \omega \; \hat{J}_n \; \exp(\frac{-j\pi x}{P_n})}{V_{sn} \left[(1 + \frac{T_{1n}}{T_n}) + \frac{1}{jS_n T_n \omega} \right]} \qquad \text{..........(3.19)}$$

and

$$B_n = \frac{\rho_{rn} \; \hat{J}_n}{S_n \; V_{sn}} \; \frac{\exp(\frac{-j\pi x}{P_n})}{\left[(1 + \frac{T_{1n}}{T_n}) + \frac{1}{jS_n T_n \omega} \right]} \qquad \text{..........(3.20)}$$

In these equations, S_n is the slip on the n^{th} harmonic given, for convenience by,

$$S_n = 1 - \frac{n}{k_p}(1 - S_k) \qquad \text{..........................(3.21)}$$

where S_k is the slip on the harmonic corresponding to the machine winding pole pitch.

The other quantities subscripted "n" are the values of the parameters particularly relating to the $n^{\underline{th}}$ harmonic. Appendix (3.5.2) shows how ℓ_{rn} and ρ_{rn} may be calculated for a squirrel-cage machine.

The previous simple form of analysis [(3.6)(3.7)] gave the flux values in terms of components in time phase and time quadrature with the winding excitation wave. Displaying the results in this fashion is also convenient from the point of view of experimental verification.

The total flux as a complex value at a general position x' can be found by taking the sum,

$$B_g = \sum_n B_{gn, x=x'}$$

$$= \hat{B}_g \exp(j\phi_1) \text{ say.}$$

Now the excitation at the point x' is given by,

$$J_S = \hat{J}_S \exp(-j \frac{\pi x'}{P_w})$$

$$= \hat{J}_S \exp(j\phi_2) \text{say}$$

and the in-phase and quadrature components can be found by resolving $\hat{B}_g \exp\left[j(\phi_1 - \phi_2)\right]$.

3.3.3 The force and voltage calculations

The harmonic forces can readily be calculated by first resolving the harmonic flux into components in space phase and space quadrature with the harmonic excitation. Thus finding the real and imaginary parts of B_{gn} yields,

$$B_{pn} = \frac{\rho_{rn}\hat{J}_n}{S_n V_{sn}} \frac{\exp(\frac{-j\pi x}{P_n})}{\left[(1 + \frac{T_{1n}}{T})^2 + (\frac{1}{S_n T_n \omega})^2\right]} \qquad \text{.................(3.22)}$$

$$B_{qn} = \frac{\rho_{rn}\hat{J}_n}{S_n V_{sn}} \frac{\left[S_n T_{1n}\omega(1 + \frac{T_{1n}}{T_n}) + \frac{1}{S_n T_n \omega}\right]}{\left[(1 + \frac{T_{1n}}{T})^2 + (\frac{1}{S_n T_n \omega})^2\right]} \exp(-j\frac{\pi x}{P_n})$$

....................(3.23)

The harmonic force is then given by,

$$\frac{1}{2}\hat{B}_{pn}\hat{J}_n \quad N/m^2 \qquad \text{.......................(3.24)}$$

whence the total force is,

$$\sum_n \frac{1}{2}\hat{B}_{pn}\hat{J}_n \quad N/m^2$$

The voltage may be calculated as follows:

The total power input may be written as,

$$P_T = A_S \sum_n \frac{1}{2}\hat{B}_{pn}\hat{J}_n V_{Sn}$$

where, A_S is the stator surface area.

Similarly, the reactive power may be written as,

$$Q_T = A_S \sum_n \frac{1}{2}\hat{B}_{qn}\hat{J}_n V_{Sn}$$

The equivalent circuit per phase may then be taken as a series combination of $(R_1 + R_2)$ and $(x_1 + x_2)$ where R_1 and x_1 are the stator per phase resistance and leakage reactance respectively, and R_2 and x_2 are given by,

$$R_2 = \frac{P_T}{3I_{ph}^2}$$

$$x_2 = \frac{Q_T}{3I_{ph}^2}$$

where I_{ph} is the r.m.s. phase current.

The input voltage may then be calculated from the equivalent circuit.

3.3.4 An experimental machine

It has been argued for an idealised case in reference (3.6) that the rotor resistivity for a short-stator machine should be high compared with its conventional counterpart. The ratio of rotor coupled time constant (T) to rotor transit time (t_s) under the excited region is thus commonly in the range 1 to $\frac{1}{2}$. The experimental model accordingly used high resistance rotor bars so that (t_s/T) was (1.85) at (200)Hz. The rotor was constructed so that the rotor bar position in the slot could fairly readily be changed to enable the effects of different rotor leakage to be investigated. The air-gap was constant and the four pole stator winding which used (12) of the (72) stator slots was of the form shown in Fig. (3.9). This particular form of winding uses a "three plane" end winding construction which is unusual in rotary machines but which is apt in short arc windings since it is complete in two pole pitches.

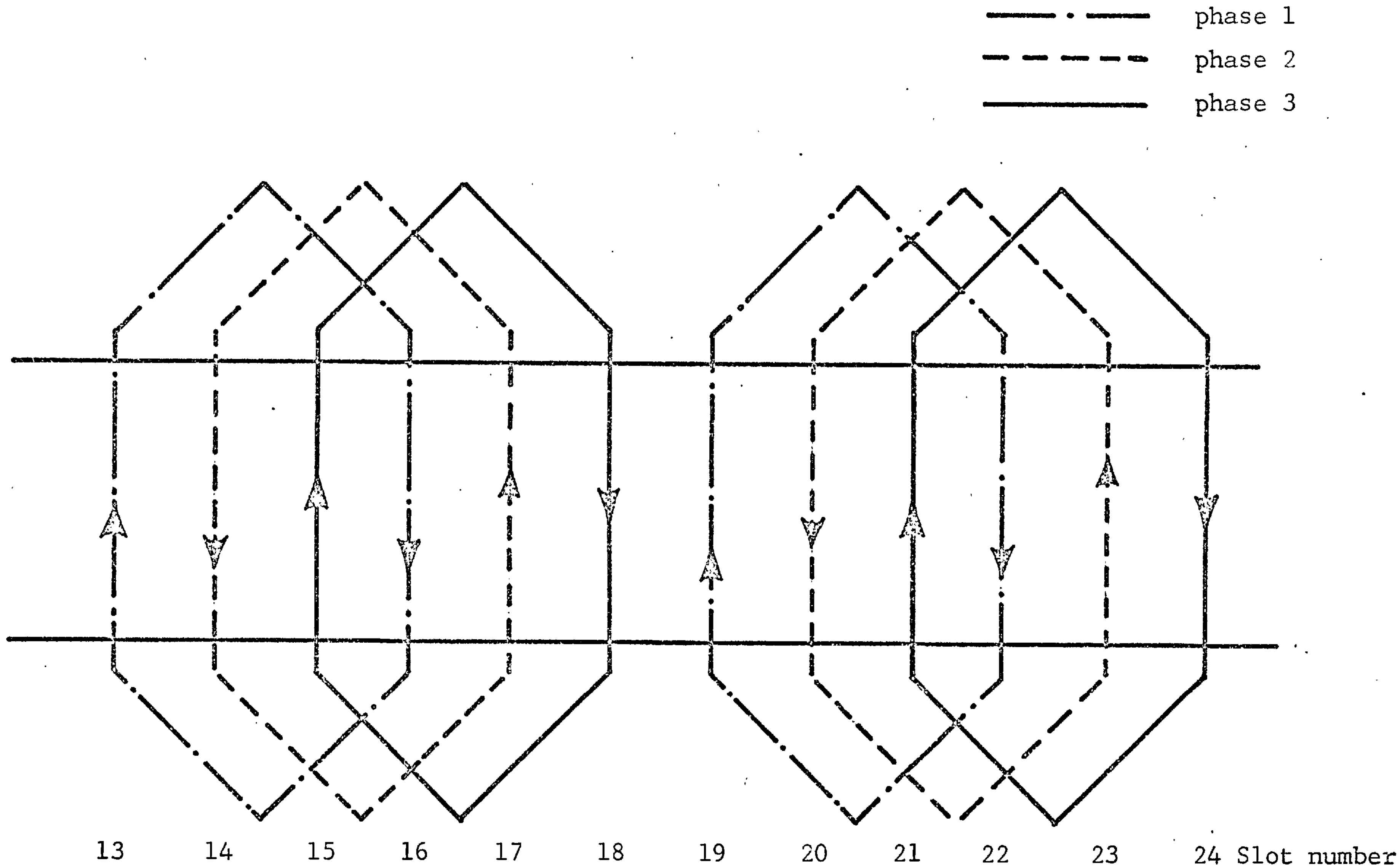

Fig. 3.9 The experimental machine winding

3.3.5 Experimental results for the uniform gap short stator machine

One of the more difficult parameters to calculate in induction machine analysis is the stator end winding leakage reactance. Accordingly the experiments were performed at constant input current so that the predicted and measured results could be compared without a knowledge of the stator leakage reactance. However, prediction at constant voltage is more desirable than the prediction at constant current. Thus the voltage-speed curve at constant current was also calculated for comparison with the measured results using measured values of stator leakage reactance and resistance.

The constant current results can therefore be scaled to give the constant voltage performance. Figures (3.10) and (3.11) show flux profiles at synchronous speed for the low and high rotor leakage respectively. The profiles are plotted resolved, as explained earlier, into in-phase and quadrature components. The resolution method for the experimental points follows that explained in reference (3.22) and is outlined in Appendix (3.5.3). The full lines on the graphs represent the theoretical results and it will be

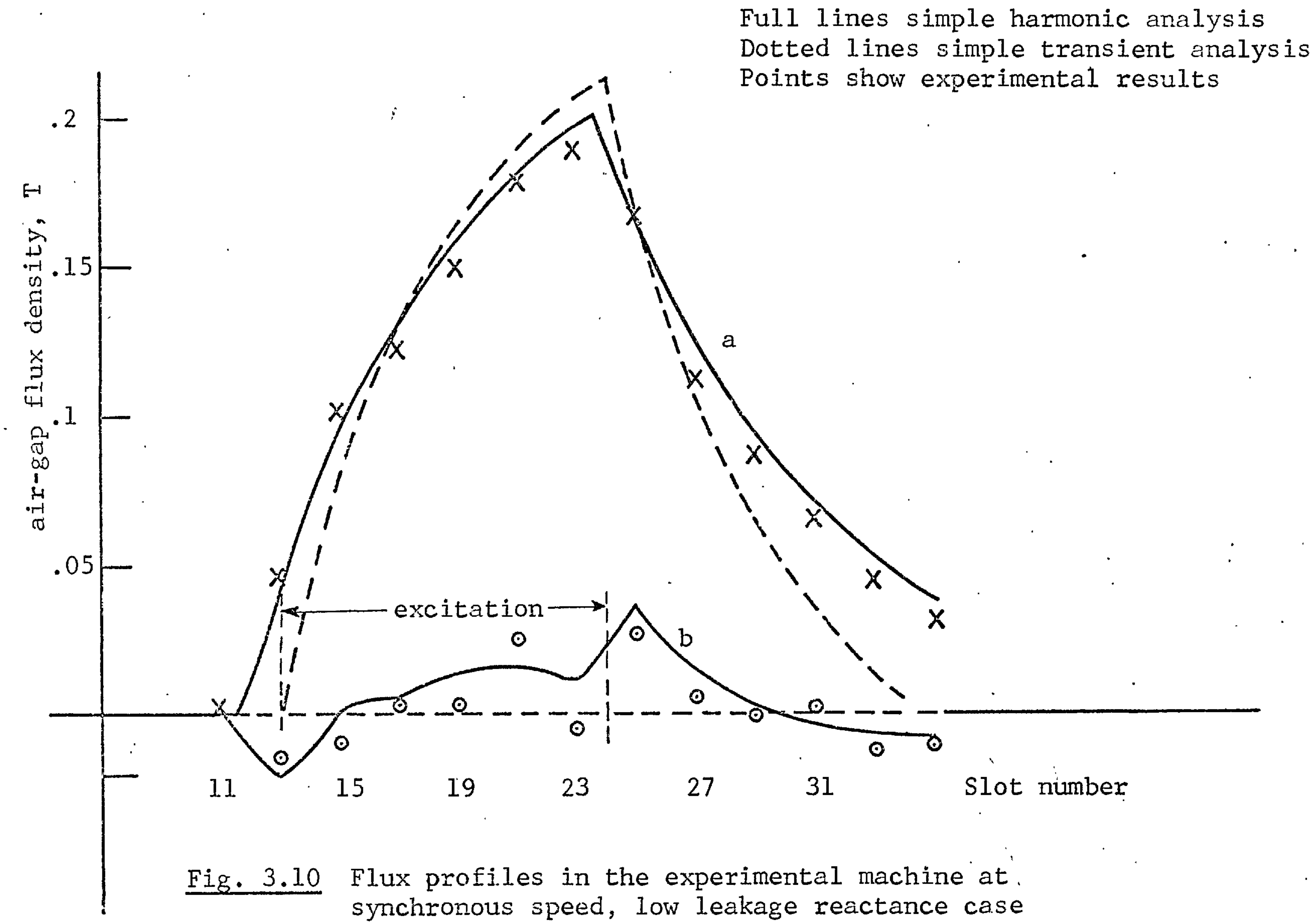

Fig. 3.10 Flux profiles in the experimental machine at synchronous speed, low leakage reactance case

(a) B_q (b) B_p

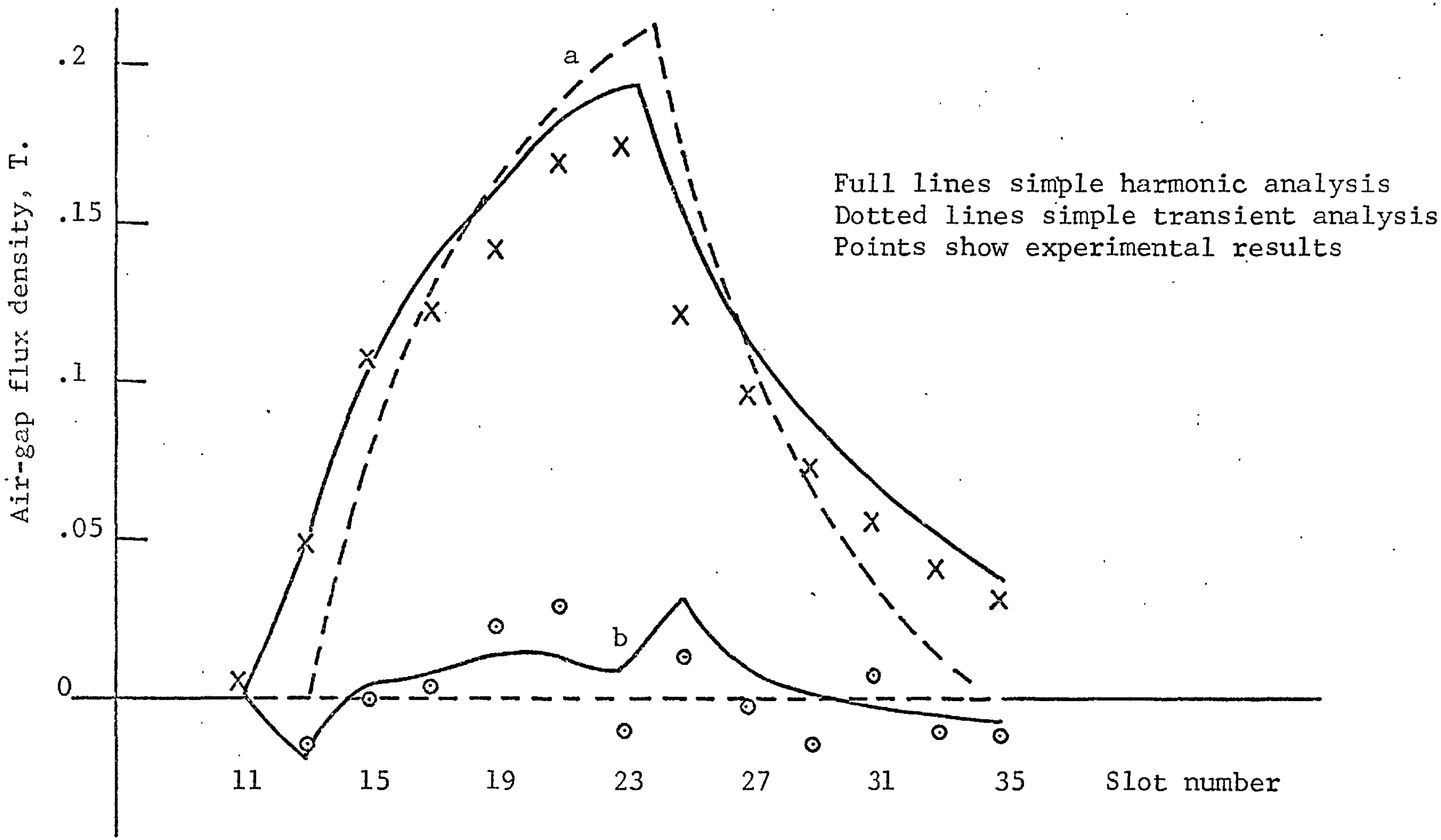

Fig. 3.11 Flux profiles in the experimental machine at synchronous speed, high leakage reactance case.

(a) B_q (b) B_p

observed that the agreement is generally good. The dotted lines on the graphs show the results of applying the early simple theory (3.6)(3.7) to this case, B_q is an exponential rise whilst B_p is zero. The chief difference is in the "input step" of flux predicted by Tipping (3.17) due to the fast moving transients at the region boundaries. (The early analysis (3.6)(3.7) had a zero flux density at entry as a boundary condition.) The correlation between the B_p predictions and measured values is not as good as the B_q predictions. The B_p values are, however, very small and the differences are most likely due to the measurement of small angle differences, although it must be remembered that the harmonic content of the excitation wave (which was assumed to be sinusoidal in the analysis) could also be affecting these results.

Fig. (3.12) shows the theoretical torque-speed curves plotted at constant current for the two leakage reactance cases together with the earlier simple theory (3.6)(3.7) prediction. It can be seen that the inclusion of leakage reactance is of some importance. Figures (3.13) and (3.14) show the correlation between the theoretical and practical torque and input voltage characteristics; it will again be noted that the correlation is good.

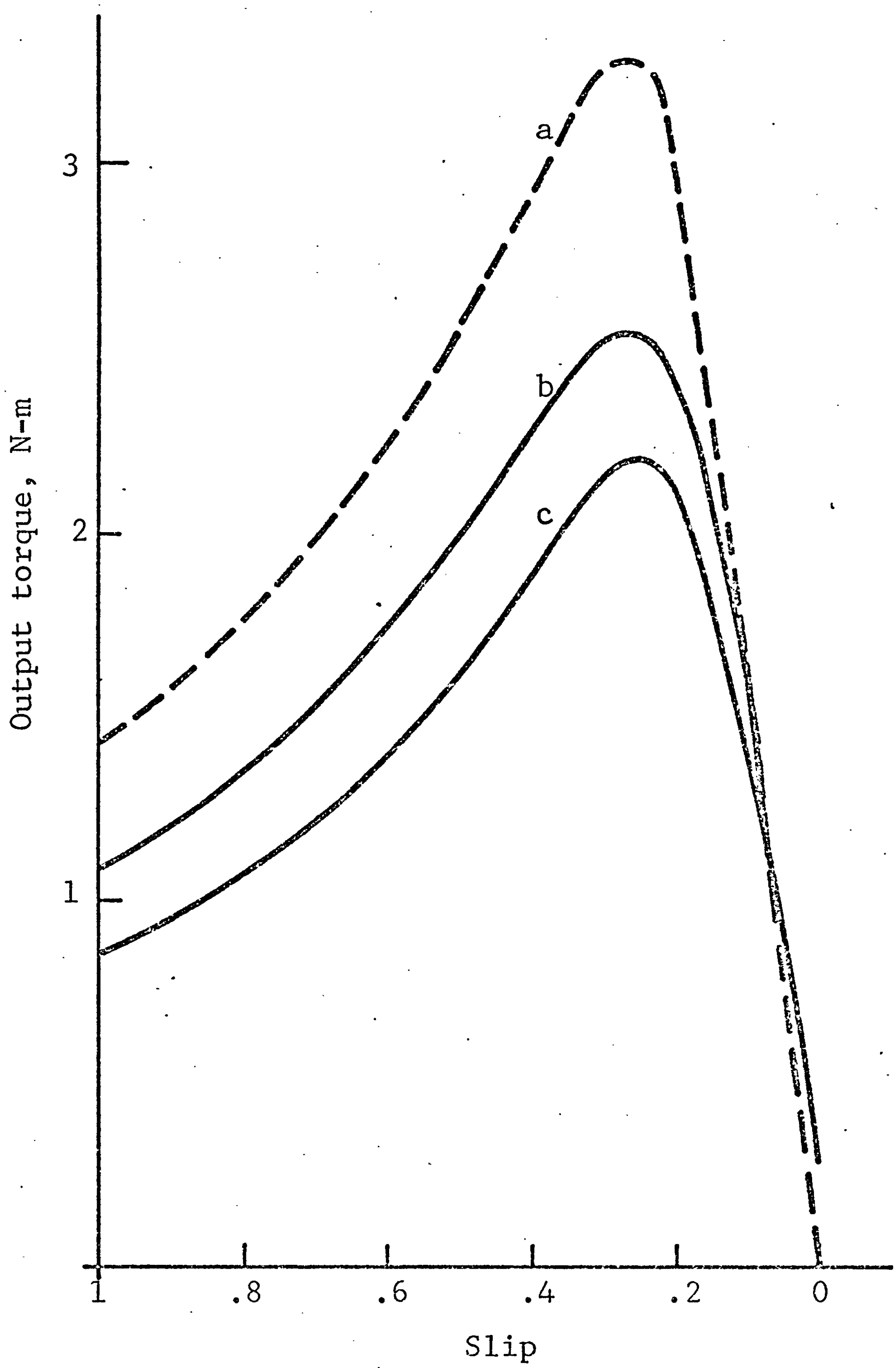

Fig. 3.12 Theoretical torque-speed curves.

(a) Simple transient analysis (no leakage reactance allowance)

(b) Simple harmonic theory, low leakage reactance case

(c) Simple harmonic theory, high leakage reactance case.

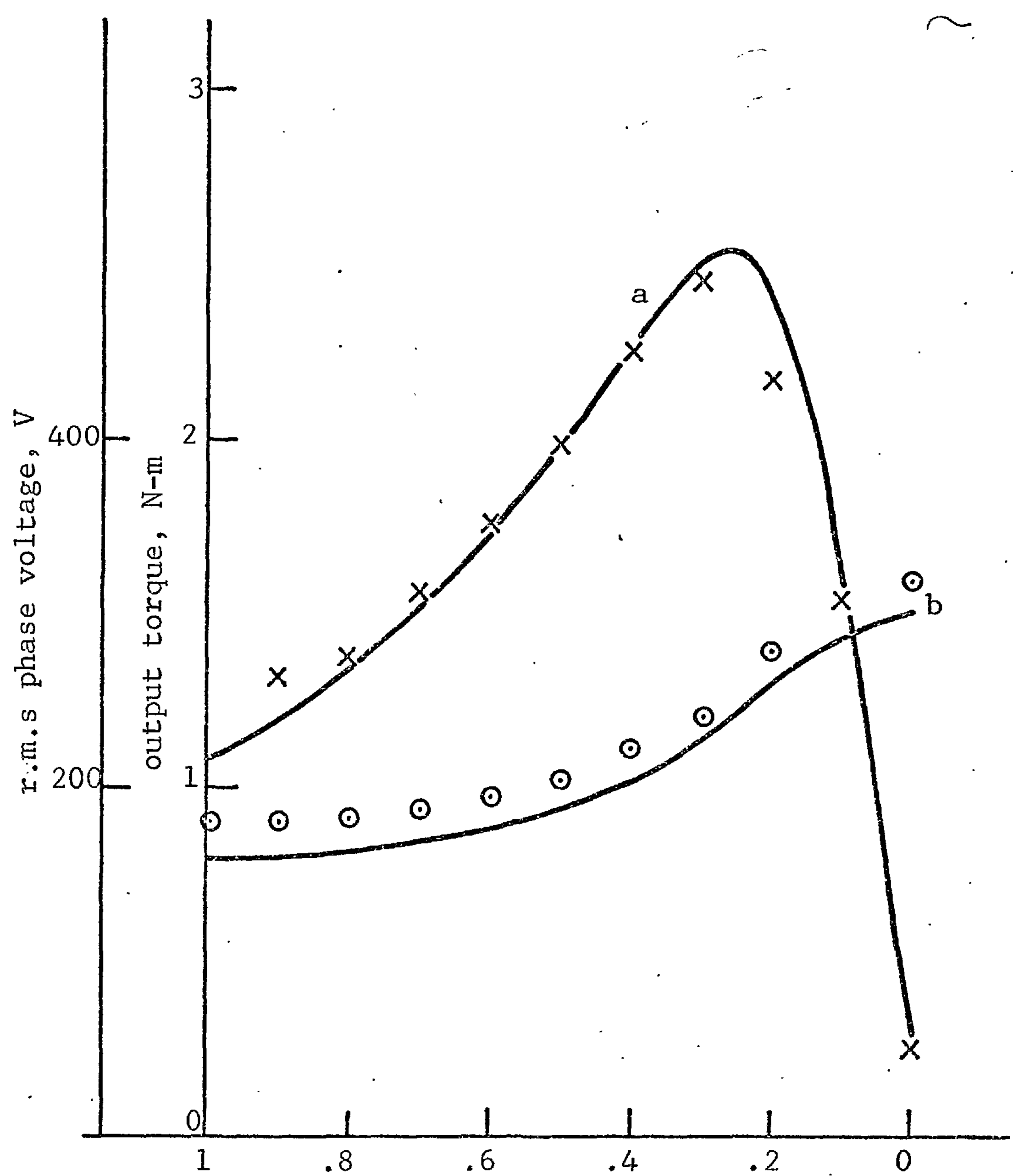

Fig. 3.13 The correlation between the simple harmonic theory and the experiment, low leakage reactance case.

(a) Output torque
(b) Terminal voltage

Lines show the theory points the experimental values.

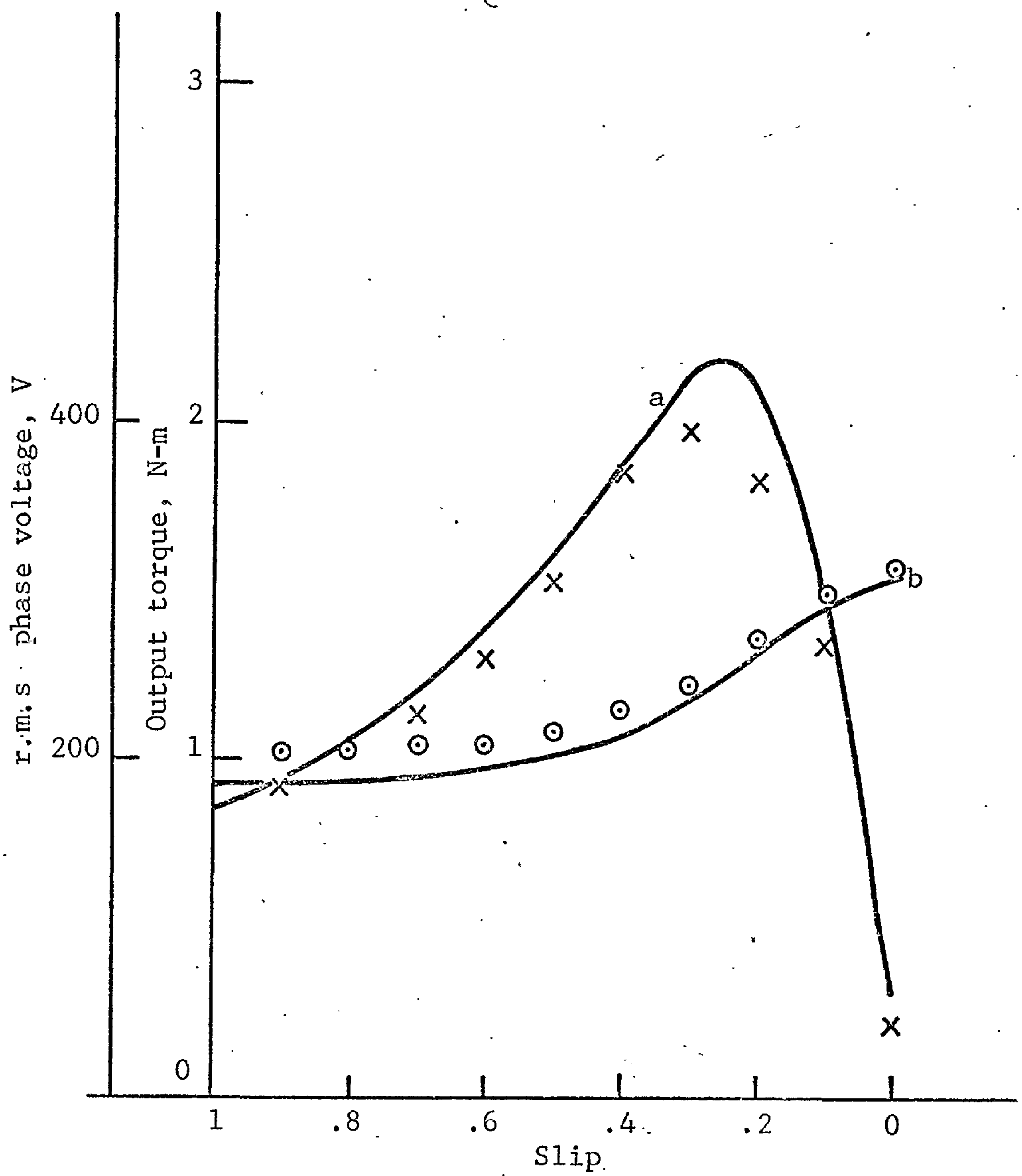

Fig. 3.14 The correlation between the simple harmonic theory and the experiment, high leakage reactance case.

(a) Output torque
(b) Terminal voltage

Lines show the theory, points the experimental values.

3.3.6 Exit-edge effects

The preceding harmonic theory assumes a uniform air-gap and the analysis is rigorous for this case assuming that the electromagnetic model (Fig. (3.6)) is an accurate representation. However, practical short stator machines commonly have an open magnetic circuit outside the excited region. As a first step in considering this problem a step in the air gap will be considered, as shown in Fig. (3.15). It is assumed that whilst the ratio between the gap outside the excitation to that inside may be large, the length of the outside gap is sufficiently small to assume that the flux lines away from the immediate vicinity of the discontinuity are radial. As a rotor element approaches the end of the excitation it will in general be threaded by flux. The element must retain this flux as it crosses the discontinuity. Since there is now no stator current the rotor current must be sufficient to maintain this flux. The flux will decay exponentially as the element moves on owing to dissipation in the rotor conductors.

If the air-gap is uniform, then the energy transported across the boundary is, of course, the same as the total rotor copper loss outside the excited region. This energy comes from the supply and for the uniform gap case, therefore,

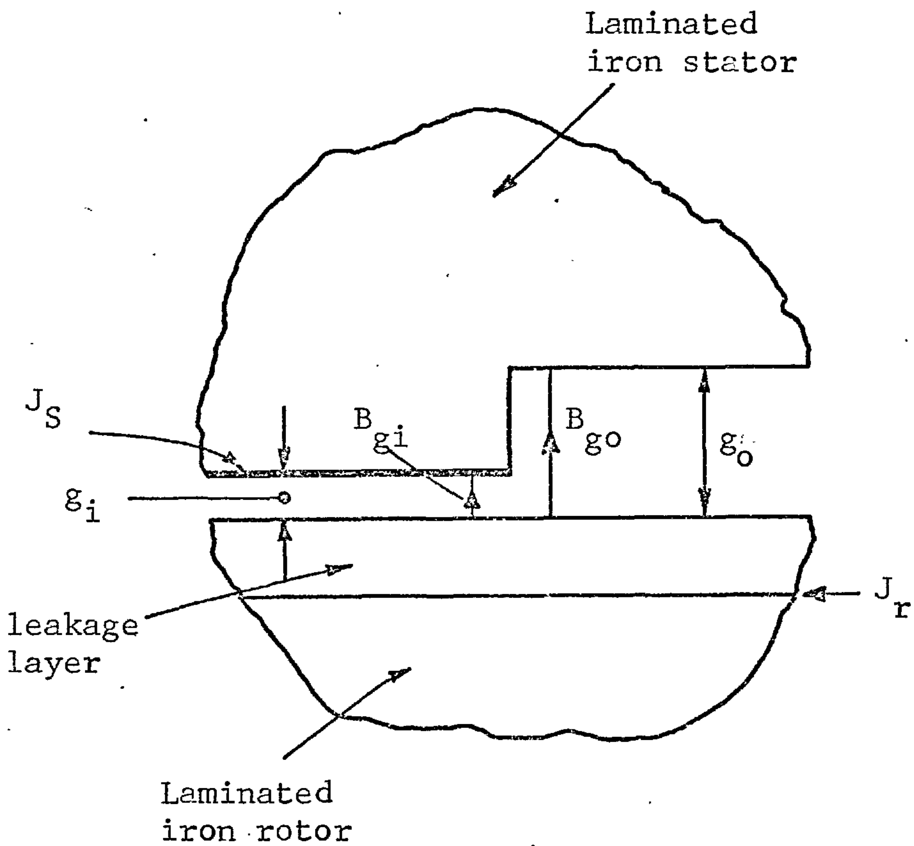

Fig. 3.15 Illustrating the conditions at a step in the air-gap

the presence of the exit-edge will not modify the output characteristic calculated. However, if the air-gap increases outside the excited region, the rotor current necessary to maintain the flux at its exit-edge value will be increased, resulting in an increase in the rotor copper loss outside the excited region. The increase in this loss cannot come from the supply but must be produced by a retarding torque on the rotor.

Reference (3.16) calculates the exit-edge loss for the case with no rotor leakage by finding the rotor copper loss outside the block as follows. For an exit-edge flux density of B_{gx} which must be maintained immediately beyond the excited region the rotor current loading required is given by,

$$J_{ro} = \frac{g_o \pi}{P_o \mu_o} B_{gx} \qquad \text{.........................(3.25)}$$

assuming that the flux is radial and sinusoidally distributed. These assumptions are, of course, not strictly valid. However, the flux in the region immediately beyond the gap step is a complicated two-dimensional pattern and in the absence of more rigorous approach the approximation was taken in the reference. The reference further assumed that the rotor current will decay according to the formula,

$$J_r = J_{ro} \exp\left(- \frac{x}{T_o V} \right) \qquad \text{.......................(3.26)}$$

where $V = V_s(1 - S)$ is the rotor speed and

T_o is the rotor coupled time constant outside the block, given by,

$$T_o = \frac{P_o^2 \ \mu_o}{\pi^2 \rho_r g_o} \qquad \text{.......................(3.27)}$$

Thus the reference calculated the rotor copper loss outside the excited block as,

$$\frac{1}{2} \rho_r \int_o^{\infty} J_{ro}^2 \ \exp\left(- \frac{2x}{T_o V}\right) dx = \frac{B_{gx}^2 \ g_o V}{4 \mu_o}$$

As was indicated earlier, a part of this loss equal to $\frac{B_{gx}^2 \ g_i V}{4 \mu_0}$ is provided from the supply. The remaining portion,

$$\frac{B_{gx}^2 \ V}{4 \mu_o} (g_o - g_i) \qquad \text{.......................(3.28)}$$

produces a retarding torque. This torque may be used to modify the torque characteristics obtained from the analysis with a constant gap so that it approximates to the stepped gap case.

Now reference (3.16) assumed no leakage, and the time constant outside the excited region was calculated on this basis. However, the new harmonic analysis includes leakage reactance and it is necessary to re-examine the retarding torque calculations in this light. If the electromagnetic model (Fig. 3.6) is considered, then as a rotor element leaves the excited region then it is apparent that the flux threading the element, B, must remain constant. The rotor current loading required to drive this flux can be calculated as follows.

Firstly, if the leakage layer is considered, then, following equation (3.1), we have,

$$B_{\ell o} = - \ell_r \frac{\partial J_{ro}}{\partial x}$$

where subscript "o" refers to the unexcited region.

Then, making the assumptions of reference (3.16), which is that the flux is sinusoidal in space, we have,

$$B_{\ell o} = \frac{j\pi}{P_o} \ell_r J_{ro} \qquad \text{.....................(3.29)}$$

Secondly, the gap flux may be considered and following equation (3.3),

$$\frac{g_o}{\mu_o} \frac{\partial B_{go}}{\partial x} = J_{ro}$$

or $$B_{go} = \frac{jP_o}{\pi} \frac{\mu_o}{g_o} J_{ro} \qquad \text{. ....(3.30)}$$

Now the flux through the element is given by,

$$B_o = B_{go} + B_{\ell o} \qquad \text{.....................(3.31)}$$

so that

$$B_o = \frac{jP_o \mu_o}{g_o \pi} \left[1 + \frac{\ell_r \pi^2}{\mu_o P_o^2} g_o \right] J_{ro} \qquad \text{..........(3.32)}$$

and the current density J_{ro} required to drive the flux B_o can be written,

$$J_{ro} = \frac{g_o \pi}{jP_o \mu_o} \left[\frac{1}{1 + \frac{\ell_r \pi^2}{\mu_o P_o^2}} \right] B_o \qquad \text{..........(3.33)}$$

Having calculated J_{ro} the rotor copper loss can be calculated as in the earlier case, but using the time constant outside the excited region as,

$$T_o = \frac{P_o^2 \mu_o}{\pi^2 \rho_r g_o} + \frac{\ell_r}{\rho_r} \qquad \text{......................(3.34)}$$

This yields a loss $= \dfrac{B_x^2 g_{oe} V}{4 \mu_o}$

$$\text{where } g_{oe} = \frac{g_o}{1 + \dfrac{\ell_r \pi^2}{\mu_o P_o^2} g_o} \qquad \text{...................(3.35)}$$

g_{oe} of course becomes g_o as ℓ_r tends to zero.

The retarding torque is produced by the difference between this loss and the loss which would have occurred if no step existed, that is, by,

$$\frac{B_x^2 V}{4 \mu_o} (g_{oe} - g_{ie}) \qquad \text{........................(3.36)}$$

$$\text{where } g_{ie} = \frac{g_i}{1 + \dfrac{\ell_r \pi^2}{\mu_o P_o^2} g_i} \qquad \text{........................(3.37)}$$

Equation (3.36) will reduce to equation (3.28) if ℓ_r tends to zero.

It will be noted that the above technique is by no means rigorous. The field under the excited region has been calculated on the basis of a uniform air-gap. Now strictly speaking this field will be modified under the excited region when the gap is increased outside due to different "boundary matching" conditions. However, as a first approximation this modification has been ignored and the exit-edge value of B calculated on the uniform gap basis.

The considerations in this section have so far been confined to stepped gap machines. When an arc-stator case is considered it is apparent that there is a difficulty in ascribing a value to g_o. However, several authors(3.19)(3.20)(3.17) have considered the analysis of a model consisting of a thin sheet of excitation located on a laminated iron boundary and facing free space. The conditions outside the excited region of an arc-stator machine approximate to the above model with the rotor current providing the excitation. Reference 3.20, page 161 in particular shows that the effective air-gap "seen" by such an excitation is $\frac{P_w}{\pi}$ where P_w is the winding pole pitch. The calculation therefore for the exit-edge loss for an arc-stator machine can be performed approximately as before by replacing g_o by $\frac{P_w}{\pi}$.

3.3.7 Experimental results for an arc-stator machine

The experimental model of section (3.3.4) was modified by removing the stator core and teeth over the unexcited region. Tests were then performed on the same basis as before to check the above theory. Fig. (3.16) compares the theoretical and practical torque-slip characteristics and it will be observed that the agreement is good. The input voltage characteristic is also shown on the figure. This voltage has been calculated on the basis of uniform gap, since the correction for the exit-edge loss has been confined to the torque calculations. It can be seen from the figure that the voltage prediction has good correlation with the experimental points.

3.4 Conclusions

The theory presented in this chapter is extremely simple to compute and within its one-dimensional limitation gives extremely useful results. Since the computation time is short, it is a considerable aid to design, since many possible configurations may be quickly checked. As has been previously indicated, this form of analysis is

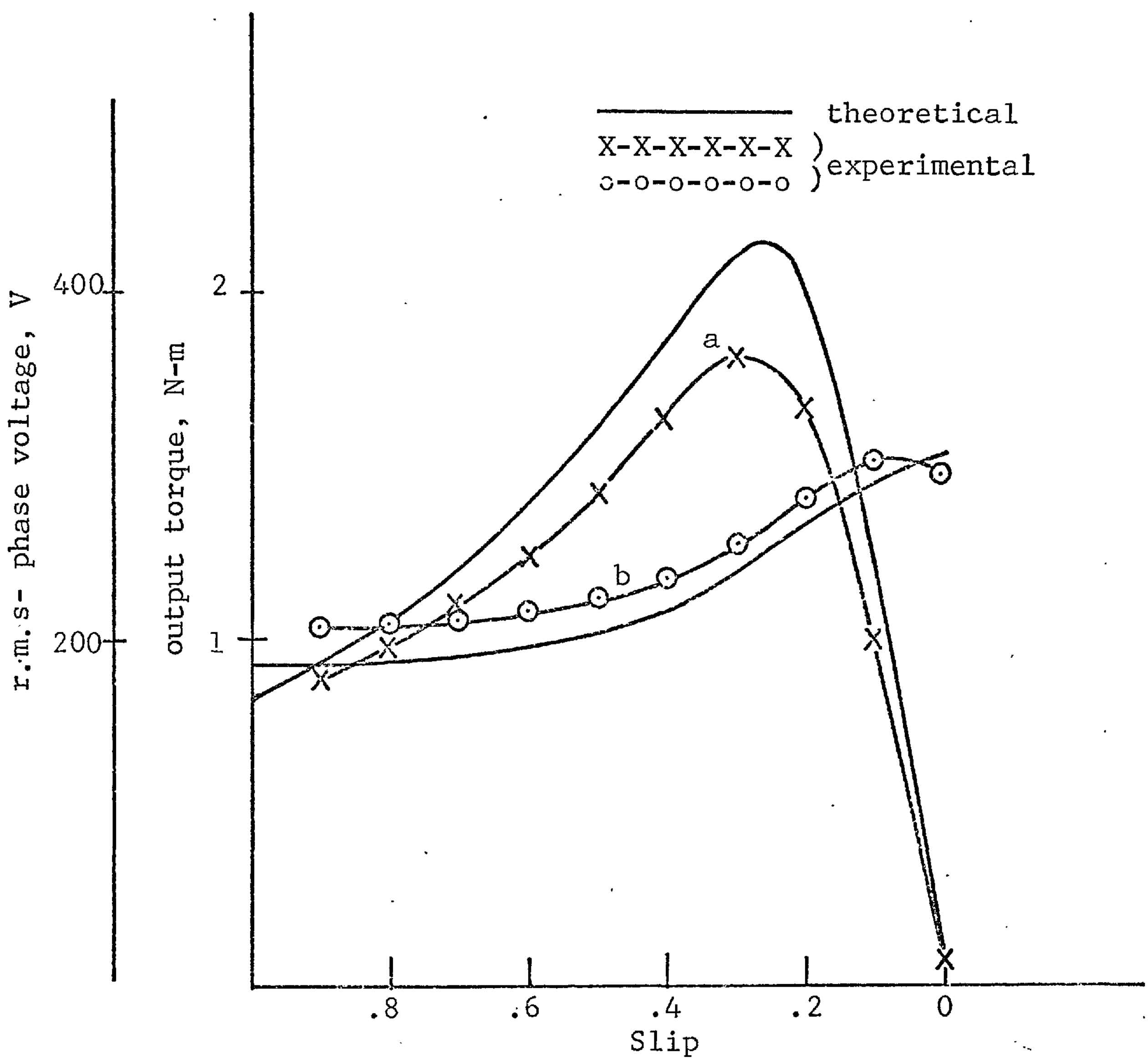

Fig. 3.16 The characteristics of a short-arc machine using the simple harmonic theory with allowance for exit-edge losses

(a) Torque
(b) Terminal voltage

useful for linear motors with plate rotors if an estimate of the effective rotor impedance can be made. However, the theory is not in any sense rigorous, nor can it be applied to the interesting cases where the outside gap is shaped. It was thought therefore appropriate to attempt a more rigorous approach adaptable to any gap shape. This second new theory is given in the next chapter.

3.5 Appendices

3.5.1 Fourier Analysis of the excitation current sheet

Fig. (3.7) shows the excitation, which extends between $\frac{-q\pi}{k_p}$ and $\frac{+q\pi}{k_p}$ radians. This excitation is assumed to be of the form,

$$J_S = \hat{J}_S \exp\left[j(\omega t - k_p x)\right] \qquad \text{.....................(3.38)}$$

where x is measured in radians.

Using Fourier Analysis, the excitation may be represented as a sum of harmonic excitations acting on the range $-\pi$ to $+\pi$ radians,

$$J_S = \hat{J}_S \exp(j\omega t) \sum_{n=-\infty}^{+\infty} A_n \exp(-jnx) \qquad \text{.............(3.39)}$$

where,
$$A_n = \frac{1}{2\pi} \int_{\frac{-q\pi}{k_p}}^{\frac{q\pi}{k_p}} \exp(-jk_p x) \exp(jnx) dx$$

$$= \frac{q}{k_p} \frac{\text{Sin}(\alpha_n)}{\alpha_n}$$

and,
$$\alpha_n = (n - k_p) \frac{q\pi}{k_p} \qquad \text{........................(3.40)}$$

Therefore, equation (3.39) becomes,

$$J_S = \sum_{n=-\infty}^{+\infty} \hat{J}_n \exp\left[j(\omega t - nx)\right] \qquad \text{...............(3.41)}$$

where, $\hat{J}_n = A_n \hat{J}_S$ ....(3.42)

Equation (3.41) may be re-written with x in metres rather than radians, as,

$$J_S = \sum_{n=-\infty}^{+\infty} \hat{J}_n \exp\left[j(\omega t - \frac{\pi}{P_n}x)\right] \qquad \text{..............(3.43)}$$

where $P_n = \frac{k_p P_w}{n}$ is the pole pitch for the n^{th} excitation harmonic.

3.5.2 The calculation of an equivalent surface impedance for the squirrel-cage rotor

The harmonic analysis assumes that at each particular excitation harmonic, a sinusoidally distributed flux exists in the air-gap. This flux induces sinusoidal currents in the rotor bars, the r.m.s. values of which can be represented by phasors. The phasors of two adjacent bars are displaced by the slot angle at the particular harmonic considered,

$$\theta_n = \frac{2n\pi}{N_2} \qquad \text{.........................(3.44)}$$

The end ring segments between the bars make, with respect to the bars at each particular harmonic, a polygonal mesh of impedance, the external line currents of which are the bar currents. Due to the symmetry of the cage, the current distribution in the ring is also sinusoidal in space and its r.m.s. value can be represented by phasors. The phasors of adjacent segments are also displaced by the harmonic slot angle θ_n.

Fig. (3.17a) shows a few bars and ring segments; Fig.(3.17b) shows the current phasor diagram. If the $n^{\underline{th}}$ harmonic of the bar current is denoted in general by I_{bn} and the ring current by I_{rn}, it follows from Fig. (3.17c) that,

$$I_{bn} = I_{rn} \; 2\mathrm{Sin}\left[\frac{\theta_n}{2}\right] \qquad \text{....................(3.45)}$$

The copper losses in the cage for the $n^{\underline{th}}$ harmonic are,

$$L_{Cn} = N_2(I_{bn}^2 \; r_b + 2I_{rn}^2 \; r_r) \qquad \text{...............(3.46)}$$

Fig. 3.17 Illustrating the calculation of the effective rotor parameters for a squirrel-cage motor

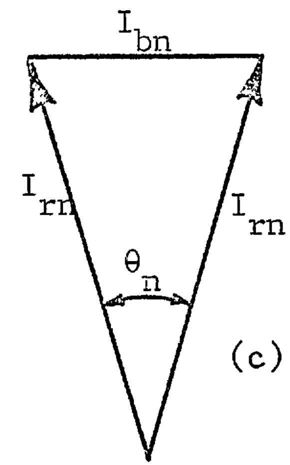

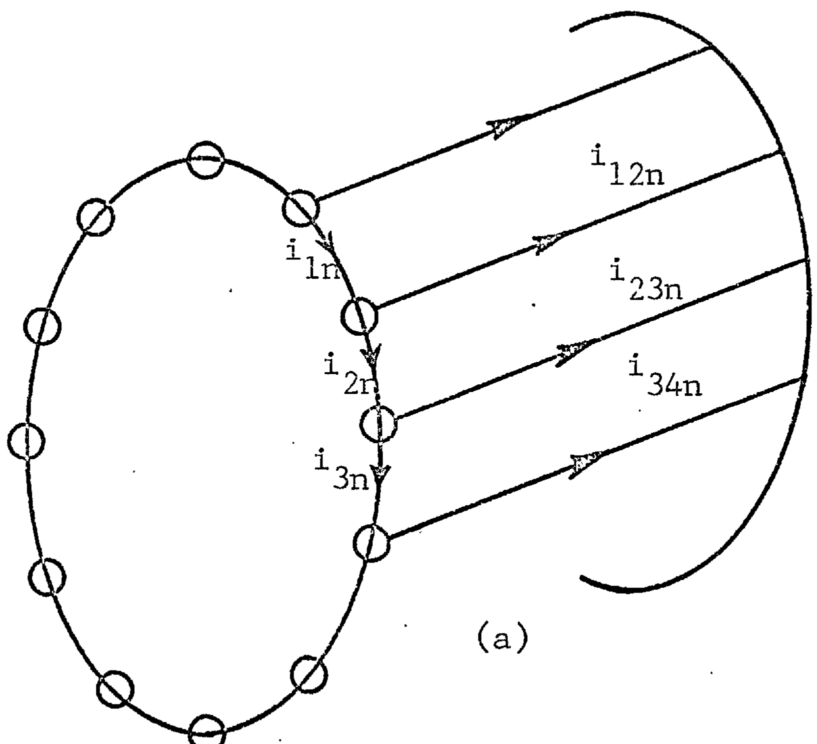

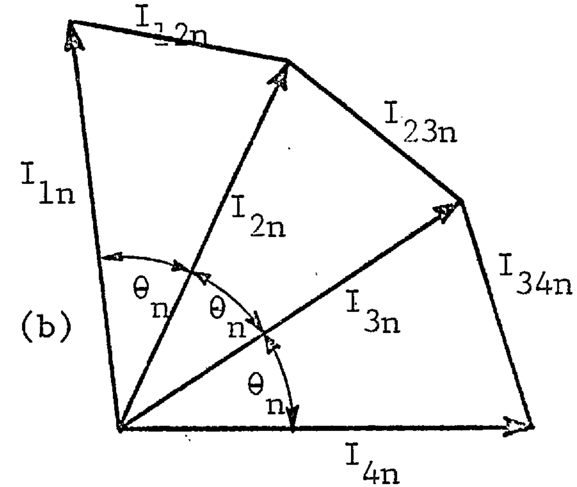

r_b and r_r are the resistances of a single bar and of a single segment respectively.

Substituting for I_{rn} from (3.45) into (3.46),

$$L_{Cn} = N_2 I_{bn}^2 r_{ben} \qquad \text{.........................(3.47)}$$

where

$$r_{ben} = r_b + \frac{r_r}{2 \operatorname{Sin}^2 \left[\frac{\theta_n}{n}\right]} \qquad \text{....................(3.48)}$$

r_{ben} is the equivalent bar resistance for the $n^{\underline{th}}$ harmonic which also takes into account the ring segments.

The rotor leakage reactance may be calculated in the same manner as above, yielding an equivalent bar reactance,

$$x_{ben} = x_b + \frac{x_r}{2 \operatorname{Sin}^2 \left[\frac{\theta_n}{2}\right]} \qquad \text{....................(3.49)}$$

Now, the squirrel-cage rotor may be represented by an equivalent sheet rotor with a surface resistivity of ρ_{rn}, and surface inductance ℓ_{rn}. The appropriate surface current density then has a peak value,

$$\hat{J}_{rn} = \frac{\hat{I}_{bn}}{\left(\frac{2\pi R}{N_2}\right)} \quad \text{.........................(3.50)}$$

ρ_{rn} may be calculated by equating the copper losses in the sheet to those in the cage,

$$\frac{1}{2} \, \rho_{rn} \, \hat{J}_{rn}^2 = \frac{1}{2} \, \hat{I}_{bn}^2 \, r_{ben} . N_2$$

to give

$$\rho_{rn} = \frac{(2\pi R)^2}{N_2} \, r_{ben} \quad \text{.........................(3.51)}$$

Similarly,

$$\ell_{rn} = \frac{(2\pi R)^2}{\omega N_2} \, x_{ben} \quad \text{.........................(3.52)}$$

3 5.3 Resolution of measured flux profile into components in time phase and in quadrature with the current sheet

A resistance of (.0251) ohms was connected in the red phase at the star point and the potential difference across this resistance used as a phase reference.

Figure (3.18) is a space diagram showing the positions of the current and flux wave when the flux is wholly

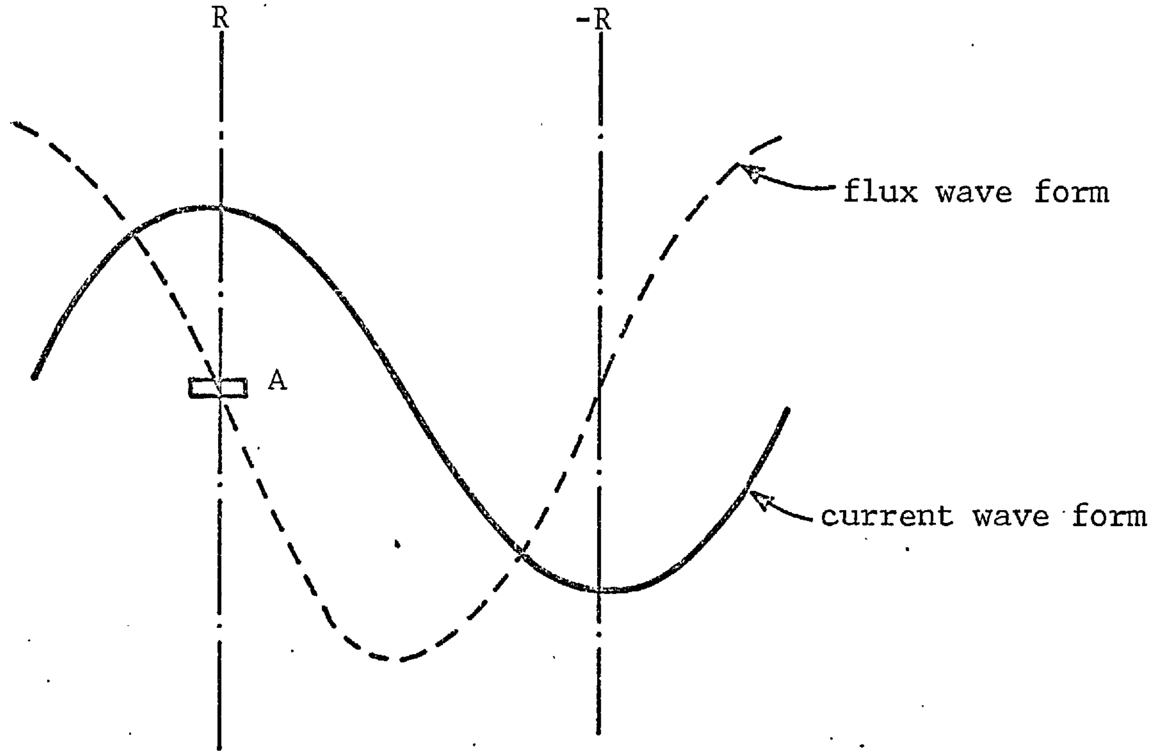

Fig. 3.18 Space diagram.

reactive. The diagram is drawn for the particular instant of time when the red phase current has its maximum value. It can be seen that the e.m.f. induced in a coil at A is in anti-phase in time to the red current; hence if the flux were wholly reactive, that is, if it had no B_p component, the e.m.f. induced in the search coil positioned over the slot which carries a red conductor will be in anti-phase to the reference voltage.

The search coils are positioned at ($\frac{2\pi}{3}$) radian intervals along the current wave and therefore the phase relationship between any coil and the reference voltage is known, for the case of wholly reactive flux.

The method of resolving the flux at a particular coil position is then as follows if:

θ_R is the phase reference.

θ_v is the phase of the measured search coil voltage.

V_{1s} is the magnitude of the measured search coil voltage, converted into flux density units.

γ is the phase relationship between the coil and the reference voltage for the case of wholly reactive flux.

Then $$V_{1s}\cos\left[\gamma - (\theta_v - \theta_R)\right] = B_q \qquad \text{.............(3.53)}$$

and $$V_{1s}\sin\left[\gamma - (\theta_v - \theta_R)\right] = B_p \qquad \text{.............(3.54)}$$

CHAPTER FOUR

THE USE OF PERMEANCE HARMONICS
IN THE ANALYSIS OF
SHORT-STATOR MACHINES

4.1 Introduction

The harmonic analysis presented in the previous chapter analysed a short stator machine by assuming initially that the air-gap was constant around the periphery. The effect of discontinuous core iron was then accounted for by a method which was not in any way rigorous. It is the object of this chapter to present a more rigorous approach to test the earlier simple method analytically and again to check the results against experimental findings.

The model chosen for the analysis is again one-dimensional and it is again assumed that circumferential components of flux are absent in the air-gap, i.e. the field does not vary in the radial direction. Again in line with the previous approach it is assumed that the rotor can be represented by a conducting sheet which has surface values of resistance and leakage inductance. These values are calculated for a particular harmonic if the rotor is of squirrel cage form with reference to the bar and end-ring impedances by equating equivalent complex powers as shown in Section (3.5.2).

The air-gap length considered by the analysis which follows may be any general function; the particular shapes of interest are those which most closely model an arc-stator. For example, Fig. (4.1) shows a case where the gap is stepped so that the air-gap in the unexcited region is large. Fig. (4.2) shows as a second example a case in which the air-gap is gradually increased outside the excited region. It has been argued (4.1) that this shape may reduce the effect of the exit-edge losses by limiting the rotor current step immediately outside the excited region.

The analysis is performed by again resolving the excitation into a series of harmonics of the same form as in the previous chapter. In addition, the air-gap is also represented by a harmonic series. In this case the machine permeance or reciprocal air-gap length is resolved.

As a first step in the development of the theory the excitation is considered to act on the air-gap when no rotor conductor is present. Thus each component of excitation is considered to act on each component of permeance to produce flux density distributions. In essence a particular $n^{\underline{th}}$ excitation harmonic produces flux waves on each harmonic mode. It gives an $n^{\underline{th}}$ harmonic flux when acting on the average gap and also side-band

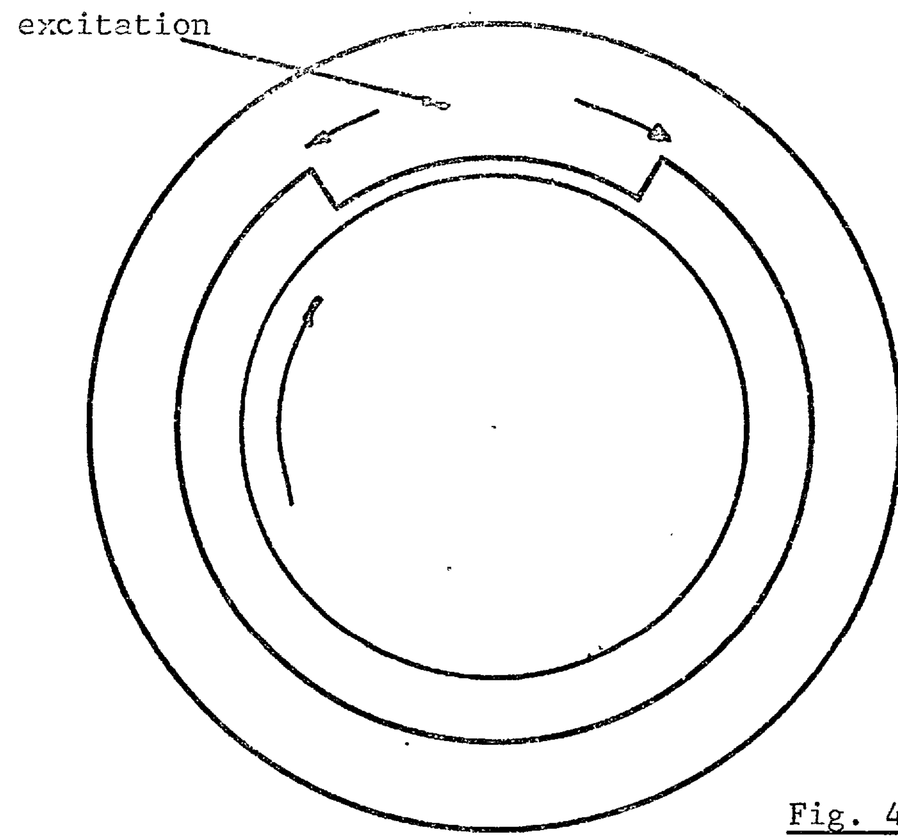

Fig. 4.1

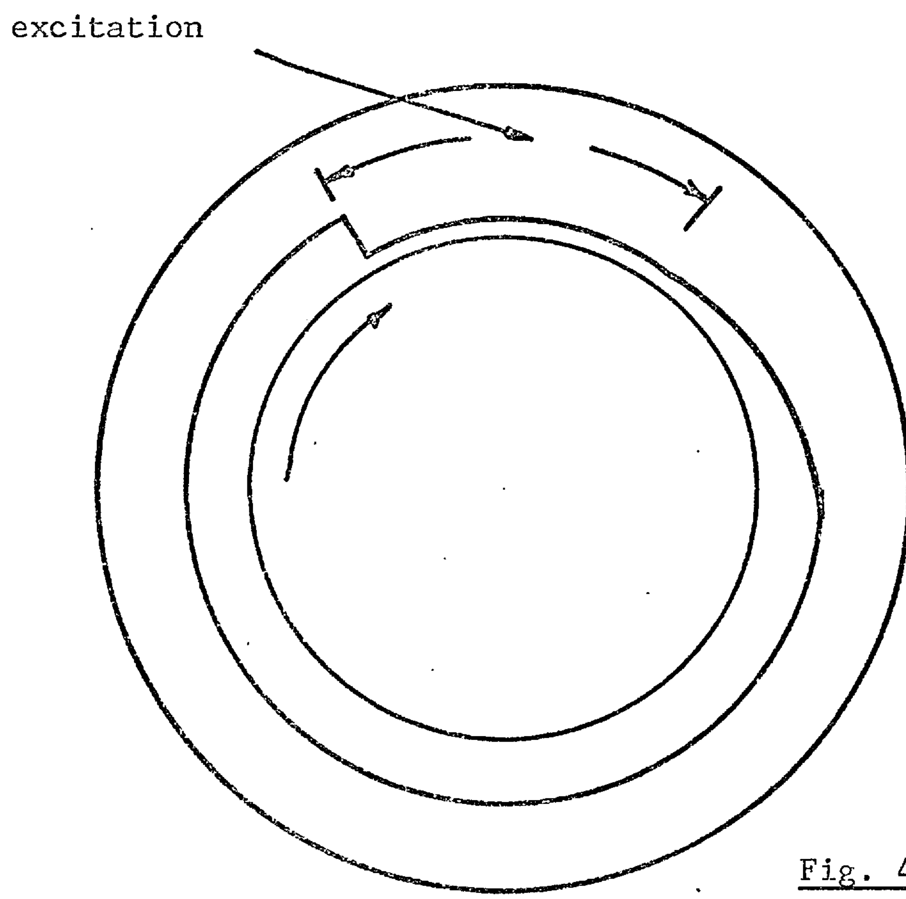

Fig. 4.2

Fig. 4.1 Stepped-gap machine

Fig. 4.2 Gap shaping outside the excited region harmonics of orders $n - m$ and $n + m$ when operating on the m^{th} permeance wave. Thus to find the n^{th} harmonic of flux in the air-gap it is necessary to add the component due to the n^{th} excitation harmonic acting on the average gap to those produced by the $(n \mp m)^{th}$ excitation harmonics acting on the m^{th} permeance wave.

The total open circuit flux on a particular harmonic may then be used to find a first component of the rotor induced e.m.f. This could be thought of as being due to a surface mutual inductance between the stator and the rotor.

Further components of rotor e.m.f.'s may be found by considering the induced rotor current sheet harmonics. The rotor current sheets act on the air-gap in the same manner as the stator sheets. Thus rotor e.m.f.'s, as far as the n^{th} harmonic field is concerned, are produced by the n^{th} and the $(n \pm m)^{th}$ rotor current sheets. These e.m.f.'s can be thought of as being due to a rotor surface self inductance. An additional rotor induced e.m.f. is produced by the rotor leakage field. This may be accounted for by including a rotor surface leakage inductance.

The rotor induced e.m.f.'s together with the rotor ohmic drop may be formed into a single equation for the n^{th} harmonic. This equation will contain as the unknown quantities the rotor surface currents due to each of the harmonics considered.

Thus, n equations, one for each of the harmonic fields included, are available and these may be solved simultaneously to find the rotor surface current distributions.

These distributions may then be used to find the rotor copper losses and torque.

The method follows the general lines adopted by Altenbernd et al. [4.2] for the case of a single phase squirrel-cage motor, but differs in treatment in that surface current densities are considered rather than rotor mesh currents, and of course in that the excitation considered here is poly-phase.

4.2 The open circuit flux density

With the rotor conductor removed, the flux density for the n^{th} harmonic of excitation acting on the m^{th} harmonic of permeance (1/air-gap length) may be found from,

$$b_{1\,m,n} = \mu_o \underline{P}_m \int J_{1n}\ Rdx \qquad \ldots\ldots\ldots\ldots\ldots(4.1)$$

where J_{1n} is the $n^{\underline{th}}$ harmonic of the excitation

and, $\underline{P}_m$ is the general $m^{\underline{th}}$ harmonic of the permeance.

From Appendix (3.5.1) in the previous chapter,

$$J_{1n} = \hat{J}_{1n} \operatorname{Sin}(\omega t - nx_1) \qquad \ldots\ldots\ldots\ldots\ldots(4.2)$$

where $\hat{J}_{1n} = A_{1n}\ \hat{J}_s$ $\qquad \ldots\ldots\ldots\ldots\ldots(4.3)$

$$A_{1n} = \frac{q}{k_p} \quad \frac{\operatorname{Sin} \alpha_n}{\alpha_n} \qquad \ldots\ldots\ldots\ldots\ldots(4.4)$$

and $\quad \alpha_n = (n - k_p) \frac{q}{k_p} \pi$ $\qquad \ldots\ldots\ldots\ldots\ldots(4.5)$

The permeance variations may be represented, in general, as,

$$\underline{P} = \lambda_o + \sum_{m=1}^{\infty} \lambda_m \operatorname{Cos}(mx_1 - \gamma_m) \quad \ldots\ldots\ldots(4.6)$$

That is, in equation (4.1),

$$\underline{P}_m = \lambda_m \quad \operatorname{Cos}(mx_1 - \gamma_m) \quad (m \neq 0) \ \ldots\ldots\ldots\ldots\ldots(4.7)$$

$$\underline{P}_m = \lambda_o = \text{average permeance } (m=0) \quad \ldots\ldots\ldots(4.8)$$

Defining $M_{1n} = \int J_{1n}\, R dx$ ....(4.9)

we have, from equations (4.2) and (4.3),

$$M_{1n} = \hat{M}_{1n} \operatorname{Cos}(\omega t - nx_1) \quad \text{.........................(4.10)}$$

where $\hat{M}_{1n} = \frac{R}{n} A_{1n} \hat{J}_s$ ....(4.11)

Now, from equations (4.1), (4.9) and (4.10),

$$b_{1m,n} = \mu_o \underline{P}_m M_{1n} \quad \text{........................(4.12)}$$

The total open-circuit flux density may be given as,

$$b_1 = \mu_o \left[\sum_n \hat{M}_{1n} \operatorname{Cos}(\omega t - nx_1) \right] \left[\lambda_o \left[1 + \sum_m 2K_m \operatorname{Cos}(mx_1 - \gamma_m) \right] \right]$$

........................(4.13)

where $K_m = \frac{\lambda_m}{2\lambda_o}$ ....(4.14)

$n = \mp 1, \mp 2, \mp 3$ .....

and $m = 1, 2, 3$ .....

Equation (4.13) could be re-written as,

$$b_1 = \mu_o \lambda_o \sum_n \hat{M}_{1n} \operatorname{Cos}(\omega t - nx_1)$$

$$+ \mu_o \lambda_o \sum_n \sum_m \hat{M}_{1n} K_m \operatorname{Cos}\left[\omega t - (n + m)x_1 + \gamma_m\right]$$

$$+ \mu_o \lambda_o \sum_n \sum_m \hat{M}_{1n} K_m \operatorname{Cos}\left[\omega t - (n - m)x_1 - \gamma_m\right]$$

$$\qquad \ldots\ldots\ldots\ldots\ldots(4.15)$$

which may be written as,

$$b_1 = \sum_n b_1(n,n) + \sum_n \sum_m b_1((n + m),n)$$

$$+ \sum_n \sum_m b_1(\,(n - m),n) \qquad \ldots\ldots\ldots\ldots\ldots(4.16)$$

where $\quad b_1(n,n) = \mu_o \lambda_o \hat{M}_{1n} \operatorname{Cos}(\omega t - nx_1) \ldots\ldots\ldots(4.17)$

$\qquad b_1((n+m),n) = \mu_o \lambda_o \hat{M}_{1n} \operatorname{Cos}(\omega t - (n+m)x_1 + \gamma_m) \ldots\ldots(4.18)$

and $\quad b_1((n-m),n) = \mu_o \lambda_o \hat{M}_{1n} \operatorname{Cos}(\omega t - (n-m)x_1 - \gamma_m) \ldots\ldots(4.19)$

Expression (4.17) represents a field of order n, due to the stator current sheet $n^{\underline{th}}$ harmonic acting on the average air-gap permeance λ_o, while expressions (4.18) and (4.19) represent the side-band fields of order (n + m) and (n - m) respectively which are due to the $n^{\underline{th}}$ harmonic of the current sheet acting on the $m^{\underline{th}}$ harmonic of the permeance wave. This means that the permeance wave exercises a modulation effect on the field.

Equation (4.15) can be represented by a single expression, as follows,

$$b_1 = \mu_o \lambda_o \sum_n \sum_m \hat{M}_{1n} K_m \operatorname{Cos}\left[\omega t - (n + m)x_1 + \gamma_m\right] \quad \ldots(4.20)$$

where $n = \mp 1, \mp 2, \mp 3 \ldots\ldots$

$m = 0, \mp 1, \mp 2, \mp 3 \ldots\ldots$

at $m = 0$, $K_m = 1$ and $\gamma_m = 0$, and for negative values of m, γ_m is replaced by $-\gamma_m$.

If the first n excitation harmonics are considered, it is apparent that field harmonics will be produced outside this range because of the "side-band" effects. In the analysis, these harmonic fields will be neglected. That is, the value of $(n \mp m)$ must be in the range of the considered excitation harmonics.

4.3 Surface mutual inductance "stator to rotor"

The field in the air-gap of the order n can be produced in one of two ways:-

a) An excitation of the order n acting on the average air gap permeance λ_o.

(b) An excitation of the order $n \mp m$ acting on the m^{th} permeance harmonic.

4.3.1 <u>The n^{th} harmonic field due to the n^{th} excitation harmonic</u>

This field may be written using equation (4.17) in rotor co-ordinates as,

$$b_1(n,n) = \mu_o \lambda_o \hat{M}_{1n} \operatorname{Cos}(S_n \omega t - n x_2) \quad \ldots\ldots\ldots\ldots(4.21)$$

This field causes an induced e.m.f. in the rotor, given by,

$$e_{1(n,n)} = S_n V_{sn} b_1(n,n)$$

Now the synchronous speed for the n^{th} harmonic is,

$$V_{sn} = \frac{R}{n}\omega \quad \ldots\ldots\ldots\ldots\ldots\ldots\ldots(4.22)$$

and from equation (4.11)

$$\hat{M}_{1n} = \frac{R}{n} A_{1n} \hat{J}_s$$

Therefore,

$$e_{1(n,n)} = S_n \omega \frac{R}{n} \mu_o \lambda_o \frac{R}{n} A_{1n} \hat{J}_s \cos(S_n \omega t - nx_2)$$

This could be written in complex notation, using J_{1n} as a phase reference,

$$E_{1(n,n)} - -jS_n \omega M_{21n} \hat{J}_s \qquad \text{.........................(4.23)}$$

where,

$$M_{21n} = \mu_o \lambda_o \left(\frac{R}{n} \right)^2 A_{1n} \qquad \text{.........................(4.24)}$$

This quantity can be regarded as a surface mutual inductance.

4.3.2 The $n^{\underline{th}}$ harmonic field due to the $(n \mp m)^{\underline{th}}$ excitation harmonic

This field may be written, using equations (4.18) and (4.19), in rotor co-ordinates as,

$$b_1(n,n+m) = \mu_o \lambda_o \hat{M}_{1\ (n+m)} K_m \operatorname{Cos}(S_n \omega t - nx_2 - \gamma_m) \quad \text{...(4.25)}$$

where $m = \mp 1, \mp 2$ .....

and for negative values of m, γ_m is replaced by $-\gamma_m$.

This field causes an induced e.m.f. in the rotor, given by,

$$e_{1(n,n+m)} = S_n V_{sn} b_{1(n,n+m)}$$

$$= S_n \omega \frac{R}{n} \mu_o \lambda_o \frac{RK_m}{(n+m)} A_{1(n+m)} \hat{J}_s \cos(S_n \omega t - nx_2 - \gamma_m) \quad \text{...............(4.26)}$$

Writing this, as before, in complex notation,

$$E_{1(n,n+m)} = -jS_n \omega M_{21(n+m)} \hat{J}_s \quad \text{...............(4.27)}$$

where,

$$M_{21(n+m)} = \mu_o \lambda_o \frac{R^2}{n(n+m)} \cdot A_{1(n+m)} K_m \cdot \exp(-j\gamma_m) \text{...(4.28)}$$

The total surface mutual inductance may be written using equations (4.24) and (4.28) as,

$$M_{21} = \mu_o \lambda_o \frac{R^2}{n} \sum_m \frac{A_{1(n+m)}}{(n+m)} K_m \exp(-j\gamma_m) \quad \text{.....(4.29)}$$

where $n = \mp 1, \mp 2$ .....

$m = 0, \mp 1, \mp 2, \mp 3$ .....

and when $m = 0$, $K_m = 1$ and $\gamma_m = 0$.

Again when m assumes negative values, γ_m is replaced by $-\gamma_m$.

4.4 Rotor surface self inductance

The rotor surface current density J_r may be represented as,

$$J_r = \sum_n J_{2n} \operatorname{Sin}(S_n \omega t - nx_2 - \theta_{2n}) \qquad \ldots\ldots\ldots\ldots(4.30)$$

where θ_{2n} is the phase of the n^{th} rotor current density harmonic relative to J_{1n}.

The field due to this current may be considered,as in the previous section, in two parts.

4.4.1 The n^{th} harmonic field due to the n^{th} rotor current harmonic

This field may be written, using equation (4.21), as,

$$b_{2(n,n)} = \mu_o \lambda_o \hat{M}_{2n} \operatorname{Cos}(S_n \omega t - nx_2 - \theta_{2n}) \qquad \ldots\ldots(4.31)$$

where $\quad M_{2n} = \int J_{2n} \, Rdx$

$$= \frac{R}{n} \hat{J}_{2n} \operatorname{Cos}(S_n \omega t - nx_2 - \theta_{2n}) \qquad \ldots\ldots\ldots(4.32)$$

that is, $\quad \hat{M}_{2n} = \frac{R}{n} \hat{J}_{2n} \qquad \ldots\ldots\ldots\ldots\ldots\ldots\ldots\ldots(4.33)$

The self induced e.m.f. due to this field may be written as,

$$e_{2(n,n)} = S_n V_{sn} b_{2(n,n)}$$

Substituting for V_{sn} from equation (4.22), and $b_{2(n,n)}$ from equations (4.31) and (4.33),

$$e_{2(n,n)} = S_n \frac{R}{n}\omega\mu_o\lambda_o \frac{R}{n} \hat{J}_{2n} \, \text{Cos}(S_n\omega t - nx_2 - \theta_{2n}) \text{.....} (4.34)$$

Writing this in complex notation, and keeping J_{1n} as a phase reference,

$$E_{2(n,n)} = -jS_n\omega L_{22n} \hat{J}_{2n} \exp(j\theta_{2n}) \text{ ....} (4.35)$$

where $$L_{22n} = \frac{R^2}{n^2} \cdot \mu_o\lambda_o \text{ ....} (4.36)$$

Further induced e.m.f. may be produced by the leakage inductance of the rotor sheet, given by,

$$E_{2gn} = -jS_n\omega L_{2gn} \hat{J}_{2n} \exp(j\theta_{2n}) \text{ ....} (4.37)$$

Where L_{2gn} is the surface leakage inductance of the rotor.

The resistive drop in the rotor may also be represented as,

$$E_{2rn} = \rho_{2n} \hat{J}_{2n} \exp(j\theta_{2n}) \quad \text{......................(4.38)}$$

where ρ_{2n} is the surface resistivity of the rotor.

4.4.2 The n^{th} harmonic field due to the $(n \mp m)^{th}$ rotor current harmonic

Again, this field may be expressed as follows,

$$b_{2(n,n+m)} = \mu_o \lambda_o \hat{M}_{2(n+m)} K_m \, \mathrm{Cos}\left[S_n \omega t - nx_2 - \theta_{2(n+m)} - \gamma_m \right]$$
$$\text{....................(4.39)}$$

where $m = \mp 1, \mp 2$ .....

and the induced e.m.f. due to this field is,

$$e_{2(n,n+m)} = S_n V_{sn} \, b_{2(n,n+m)}$$

$$= S_n \frac{R}{n} \omega \, \mu_o \lambda_o \frac{R}{(n+m)} J_{2(n+m)}$$

$$K_m \, \mathrm{Cos}\left[S_n \omega t - nx_2 - \theta_{2(n+m)} - \gamma_m \right]$$
$$\text{...............(4.40)}$$

and in complex notation this becomes,

$$E_{2(n,n+m)} = -jS_n\omega L_{22(n+m)} \hat{J}_{2(n+m)} \exp \left[j\theta_{2(n+m)}\right] \text{.......}(4.41)$$

where $$L_{22(n+m)} = \frac{R^2}{n(n+m)} \mu_o \lambda_o . K_m \exp(-j\gamma_m) \text{...........}(4.42)$$

4.5 The rotor voltage equation

From equations (4.29), (4.36), (4.37), (4.38) and (4.42),

$$0 = (\rho_{2n} + jS_n\omega L_{2gn}) \hat{J}_{2n} \exp(j\theta_{2n})$$

$$+ jS_n\omega L'_{2n} \sum_m \frac{K_m}{(n+m)} \hat{J}_{2(n+m)} \exp\left[j\theta_{2(n+m)}\right] \exp(-j\gamma_m)$$

$$+ jS_n\omega M'_{21n} \sum_m \frac{A_{1(n+m)}}{(n+m)} K_m \hat{J}_s \exp(-j\gamma_m) \text{........}(4.43)$$

where $L'_{2n} = M'_{21n} = \mu_o \lambda_o \frac{R^2}{n}$

$n = \mp 1, \mp 2 \text{.....}$

$m = 0, \mp 1, \mp 2 \text{.....}$

when $m = 0$, $K_m = 1$ and $\gamma_m = 0$,

and when m is negative, γ_m is replaced by $-\gamma_m$.

Now, writing,

$$\sum_m \frac{A_{1(n+m)}}{(n+m)} K_m \exp(-j\gamma_m) = F_{21n} \quad (m=0,\mp 1,\mp 2 \text{ ...}) \text{ ....}(4.44)$$

$$\frac{K_m^*}{(n+m)} \exp(-j\,\gamma_m) = F_{2(n+m)} \qquad (m=\mp 1, \mp 2 \ldots) \qquad \ldots\ldots\ldots (4.45)$$

and $$L_{2n} = \frac{L'_{2n}}{n} + L_{2gn} \qquad \ldots\ldots\ldots (4.46)$$

Equation (4.43) may now be set in matrix form as shown in Fig. (4.3).

This figure is drawn for a restricted harmonic range with n up to 3 and using the first 3 permeance harmonics. It will, of course, be appreciated that this matrix could be extended to include any desirable number of harmonics.

For an appreciable number of harmonics a computer solution of the matrix is essential. This solution can conveniently be found by first inverting the impedance matrix to form an admittance matrix, whence the rotor currents can be found by multiplying the admittance matrix by a voltage matrix.

Once the rotor currents are known, the output torque may be calculated as shown in the following section.

4.6 Performance calculations

4.6.1 The output torque calculations

The rotor ohmic loss $= \frac{A_r}{2} \sum \rho_{2n} J_{2n}^2$ watts

where A_r = rotor surface area.

$$
\left[\begin{array}{ccccccc}
1 & 0 & 0 & 0 & 0 & 0 & 0 \\
\begin{array}{c} jS_{-3}\omega M'_{21(-3)} \\ F_{21(-3)} \end{array} & \begin{array}{c} \rho_{2(-3)} + \\ jS_{-3}\omega L_{2(-3)} \end{array} & \begin{array}{c} jS_{-3}\omega L'_{2(-3)} \\ F_{2(-2)} \end{array} & \begin{array}{c} jS_{-3}\omega L'_{2(-3)} \\ F_{2(-1)} \end{array} & 0 & 0 & 0 \\
\begin{array}{c} jS_{-2}\omega M'_{21(-2)} \\ F_{21(-2)} \end{array} & \begin{array}{c} jS_{-2}\omega L'_{2(-1)} \\ F_{2(-3)} \end{array} & \begin{array}{c} \rho_{2(-2)} + \\ jS_{-2}\omega L_{2(-2)} \end{array} & \begin{array}{c} jS_{-2}\omega L'_{2(-2)} \\ F_{2(-1)} \end{array} & \begin{array}{c} jS_{-2}\omega L'_{2(-2)} \\ F_{2(1)} \end{array} & 0 & 0 \\
\begin{array}{c} jS_{-1}\omega M'_{21(-1)} \\ F_{21(-1)} \end{array} & \begin{array}{c} jS_{-1}\omega L'_{2(-1)} \\ F_{2(-3)} \end{array} & \begin{array}{c} jS_{-1}\omega L'_{2(-1)} \\ F_{2(-2)} \end{array} & \begin{array}{c} \rho_{2(-1)} + \\ jS_{-1}\omega L_{2(-1)} \end{array} & \begin{array}{c} jS_{-1}\omega L'_{2(-1)} \\ F_{2(1)} \end{array} & \begin{array}{c} jS_{-1}\omega L'_{2(-1)} \\ F_{2(2)} \end{array} & 0 \\
\begin{array}{c} jS_{1}\omega M'_{21(1)} \\ F_{21(1)} \end{array} & 0 & \begin{array}{c} jS_{1}\omega L'_{2(1)} \\ F_{2(-2)} \end{array} & \begin{array}{c} jS_{1}\omega L'_{2(1)} \\ F_{2(-1)} \end{array} & \begin{array}{c} \rho_{2(1)} + \\ jS_{1}\omega L_{2(1)} \end{array} & \begin{array}{c} jS_{1}\omega L'_{2(1)} \\ F_{2(2)} \end{array} & \begin{array}{c} jS_{1}\omega L'_{2(1)} \\ F_{2(3)} \end{array} \\
\begin{array}{c} jS_{2}\omega M'_{21(2)} \\ F_{21(2)} \end{array} & 0 & 0 & \begin{array}{c} jS_{2}\omega L'_{2(2)} \\ F_{2(-1)} \end{array} & \begin{array}{c} jS_{2}\omega L'_{2(2)} \\ F_{2(1)} \end{array} & \begin{array}{c} \rho_{2(2)} + \\ jS_{2}\omega L_{2(2)} \end{array} & \begin{array}{c} jS_{2}\omega L'_{2(2)} \\ F_{2(3)} \end{array} \\
\begin{array}{c} jS_{3}\omega M'_{21(3)} \\ F_{21(3)} \end{array} & 0 & 0 & 0 & \begin{array}{c} jS_{3}\omega L'_{2(3)} \\ F_{2(1)} \end{array} & \begin{array}{c} jS_{3}\omega L'_{2(3)} \\ F_{2(2)} \end{array} & \begin{array}{c} \rho_{2(3)} + \\ jS_{3}\omega L'_{2(3)} \end{array}
\end{array}\right]
\left[\begin{array}{c}
\hat{J}_S \\ J_{2(-3)} \\ J_{2(-2)} \\ J_{2(-1)} \\ J_{2(1)} \\ J_{2(2)} \\ J_{2(3)}
\end{array}\right]
=
\left[\begin{array}{c}
\hat{J}_S \\ 0 \\ 0 \\ 0 \\ 0 \\ 0 \\ 0
\end{array}\right]
$$

Fig. 4.3 The matrix for finding the rotor current components

The synchronous power input $= \frac{A_r}{2} \sum_n \frac{\rho_{2n} \hat{J}_{2n}^2}{S_n}$ watts

and the output torque $= \frac{RA_r}{2} \sum_n \frac{\rho_{2n} \hat{J}_{2n}^2}{S_n V_{sn}}$ N-m ....(4.47)

4.6.2 The flux density profile calculations

To calculate the total flux density in the air-gap, equation (4.20) may be used, after replacing $\hat{M}_{1n}$ by,

$$M_n = \hat{M}_{1n} + \hat{M}_{2n}$$

$$= \frac{R}{n} \left[A_{1n} \hat{J}_s + \hat{J}_{2n} \exp(j\theta_{2n}) \right] \quad \text{....................(4.48)}$$

The equation for the flux density in stator co-ordinates is then,

$$b_g = \mu_o \lambda_o \sum_n \sum_m M_n K_m \text{ Cos } \left[\omega t - (n + m)x_1 + \gamma_m \right] \quad \text{...(4.49)}$$

$n = \mp 1, \mp 2$ .....

$m = 0, \mp 1, \mp 2$ .....

when $m = 0$, $K_m = 1$ and $\gamma_m = 0$,

and when m is negative, γ_m is replaced by $-\gamma_m$.

4.6.3 Voltage calculations

If the complex $n^{\underline{th}}$ harmonic of the air-gap flux density is denoted by B_{gn}, then the rotor voltage equation may be rewritten as,

$$(\rho_{2n} + jS_n \omega L_{2gn})\hat{J}_{2n} \exp(j\theta_{2n}) + S_n V_{Sn} B_{gn} = 0$$

or

$$B_{gn} = -\frac{1}{S_n V_{Sn}} \left[\rho_{2n} + jS_n \omega L_{2gn}\right] \hat{J}_{2n} \exp(j\theta_{2n})$$

The input power may then be given as,

$$P_T = A_S \sum_n \frac{1}{2} V_{Sn} \hat{J}_{1n} \mathcal{R}(B_{gn})$$

where A_S is the stator surface area.

Similarly, the reactive power input is given as,

$$Q_T = A_S \sum_n \frac{1}{2} V_{Sn} \hat{J}_{1n} \mathcal{J}(B_{gn})$$

Following the method given in section (3.3.3) these power inputs may be used together with the stator resistance and leakage reactance to find the input voltage.

4.7 Comparison of the permeance harmonic analysis with the simple excitation harmonic analysis

It is apparent that the permeance analysis should reduce to the earlier simple harmonic analysis when the case of a uniform air-gap is considered. In this case the permeance harmonic series reduces to a single term corresponding to the reciprocal of the air-gap length.

The equation for air-gap flux density (4.49) then becomes (by putting m = 0, i.e. $K_m = 1$ and $\gamma_m = 0$),

$$b_g = \frac{\mu_o}{g} \sum_n \frac{R}{n} \left[A_{1n}\hat{J}_s + \hat{J}_{2n} \exp(j\theta_{2n}) \right] \operatorname{Cos} \left[\omega t - nx_1 \right] \qquad \text{..........(4.50)}$$

Now, from equation (4.22),

$$\frac{R}{n} = \frac{V_{sn}}{\omega} = \frac{P_n}{\pi} \qquad \text{..............................(4.51)}$$

and from equation (4.3),

$$J_{1n} = A_{1n}\hat{J}_s \qquad \text{..............................(4.52)}$$

Substituting for $\frac{R}{n}$ and $\hat{J}_s$ from equations (4.51) and (4.52) respectively into (4.50) and writing the equation for a particular harmonic number,

$$b_{gn} = \frac{\mu_o P_n}{g\pi} (\hat{J}_{1n} + \hat{J}_{2n} \exp(j\theta_{2n})) \text{Cos}(\omega t - nx_1) \quad \ldots\ldots\ldots (4.53)$$

Writing this in complex notation,

$$b_{gn} = j \frac{\mu_o}{g} \frac{P_n}{\pi} (J_{1n} + J_{2n}) \quad \ldots\ldots\ldots\ldots\ldots\ldots\ldots\ldots\ldots (4.54)$$

Now, from equation (3.3),

$$b_g = \frac{j \mu_o}{g} \frac{P_\omega}{\pi} (J_s + J_R) \quad \ldots\ldots\ldots\ldots\ldots\ldots \ldots\ldots (4.55)$$

It will be observed that for a single harmonic, equation (4.54) corresponds exactly with equation (4.55). This means that the two analyses are the same for the uniform air-gap case.

4.8 Application of the theory to an arc-stator machine

The above permeance analysis allows the use of any gap variation. In order to apply the method to an arc-stator machine, a model with a symetrical air-gap variation may be considered as a first approximation. This model is shown on Fig. (4.1). If it is assumed that the outside gap is g_o, then Appendix (4.11) shows that the harmonic series is given as,

$$\underline{P} = \lambda_o + \sum_{m=1}^{\infty} \lambda_m \operatorname{Cos}(mx_1) \quad \ldots\ldots\ldots\ldots\ldots\ldots\ldots\ldots(4.56)$$

where $$\lambda_o = \frac{1}{\beta\, g_i}\left[(\beta - 1)\frac{q}{k_p} + 1\right] \quad \ldots\ldots\ldots\ldots\ldots\ldots\ldots(4.57)$$

$$\lambda_m = \frac{2}{\beta\pi\, mg_i}\left[(\beta - 1)\operatorname{Sin}\left(\frac{mq\pi}{k_p}\right)\right] \ldots\ldots\ldots\ldots\ldots(4.58)$$

and $$\beta = \frac{g_o}{g_i} \quad \ldots\ldots\ldots\ldots\ldots\ldots\ldots\ldots\ldots\ldots(4.59)$$

If this series is compared with the general form given in equation (4.6), it is apparent that $\gamma_m = 0$ for the symetrical gap case.

Following the discussion in the previous chapter, the gap outside g_o appropriate to the arc-stator case can be taken as P_w/π .

In order that the present analysis may be compared with the earlier analysis (Section (3.3.6)), an equivalent set of results for the torque were computed. The results are shown on Fig. (4.4). It will be observed that the agreement is generally good and it now remains to verify the permeance harmonic results experimentally.

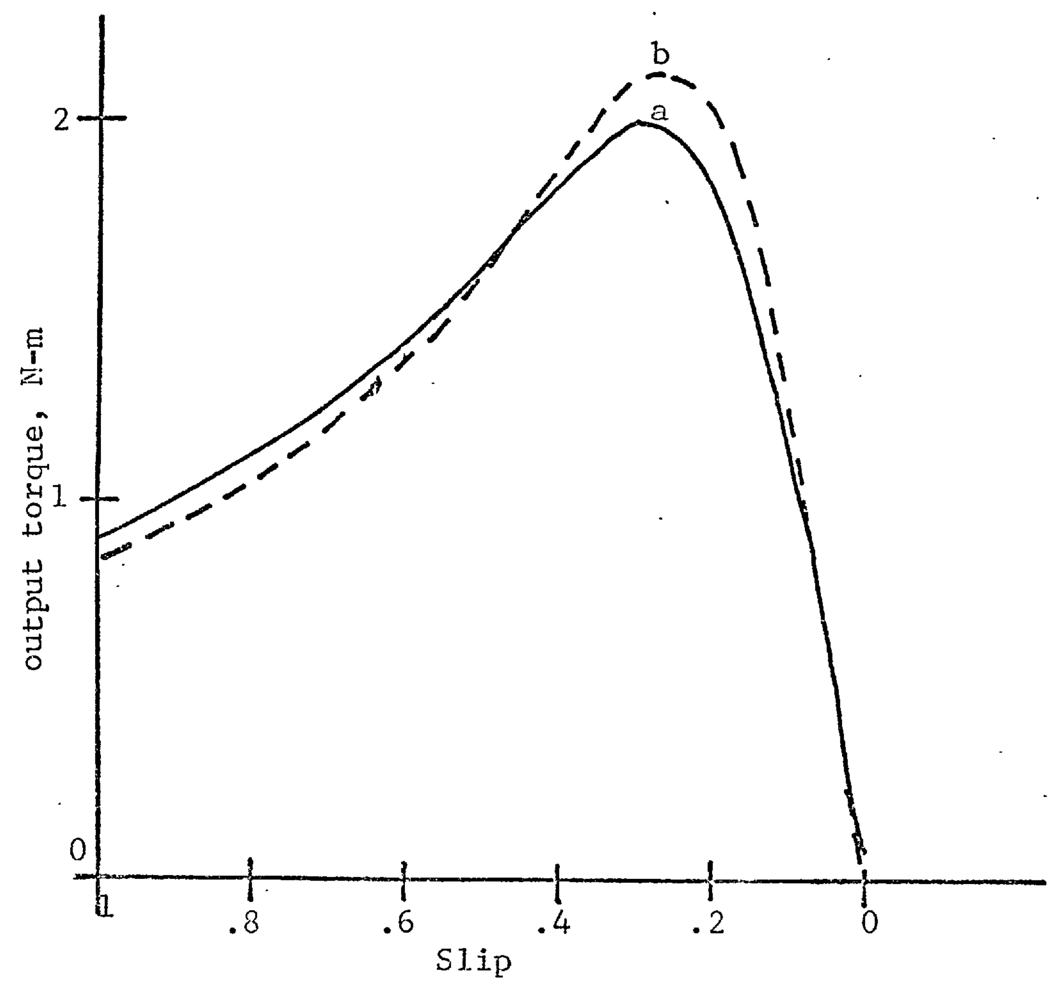

Fig. 4.4 Theoretical torque-slip curves

(a) Permeance method
(b) Simple harmonic method with allowance for exit-edge losses

4.9 Comparison of the experimental results with the permeance harmonic theory

4.9.1 Torque measurements

Experimental torque-slip and voltage-slip curves for the arc-stator machine are given in Fig. (3.16). These curves are repeated on Fig. (4.5) together with the predicted values using the permeance harmonic analysis. It will be observed that the agreement is better than that obtained in the previous chapter, as far as the torque is concerned.

4.9.2 Flux measurement

Measurements were taken to find the flux profile in the same manner as that described in Section (3.3.2). The search coils used were positioned in the air-gap under the excited region at intervals of $\frac{2P_w}{3}$ and also at the same spacing, in positions about an air-gap length from the rotor, outside the stator arc. Fig. (4.6) compares the practical and theoretical values. It will be noted that the agreement is acceptable.

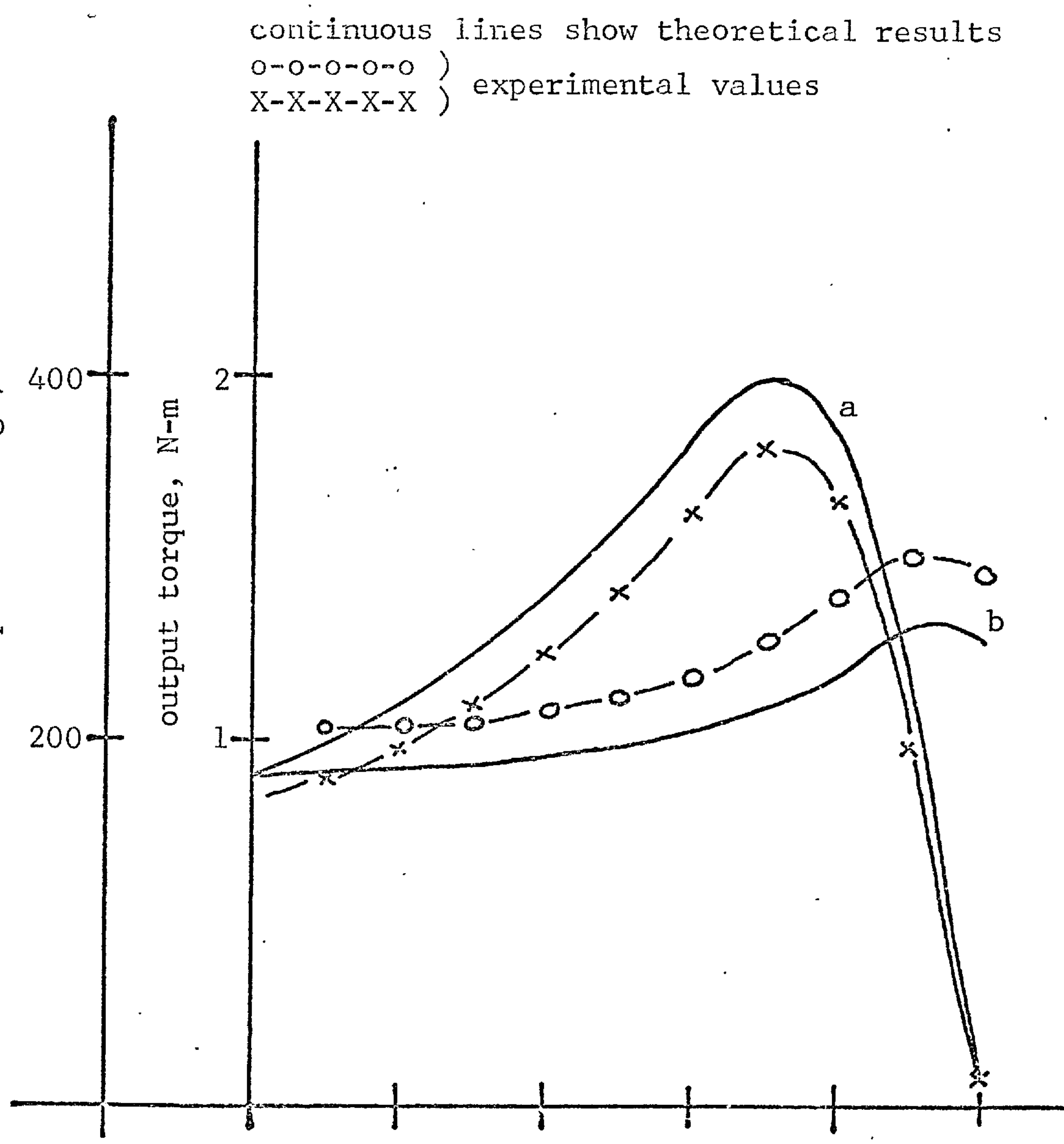

Fig. 4.5 Comparison between predicted results using the permeance harmonic method and experimental values

(a) torque
(b) voltage

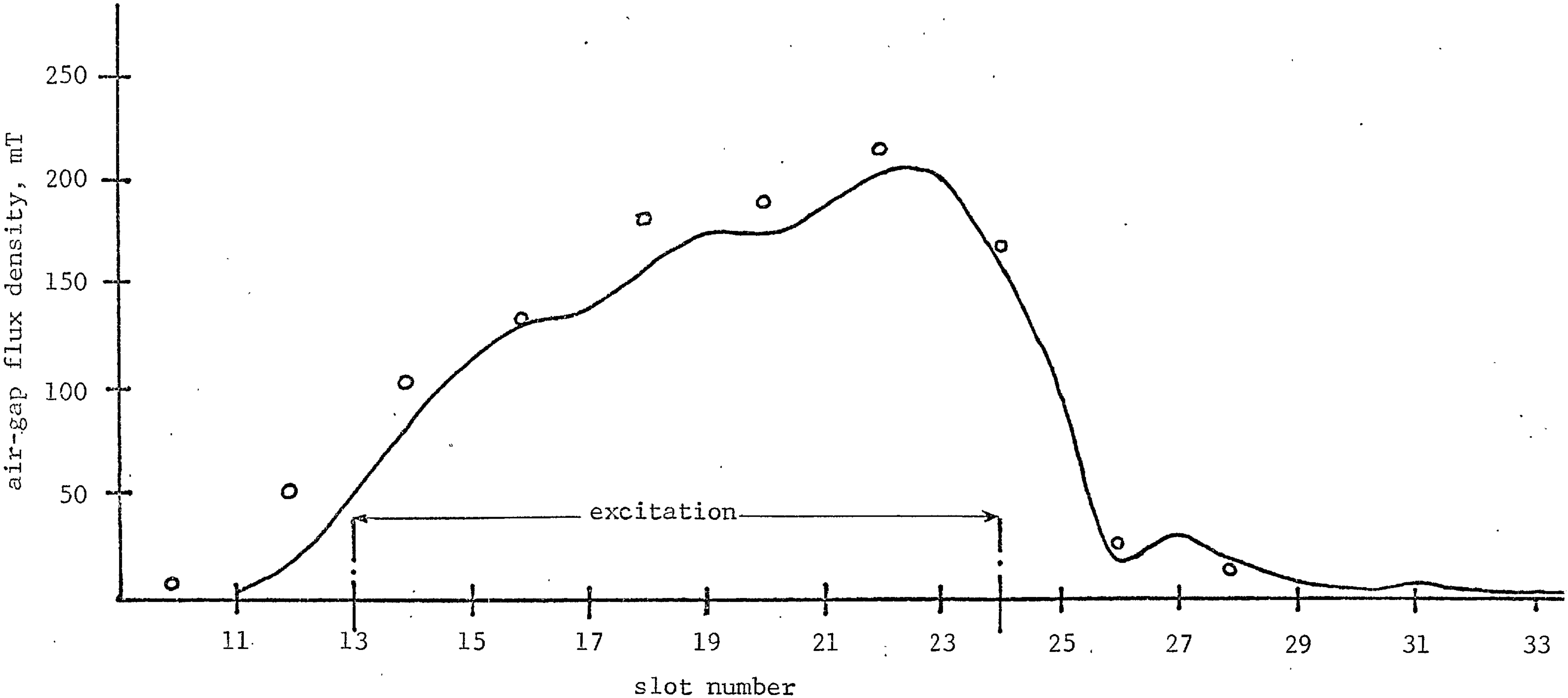

Fig. 4.6 Flux profile for the arc stator machine. Measured values shown by points. Calculated values, using the permeance harmonic analysis, by the line.

4.10 Conclusions

Despite the assumptions made in formulating the theory, the experimental and theoretical results show remarkable agreement. This more rigorous method has confirmed theoretically the value of the earlier more simple analysis.

It must be emphasised again that whilst the longitudinal end effects have been considered more rigorously, the analysis is still strictly "one-dimensional" and neglects transverse edge effects. Plate-secondary machines can be analysed by this technique only if the rotor surface resistivity and leakage inductance are known.

Clearly a two-dimensional approach is necessary either as a complete analysis or as a method of finding the surface impedances for a particular harmonic excitation mode.

A suitable form of analysis is attempted in the next chapter.

4.11 Appendix

Fourier Analysis of the permeance wave

for the symetrical air-gap case

The permeance (1/air-gap length) variation for this case is shown in Fig. (4.7). It can be seen from the figure that the function is even about the chosen axis, and therefore the harmonic components will include no sine terms, and the permeance may be represented as,

$$\underline{P} = \frac{a_o}{2} + \sum_{1}^{\infty} a_n \operatorname{Cos}(mx) \qquad \text{....................(4.60)}$$

where
$$a_n = \frac{2}{\pi}\left[\int_{o}^{\frac{q\pi}{k_p}} \lambda \operatorname{Cos}(mx)dx + \frac{1}{\beta} \int_{\frac{q\pi}{k_p}}^{\pi} \lambda \operatorname{Cos}(mx)dx)\right]$$

$$\lambda = \frac{1}{g_i} \qquad \text{...........................(4.61)}$$

and
$$\beta = \frac{g_o}{g_i} \qquad \text{...........................(4.62)}$$

After performing the integration,

$$a_n = \frac{2\lambda}{\beta\pi m}\left[(\beta - 1) \operatorname{Sin} \frac{mq\pi}{k_p}\right]$$

$$a_o = \frac{2}{\pi}\left[\int_{o}^{\frac{q\pi}{k_p}} \lambda\, dx + \frac{1}{\beta}\int_{\frac{q\pi}{k_p}}^{\pi} \lambda dx\right] = \frac{2\lambda}{\beta}\left[(\beta - 1)\frac{q}{k_p} + 1\right]$$

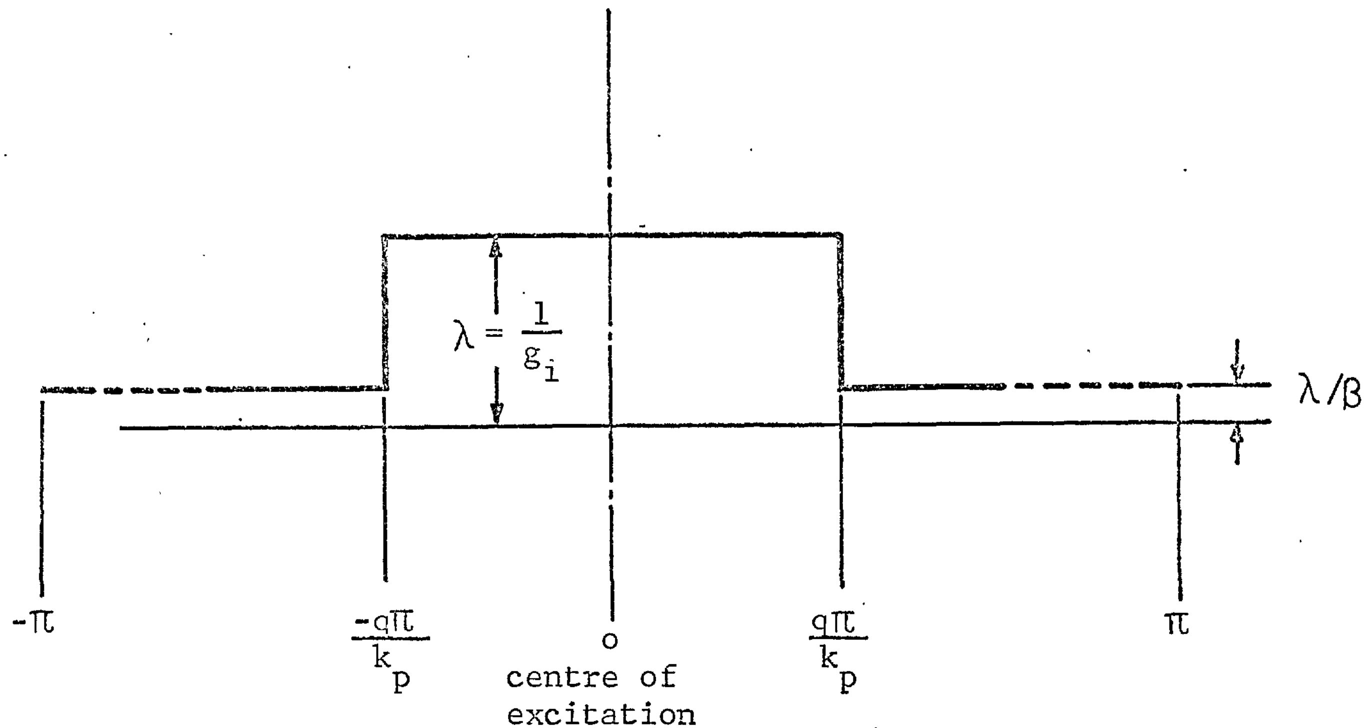

Fig. 4.7 Permeance variation for the symetrical case

Therefore,

$$\underline{P} = \lambda_o + \sum_{m=1}^{\infty} \lambda_m \operatorname{Cos}(mx) \qquad \ldots\ldots\ldots\ldots\ldots(4.63)$$

where

$$\lambda_o = \frac{1}{\beta g_i} \left[(\beta - 1) \frac{q}{K_p} + 1 \right] \ldots\ldots\ldots(4.64)$$

$$\lambda_m = \frac{2}{\beta \pi m g_i} (\beta - 1) \operatorname{Sin}\left(\frac{mq\pi}{K_p} \right) \ldots\ldots.(4.65)$$

CHAPTER FIVE

TWO-DIMENSIONAL ANALYSIS OF LINEAR INDUCTION MACHINES

5.1 Introduction

It has been previously pointed out that the effects of finite width secondary plate may be accounted for by ascribing effective values to the plate surface impedance. The Russell and Norsworthy paper [5.1] quoted in chapter 3 used a simple model and, assuming a thin rotor plate, calculated only the resistive part of the impedance. Other authors have also presented analyses with varying degrees of difficulty. Bolton [5.2] used a model which also had a thin sheet rotor and neglected field variations in the direction perpendicular to the plane of the rotor sheet. However, the analysis was performed on the basis of a current sheet excitation rather than the forced flux conditions assumed by Russell and Norsworthy. Thus longitudinal components of plate current were allowed to drive flux components in the stator iron. Therefore the effective plate surface impedance which could be derived from the paper [5.2] would include at least some rotor leakage reactance effect.

Preston and Reece[5.3] used an ingenious model and performed harmonic analysis in a direction transverse to the field travel. The development of the Preston and Reece model is illustrated in Fig. (5.1). Fig. (5.1a) shows a transverse section through a plate secondary linear motor. In order to use a harmonic analysis it was assumed that a large number of machines existed side by side with their excitations alternatively arranged positively and negatively. In order to make the problem tractable the authors assumed that the iron surfaces were planar and continuous. A transverse section through the resulting model is shown in Fig. (5.1b). The transverse variations of the excitation amplitude is shown in Fig. (5.1c). The lengths marked "2C" correspond to the width of the original stator core. The sections of excitation between these constant portions were intended to represent the excitation produced by the end-turns of the original windings. This excitation was assumed to form a current sheet on the surface of the stator iron as shown in Fig. (5.1b).

Veske [5.4] also considered a model which is similar to that of Preston and Reece with the exception that the excitation is assumed to have zero value outside the original stator core. This excitation is shown at Fig. (5.1d).

The use of a multi-layer approach to induction machine analysis was considered in a paper by Greig and Freeman [5.5].

(a) Transverse section through a plate secondary linear motor
(b) Transverse section through the electro-magnetic model
(c) Excitation amplitude variation for the Preston and Reece model
(d) Excitation amplitude variation for the Veske model

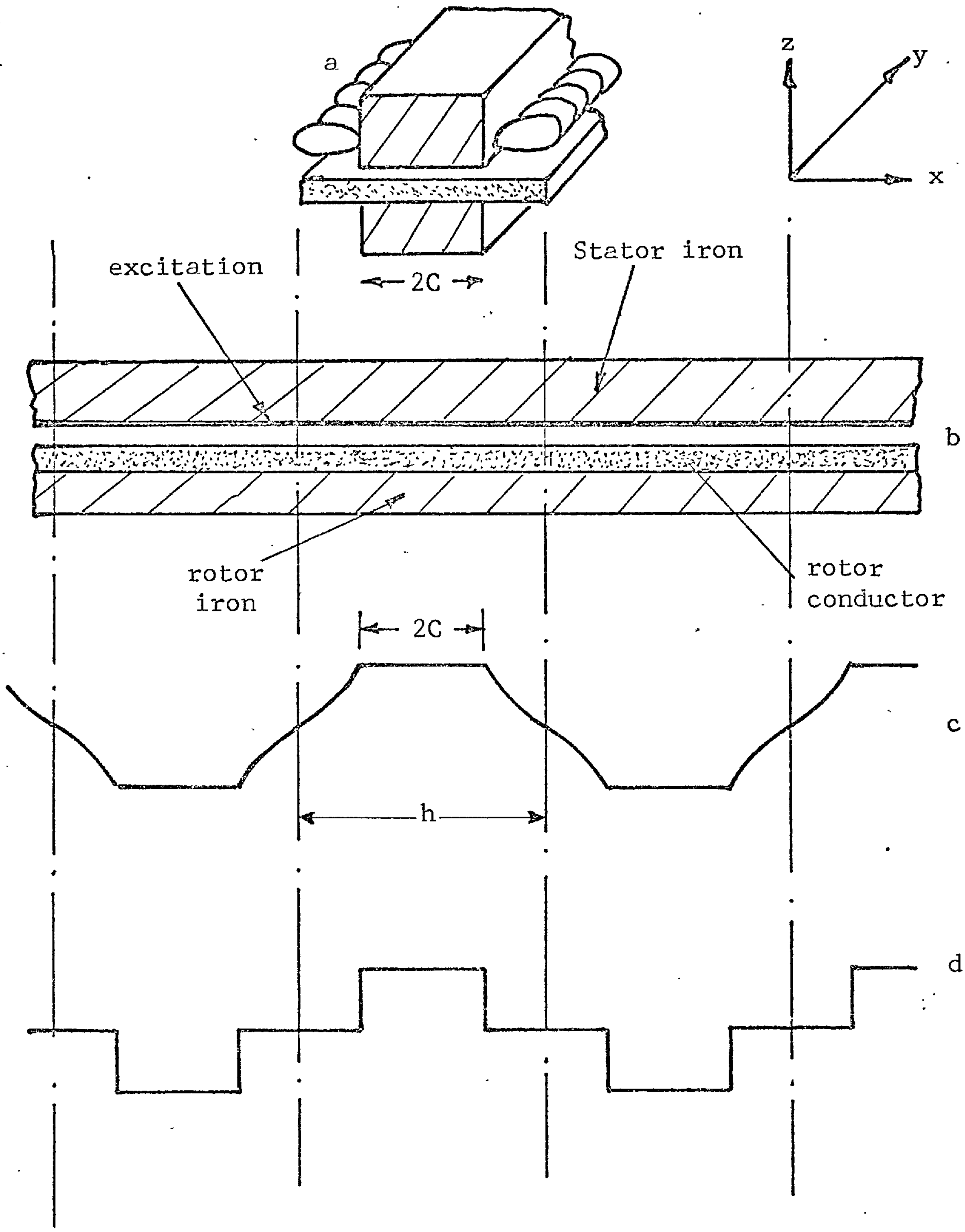

Fig. 5.1 Development of the Preston and Reece model

This first paper assumed a sinusoidal excitation and an infinitely wide model. This paper was followed by a paper by Freeman [5.6] which analysed the same model using a surface impedance approach. Freeman [5.7][5.8] has also used the surface impedance multi-layer technique to analyse the Preston and Reece model. This results in a large simplification compared with the original analysis.

All the above mentioned analyses ignore the longitudinal effects by assuming a sinusoidal excitation in this direction.

It is the object of this chapter to perform an analysis following Freeman as far as transverse effects are concerned, but including longitudinal effects by performing a second harmonic analysis in this direction. The treatment of the longitudinal harmonic follows the same lines as that in chapter 3 and allowance for the exit-edge loss is made in the same fashion.

5.2 The double harmonic analysis

The analysis performed in chapter 2 used harmonics in the transverse direction and also used the surface impedance multi-layer approach. However, this analysis was given in cylindrical coordinates. Thus, whilst the same broad steps are apparent in the treatment which follows, the detailed equations are different in that they are concerned with a planar model rather than tubular and in that harmonics in the longitudinal direction are considered.

5.2.1 The excitation harmonic series

The model considered in this section is the same as that used in Section (3.3.1), that is, a cylindrical machine with a constant air-gap and a short patch of excitation.

It will be assumed that in modelling a particular linear motor the radii are arranged to be very much greater than the layer thicknesses. This means that planar geometry can be assumed in forming the field equations. The axis labelling system is shown on Fig. (5.1a).

The current sheet is assumed to extend longitudinally over the range,

$$\frac{-q\pi}{k_p} \text{ to } \frac{q\pi}{k_p} \text{ radians.}$$

The harmonic analysis in the y direction is shown in Appendix (3.5.1).

The transverse harmonic series, was found by considering the excitation shown in Fig. (5.1c). However, in order to introduce more flexibility into the analysis the shape shown in detail in Fig. (5.2) was used. This has the advantage that the curved portions representing the end windings may be varied in length. The original Preston and Reece [(5.3)] model took the end winding representation to the edge of the plate. However, it is probably more appropriate to extend it only to the edge of the end winding.

The transverse harmonic series is found in Appendix (5.7.1).

The current density may be represented by,

$$J_x = \sum_n \sum_m J_{x,n,m} \operatorname{Cos}\left(\frac{m\pi x}{h}\right) \exp\left[j(\omega t - k_n y)\right] \quad \ldots.(5.1)$$

where, $J_{x,n,m} = A_{1n} C_{1m} J_S$

A_{1n} is the longitudinal harmonic coefficient, and C_{1m} is the transverse harmonic coefficient.

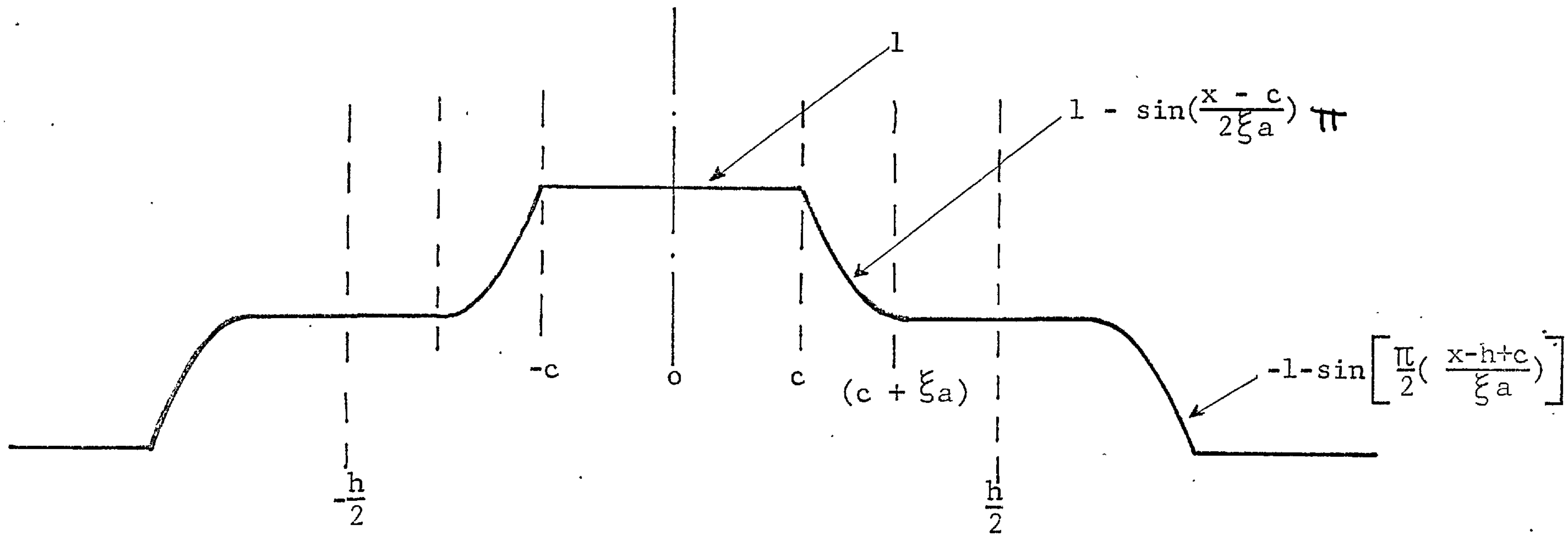

<u>Fig. 5.2</u> The excitation variation considered in the analysis

From Appendix (3.5.1) in chapter 3,

$$A_{1n} = \frac{q}{k_p} \frac{\sin\alpha_n}{\alpha_n}$$

$$\alpha_n = (n - k_p) \frac{q}{k_p}\pi$$

$$k_n = \frac{n\pi}{k_p P_w} \qquad \ldots\ldots\ldots\ldots\ldots\ldots\ldots\ldots\ldots(5.2)$$

and $\quad n = \mp 1, \mp 2, \mp 3 \ldots\ldots$

From Appendix (5.7.1),

$$C_{1m} = \frac{4}{\pi}\left[\frac{1}{m}\sin\left[\frac{m\pi}{h}(C + \xi a)\right] - (A_1 + A_2)\cos\left(\frac{m\pi c}{h}\right) + A_1\cos\left(\frac{\pi A_3}{2h}\right) + A_2\cos\left(\frac{\pi A_4}{2h}\right)\right]$$

where,

$$A_1 = \frac{\xi a}{h + 2m\xi a}$$

$$A_2 = \frac{\xi a}{h - 2m\xi a}$$

$$A_3 = h + 2m(C + \xi a)$$

$$A_4 = h - 2m(C + \xi a)$$

and, $m = 1, 3, 5 \ldots\ldots$

This expression will reduce to that obtained by Preston and Reece [5.3], by putting,

$$\xi = 1$$

and $a = \frac{h - 2C}{2}$

5.2.2 The mathematical model

A general multi-region model is considered. The model is taken to be a set of planar regions infinite in both the longitudinal and transverse directions. The current sheet excitation takes the form described above and is considered to be infinitesimally thin and situated in the plane $z = i$.

In order to make the problem tractable, the resistivity in the z direction is assumed to be infinite. This means that it is tacitly assumed that the conducting regions are formed from infinitely thin insulated layers. Displacement currents are assumed to be negligible and magnetic saturation is neglected.

Maxwell's equations for any region in the model are:

$$\text{curl } H = J \quad \ldots\ldots (5.3) \qquad \text{curl } E = -\frac{\partial B}{\partial t} \quad \ldots\ldots (5.4)$$

$$\text{div } B = 0 \quad \ldots\ldots (5.5) \qquad \text{div } J = 0 \quad \ldots\ldots (5.6)$$

$$\text{div } E = 0 \quad \ldots\ldots (5.7) \qquad J = \sigma E \quad \ldots\ldots (5.8)$$

$$B = \mu H \quad \ldots\ldots (5.9)$$

and from initial assumptions we have,

$$J_z = 0 \qquad \ldots\ldots\ldots\ldots\ldots\ldots\ldots\ldots\ldots\ldots (5.10)$$

The boundary conditions are:

(a) The normal component of flux density B_z is continuous across a boundary.

b) The longitudinal component of magnetic field strength H_y is continuous across a boundary, but allowance must be made for the current sheet, in the manner shown in Section (5.2.4).

(c) The transverse component of electric field strength E_x is continuous across a boundary.

(d) All field components disappear at $z = \mp\infty$.

5.2.3 The field equations

The field components of a general region are first derived. This is done in terms of the n^{th} longitudinal harmonic and the m^{th} transverse harmonic. Whilst the field terms strictly speaking should be written with subscripts, say in the form $E_{x,n,m}$, the last two subscripts are omitted for shortness and the term written as simply E_x. All the fields vary as $\exp\left[j(\omega t - k_n y)\right]$ and this factor is omitted from all the field expressions which follow.

We have from equations (5.1) and (5.8),

$$E_x = \hat{E}_x \cos\left(\frac{m\pi x}{h} \right) \qquad \ldots\ldots\ldots\ldots\ldots\ldots\ldots(5.11)$$

Using equations (5.6), (5.8) and (5.11) it is shown in Appendix (5.7.2) that,

$$E_y = \hat{E}_y \sin\left(\frac{m\pi x}{h} \right) \qquad \ldots\ldots\ldots\ldots\ldots\ldots\ldots(5.12)$$

and $$\hat{E}_y = j\,\frac{m\pi}{hk_n}\,\hat{E}_x \qquad \ldots\ldots\ldots\ldots\ldots\ldots\ldots(5.13)$$

Appendix (5.7.2) further shows that,

$$E_x = \left[A \cosh(\varepsilon z) + D \sinh(\varepsilon z)\right] \cos\left(\frac{m\pi x}{h}\right) \text{..(5.14)}$$

where, $\varepsilon^2 = k_n^2 + \left(\frac{m\pi}{h}\right)^2 + jS_n\omega\mu\sigma$ ....(5.15)

A and D are arbitrary constants to be determined from the boundary conditions.

Using equations (5.4), (5.11), (5.12) and (5.13), Appendix (5.7.3) shows that,

$$H_z = \frac{-1}{\omega\mu} \left[\frac{\left(\frac{m\pi}{h}\right)^2 + k_n^2}{k_n}\right] E_x \quad \text{....................(5.16)}$$

The Appendix further shows that,

$$H_y = \hat{H}_y \cos\left(\frac{m\pi x}{h}\right) \quad \text{........................(5.17)}$$

$$\hat{H}_y = \frac{jk_n}{\left(\frac{m\pi}{h}\right)} \hat{H}_x \quad \text{........................(5.18)}$$

$$H_x = \left(\frac{m\pi}{hk_n}\right) \frac{\varepsilon}{\omega\mu} \left[A \sinh(\varepsilon z) + D \cosh(\varepsilon z)\right] \text{Sin}\left(\frac{m\pi x}{h}\right)$$

$$\text{........................(5.19)}$$

From equations (5.17),(5.18) and (5.19),

$$H_y = \frac{j\varepsilon}{\omega\mu}\left[A \sinh(\varepsilon z) + D \cosh(\varepsilon z)\right] \cos\left(\frac{m\pi x}{h}\right) \qquad \text{...............(5.20)}$$

5.2.4 Field calculations at the region boundaries

Fig. (5.3a) shows a general region L where $E_{x,L}$ and $H_{y,L}$ are the field components at the upper boundary of the region and $E_{x,L-1}$ and $H_{y,L-1}$ are the equivalent values at the lower boundary.

From equations (5.14) and (5.20),

$$E_{x,L} = \left[A \cosh(\varepsilon_L z_L) + D \sinh(\varepsilon_L z_L)\right] \cos\left(\frac{m\pi x}{h}\right) \qquad \text{...............(5.21)}$$

$$H_{y,L} = \frac{-j\varepsilon_L}{\omega\mu_L}\left[A \sinh(\varepsilon_L z_L) + D \cosh(\varepsilon_L z_L)\right] \cos\left(\frac{m\pi x}{h}\right) \qquad \text{...............(5.22)}$$

Equivalent expressions for $E_{x,L-1}$ and $H_{y,L-1}$ can be formed by replacing z_L in the above equations by z_{L-1}.

Now, for regions when $L \neq 1$ or N, we can put,

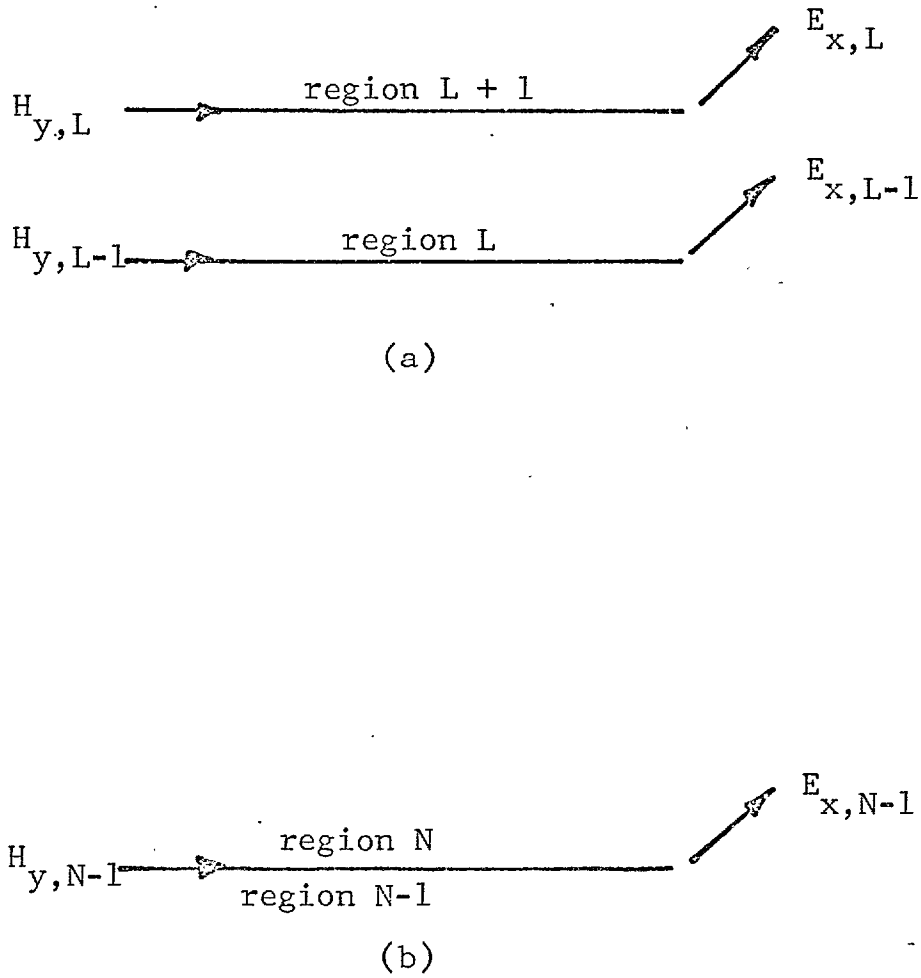

Fig. 5.3 Illustrating the regions in the analysis

(a) A general region L
(b) The conditions at the $N^{\underline{th}}$ region boundary

$$\begin{bmatrix} E_{x,L} \\ H_{y,L} \end{bmatrix} = \begin{bmatrix} T_L \end{bmatrix} \begin{bmatrix} E_{x,L-1} \\ H_{y,L-1} \end{bmatrix} \qquad \ldots\ldots\ldots\ldots\ldots\ldots\ldots(5.23)$$

where $\begin{bmatrix} T_L \end{bmatrix}$ is the transfer matrix (5.5) (5.9) for region L and is given by,

$$\begin{bmatrix} T_L \end{bmatrix} = \begin{bmatrix} a_L & b_L \\ c_L & d_L \end{bmatrix} \qquad \ldots\ldots\ldots\ldots\ldots\ldots\ldots\ldots\ldots(5.24)$$

Expressions for a_L, b_L, c_L and d_L are derived in Appendix (5.7.4).

This transfer matrix can be used to find the values of E_x and H_y at the upper boundary of a region from the equivalent values at the lower boundary.

If no excitation exists at the boundary say between regions a and b, then from the continuity of E_x and H_y at this boundary the fields at the upper boundary of region a may be found from those at the lower boundary of region b by successive application of the transfer matrix.

Considering the current sheet to be at z = i, then,

$$H'_{y,L} = H_{y,L} \qquad \text{when } L \neq i \qquad \ldots\ldots\ldots\ldots(5.25)$$

and $$H'_{y,L} = H_{y,L} - J_x \qquad \text{when } L = i \qquad \ldots\ldots\ldots\ldots(5.26)$$

where, $H_{y,L}$ is the longitudinal magnetic field strength immediately below a boundary,

and, $H'_{y,L}$ is the longitudinal magnetic field strength immediately above a boundary.

Bearing in mind the boundary conditions, it is apparent then that for the model considered, we can write,

$$\begin{bmatrix} E_{x,N-1} \\ \\ H_{y,N-1} \end{bmatrix} = \begin{bmatrix} T_{N-1} \end{bmatrix} \begin{bmatrix} T_{N-2} \end{bmatrix} \cdots\cdots \begin{bmatrix} T_{i+1} \end{bmatrix} \begin{bmatrix} E_{x,i} \\ \\ H_{y,i}-J_x \end{bmatrix} \qquad \ldots\ldots\ldots\ldots\ldots\ldots\ldots\ldots(5.27)$$

and,

$$\begin{bmatrix} E_{x,i} \\ \\ H_{y,i} \end{bmatrix} = \begin{bmatrix} T_i \end{bmatrix} \begin{bmatrix} T_{i-1} \end{bmatrix} \cdots\cdots \begin{bmatrix} T_2 \end{bmatrix} \begin{bmatrix} E_{x,1} \\ \\ H_{y,1} \end{bmatrix} \qquad \ldots\ldots(5.28)$$

If region N is now considered (Fig. (5.3b)), then, as $z \longrightarrow \infty$

$$\exp(\varepsilon z) \longrightarrow \infty$$

Therefore, from equations (5.21) and (5.22),

$$A = -D$$

$$E_{x,N-1} = A \exp(-\varepsilon_N z_{N-1}) \cos(\frac{m\pi x}{h}) \quad \text{..............(5.29)}$$

and, $$H_{y,N-1} = \frac{-j\varepsilon_N}{\omega\mu_N} A \exp(-\varepsilon_N z_{N-1}) \cos(\frac{m\pi x}{h}) \quad \text{........(5.30)}$$

Considering region (1) we have, as $z \longrightarrow -\infty$

$$\exp(-\varepsilon z) \longrightarrow \infty$$

Therefore, from equations (5.21) and (5.22),

$$A = D$$

$$E_{x,1} = A \exp(\varepsilon_1 z_1) \cos(\frac{m\pi x}{h}) \quad \text{..................(5.31)}$$

and $$H_{y,1} = \frac{j\varepsilon_1}{\omega\mu_1} A \exp(\varepsilon_1 z_1) \cos(\frac{m\pi x}{h}) \text{..............(5.32)}$$

The field components at the boundaries of regions 1 and N still contain an arbitrary constant A. The ratios, however, of E_x to H_y at these boundaries contain no arbitrary constants and it is only these ratios that are needed for a complete solution. The next section shows how this may be accomplished. The ratios of E_x to H_y have been termed the surface impedance (5.6) (5.10)(5.11)(5.12)(5.13)(5.14).

5.2.5 Surface impedance calculations

The surface impedance looking upward at a boundary $z = \psi$ is defined as,

$$Z_{\psi+1} = \frac{E_{x,\psi}}{H'_{y,\psi}} \qquad \text{.............................(5.33)}$$

and the surface impedance looking downward is,

$$Z_{\psi} = -\frac{E_{x,\psi}}{H_{y,\psi}} \qquad \text{.............................(5.34)}$$

Thus from equations (5.33) and (5.25),

$$Z_N = \frac{E_{x,N-1}}{H_{y,N-1}} \qquad \text{.............................(5.35)}$$

Substituting for $E_{x,N-1}$ and $H_{y,N-1}$ from equations (5.29) and (5.30) respectively,

$$Z_N = \frac{j\omega\mu_N}{\varepsilon_N} \qquad \text{.............................(5.36)}$$

This gives the surface impedance of the N^{th} region uniquely since it contains no arbitrary constants.

The surface impedance of the other regions going towards the current sheet may now be calculated successively using the following expressions.

From Appendix (5.7.5),

$$Z_{N-1} = \frac{b_{N-1} - d_{N-1} Z_N}{c_{N-1} Z_N - a_{N-1}} \qquad \text{.............. ......(5.37)}$$

Similarly,

$$\begin{aligned} Z_{N-2} &= \frac{b_{N-2} - d_{N-2} Z_{N-1}}{c_{N-2} Z_{N-1} - a_{N-2}} \\ &\;\vdots \\ Z_{i+1} &= \frac{b_{i+1} - d_{i+1} Z_{i+2}}{c_{i+1} Z_{i+2} - a_{i+1}} \end{aligned} \qquad \text{....................(5.38)}$$

The surface impedance looking downwards from the current sheet can be calculated as follows,

from equation (5.34),

$$Z_1 = \frac{-E_{x,1}}{H_{y,1}} \qquad \text{.............................(5.39)}$$

Substituting for $E_{x,1}$ and $H_{y,1}$ from equations (5.31) and (5.32) respectively,

$$Z_1 = \frac{j\omega\mu_1}{\varepsilon_1} \qquad \text{..............................(5.40)}$$

Again this now contains no arbitrary constants and a similar chain of calculations can be performed to find Z_i.

From Appendix (5.7.5),

$$Z_2 = \frac{b_2 - a_2 Z_1}{c_2 Z_1 - d_2} \qquad \text{.......... ....(5.41)}$$

and hence

$$Z_i = \frac{b_i - a_i Z_{i-1}}{c_i Z_{i-1} - d_i} \qquad \text{.......................(5.42)}$$

The input surface impedance at the current sheet, Z_{in}, is given by the effective impedance of a parallel combination of Z_i and Z_{i+1}.

Hence,
$$Z_{in} = \frac{Z_i Z_{i+1}}{Z_i + Z_{i+1}} \qquad \text{.......................(5.43)}$$

Substituting for Z_i and Z_{i+1} using equations (5.34) and (5.33) respectively, and rearranging,

$$Z_{in} = \frac{- E_{x,i}}{H_{y,i} - H'_{y,i}} \qquad \text{.......... ....(5.44)}$$

From equation (5.26),

$$H'_{y,i} = H_{y,i} - J_x$$

Substituting this in equation (5.44),

$$Z_{in} = \frac{-E_{x,i}}{J_x}$$

Thus, the input impedance at the current sheet has been determined. This means that using the relationship,

$$E_{x,i} = - J_x \, Z_{in} \qquad \text{........................(5.45)}$$

all the field components can be found by making use of equations (5.45), (5.42), (5.34), (5.27) and (5.28).

5.2.6 Power calculations

The time average power flowing through a boundary is given by the equation,

$$P = \mathcal{R}\left[\frac{1}{h} \int_{o}^{h/2} (\hat{E}_x \, \hat{H}^*_y \, \mathrm{Cos}^2(\frac{m\pi x}{h}) - \hat{E}_y \, \hat{H}^*_x \, \mathrm{Sin}^2(\frac{m\pi x}{h}))dx\right] \mathrm{W/m}^2$$

$$\text{........................(5.46)}$$

Substituting for $\hat{E}_y$ and $\hat{H}^*_x$ from equations (5.13) and (5.18) respectively, and integrating,

$$P = 0.25\left[1 + \left(\frac{m\pi}{hk_n}\right)^2\right] \mathcal{R}\,(\hat{E}_x\ \hat{H}^*_y) \quad W/m^2 \text{..............(5.47)}$$

Now, at the current sheet, the powers flowing upward and downward are given by the equations,

$$P_{in,up} = 0.25h\left[1 + \left(\frac{m\pi}{hk_n}\right)^2\right] \mathcal{R}\,(\hat{E}_{x,i}\ \hat{H}'^*_{y,i}) \quad W/m$$

$$P_{in,down} = -0.25h\left[1 + \left(\frac{m\pi}{hk_n}\right)^2\right] \mathcal{R}\,(\hat{E}_{x,i}\ \hat{H}^*_{y,i}) \quad W/m$$

Thus, the total power flowing from the current sheet P_{in} is given by the equation,

$$\begin{aligned} P_{in} &= P_{in,up} + P_{in,down} \\ &= 0.25h\left[1 + \left(\frac{m\pi}{hk_n}\right)^2\right] \mathcal{R}\left[\hat{E}_{x,i}(\hat{H}'^*_{y,i} - \hat{H}^*_{y,i})\right] \quad W/m \end{aligned}$$

This expression may be written in terms of the input surface impedance, whence substituting for $\hat{H}'^*_{y,i}$ and $\hat{E}_{x,i}$ from equations (5.26) and (5.45) respectively, and rearranging,

$$P_{in} = 0.25h\left[1 + \left(\frac{m\pi}{hk_n}\right)^2\right] / J_x/^2 \mathcal{R}\,(Z_{in}) \quad W/m \quad \text{........(5.48)}$$

Inserting the harmonic subscripts, equation (5.48) becomes,

$$P_{in,n,m} = 0.25\ h \left[1 + \left(\frac{m\pi}{hk_n}\right)^2 \right] / J_{x,n,m} /^2 \mathcal{R}\,(Z_{in,n,m}) \quad \text{W/m} \qquad \ldots\ldots\ldots\ldots\ldots\ldots\ldots(5.49)$$

The traction force F_T is then given by,

$$F_T = \frac{A_r}{h} \sum_n \left[\frac{\sum_m P_{in,n,m}}{V_{Sn}} \right] \quad \text{Newtons} \qquad \ldots\ldots\ldots\ldots\ldots\ldots\ldots(5.50)$$

where A_r = rotor surface area

and, V_{Sn} = the synchronous speed for the $n^{\underline{th}}$ longitudinal harmonic

5.3 Equivalent circuits

It is interesting to look at the results of the multi-layer theory in terms of equivalent circuits. The theory has been developed for the case of a constant excitation current and the complex power flow found is equivalent in conventional machine terms to the power flow into a parallel combination of magnetising reactance and rotor impedance referred to the stator.

The surface impedance (calculated by taking the summed complex power into the machine at any slip) can be regarded as a simple series circuit. Any circuit may be considered to be equivalent to this provided its complex power intake is the same. Now the magnetising reactance of a machine may be considered to be the usual conventional value converted to surface terms. Thus if this is computed it may be used as the "magnetising impedance" shunt component in an equivalent circuit. The "rotor branch" of which may be computed so that the complex power into the equivalent circuit is the same as the original summation from the layer theory. Thus if the surface impedance into the complete machine is Z, and the conventional value of magnetising reactance converted to surface terms is X_{ms}, then the equivalent circuit is formed from a parallel combination of X_{ms} and $Z_r = ZX_{ms}/(X_{ms} - Z)$.

In conventional terms but using surface values:

$$R_{2S} = \Re(Z_r)$$

and $$X_{2S} = \Im(Z_r)$$

X_{ms} may be calculated as follows.

The rotor coupled time constant referred to in the simple transient analysis (chapter 3) is,

$$T = \frac{P_\omega^2 \mu_o}{\pi^2 \rho_r g}$$

Now this term is the same as $X_{ms}/(\omega \rho_r)$,

thus, $$X_{ms} = \frac{\omega P_\omega^2 \mu_o}{\pi^2 g}$$

Recalling chapter 3, it will be remembered that the design procedure recommended in reference (5.15) was to calculate the effective rotor resistivity by using the Russell and Norsworthy (5.1) factor. This then was used in the same way as the factor R_{2S} given above and may be used for comparison purposes with the new analysis.

There has been no rigorous method to date of calculating X_{2S} for a sheet rotor and the early transient analysis assumed it to be zero. Much of the linear motor design work performed, at least in this country, has either used empirical formulae for X_{2S} or has neglected its effect.

Linear motors for high speed traction purposes using 50 Hz supplies have dimensions and specifications of the order of those given below:

pole number	=	4
winding pole pitch	=	1.4 m
stator width	=	.3 m
plate width	=	.4 to .6 m
clearance	=	.04 m
plate thickness	=	.007 m
plate material		aluminium

The variations of R_{2S} and X_{2S} as the plate width is increased are shown on Figs. (5.4) and (5.5). The value of R'_{2S} using the simple approach is also shown as a dotted line on Fig. (5.4) for comparison.

5.4 Voltage calculations

From equation (5.49)the complex harmonic power input may be written as,

$$P_{inc,n,m} = 0.25\ A_r \left[1 + \left(\frac{m\pi}{hk_n}\right)^2\right] /J_{x,n,m}/^2\ Z_{in,n,m} \qquad \text{watts}$$

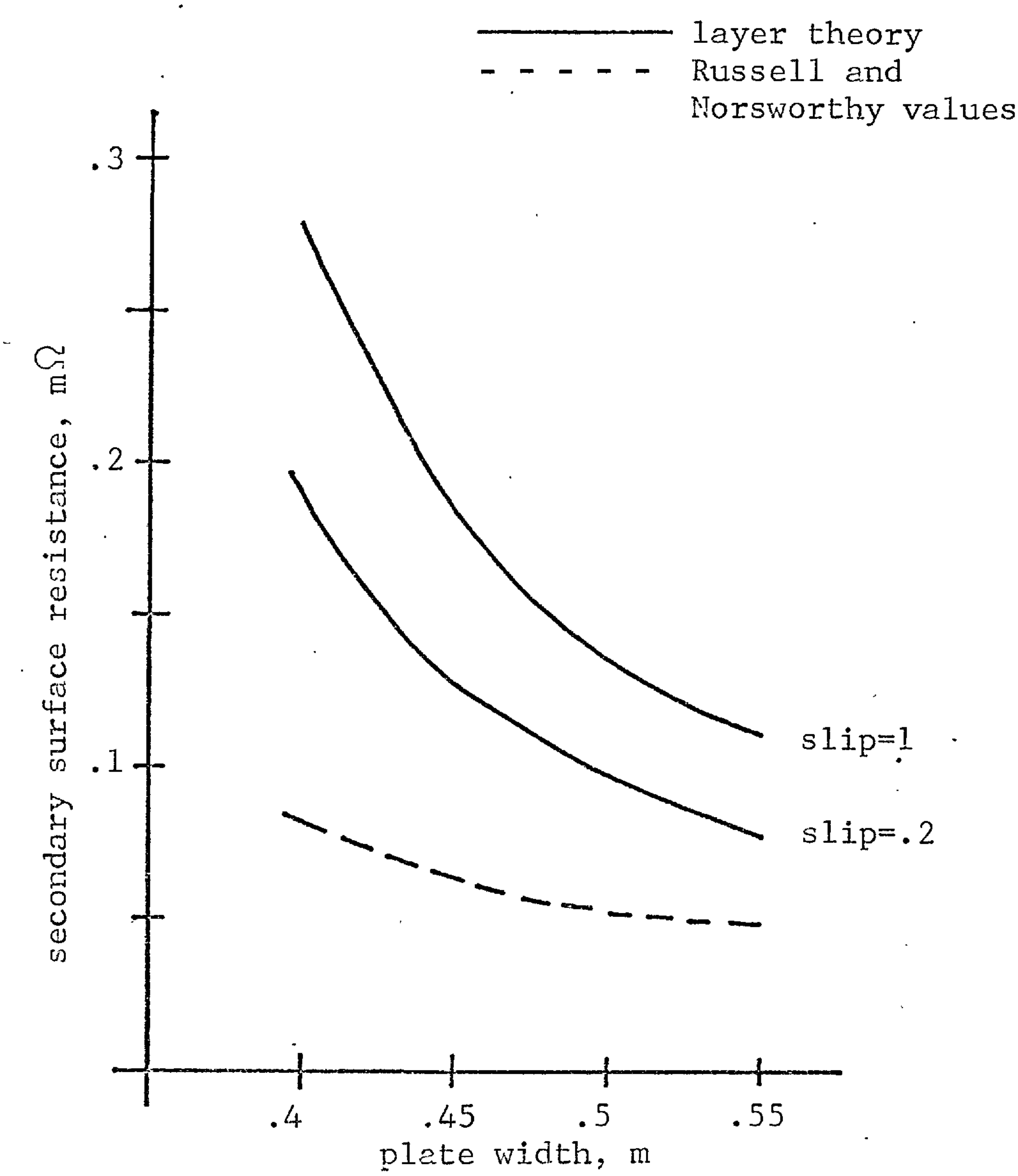

Fig. 5.4 Theoretical secondary surface resistance values

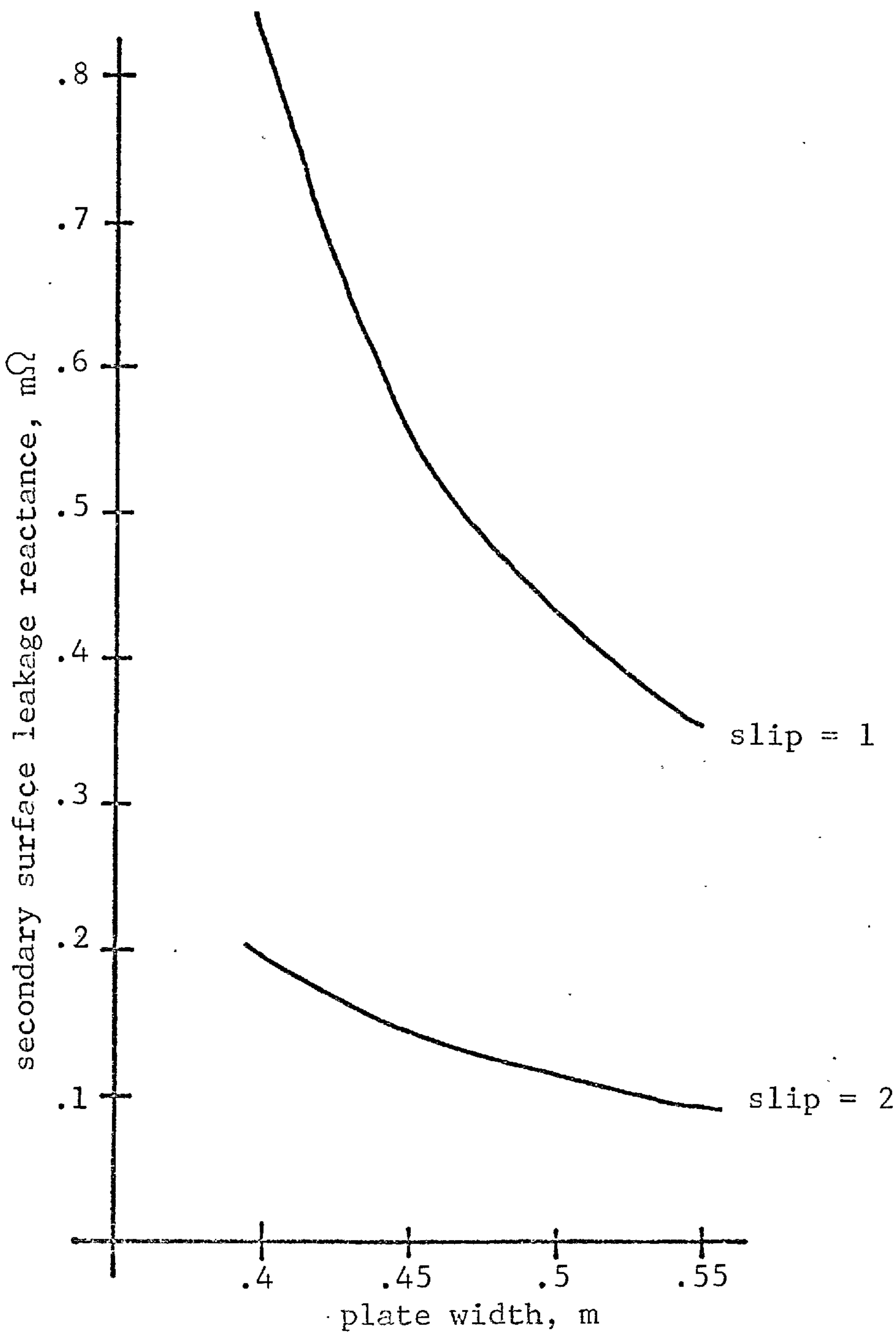

Fig. 5.5 Theoretical secondary surface leakage reactance calculations.

where A_r is the rotor surface area.

Now, the total input power is,

$$P_T = \sum_n \sum_m \mathcal{R}(P_{inc,n,m})$$

and the total reactive power is,

$$Q_T = \sum_n \sum_m \mathcal{J}(P_{inc,n,m})$$

Knowing P_T and Q_T, the terminal voltage may be calculated in the same manner as that in section 3.3.3 of chapter 3.

5.5 Experimental results

5.5.1 Experiments with continuous stator iron

An experimental model was provided by making a "plate rotor" for the previously described "patch excitation" machine. The aluminium plate rotor had a plate axial length of 26.5 cms. so that it protruded 4.15 cms. beyond the rotor core iron at each side. The plate thickness was 1.27 cms. and the clearance between the upper surface of the plate and the stator iron was 0.635 cms. These dimensions give an effective main time constant of the same order as that obtained from the squirrel-cage rotor, when the machine was excited from a 200 Hz supply.

Fig. (5.6) compares the theoretical and practical values of torque; it will be noted that the agreement is good. However, when the predicted voltage was computed using the measured value of stator impedance it was found that the agreement was only approximate. Now the measured value of stator impedance previously (in the squirrel-cage rotor case) provided good agreement between theory and practice. However, it is apparent that the model used for the layer theory allows coupling between the stator end winding and the secondary plate. This coupling will exist in practice in the plate rotor machine but will not exist practically in the squirrel-cage arrangement where the end-rings were of very limited axial length. The coupling will effectively reduce the stator end winding leakage in the plate rotor case. However, a calculation of this effect would be extremely complicated and could probably be done only by the continuous lines show theoretical results uniform gap case

o-o-o-o-o experimental results for the uniform gap case

X-X-X-X-X experimental results for the arc-stator

-·-·-·-·- theoretical voltage prediction with modified stator impedance

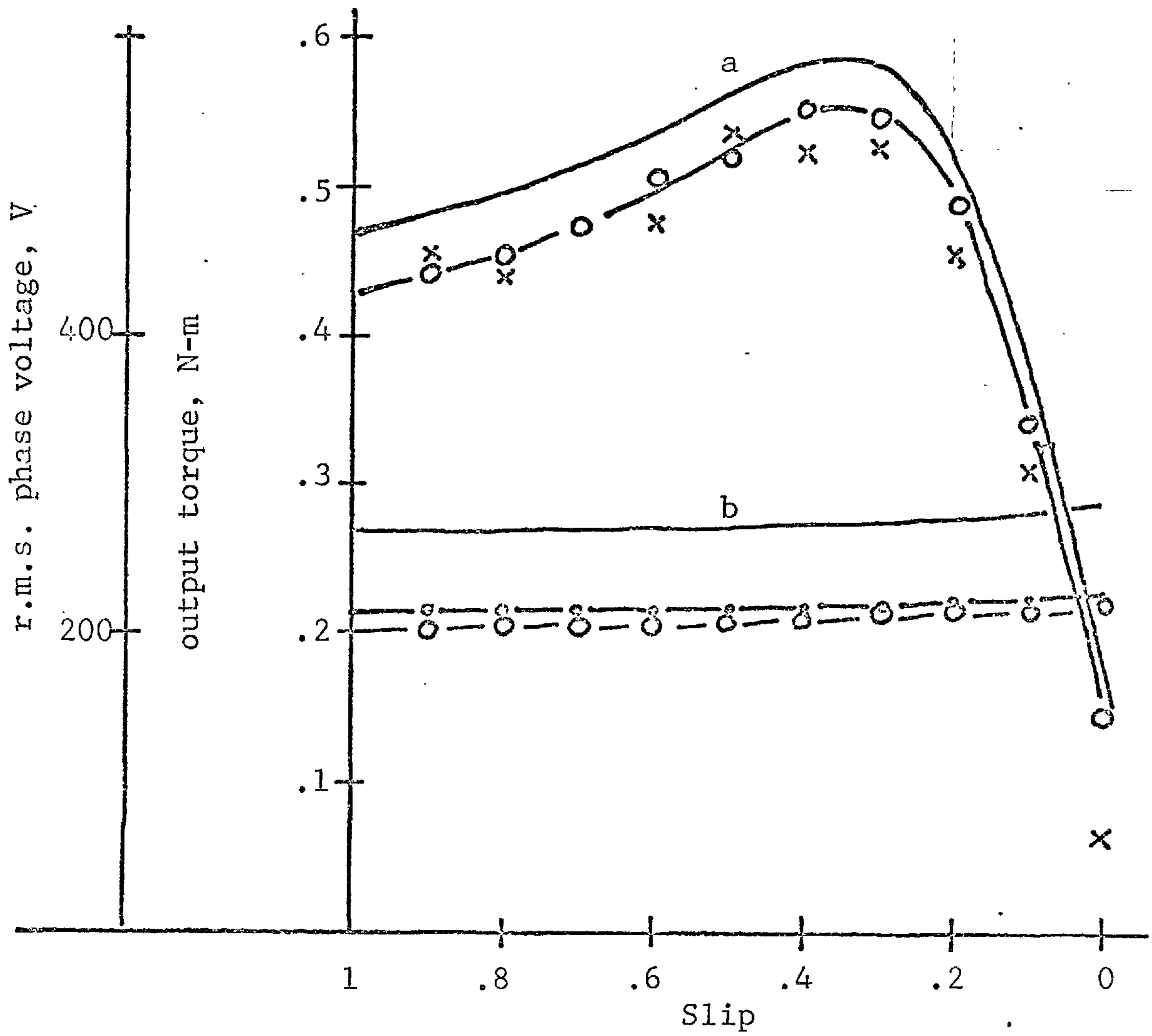

Fig. 5.6 Comparison between predicted results using the multi-layer analysis and experimental values.

(a) torque
(b) voltage

use of a purely numerical method. In the absence of this an empirical approach can be made by assuming that a fraction of the measured stator leakage reactance is effective. Fig. (5.6) shows the result of using 75% of the leakage reactance and in this particular case good agreement is obtained.

Fig. (5.7) shows the measured total flux profile measured using the search coils described in the previous chapters. Theoretical values are also shown and it will be observed that the agreement is generally good.

5.5.2 Experiments with an arc-stator

In chapter 3 the arc-stator arrangement has been described. This arrangement was used again with the plate-rotor described above. Torque-speed curves only were taken and it will be observed from Fig. (5.6) that practically no difference exists between the results obtained for continuous iron and those obtained using the arc-stator. Thus whilst the exit-edge loss should have been calculated for the arc-stator case in the manner described in chapter 3, this has not been done on the grounds that the results for torque are practically indistinguishable.

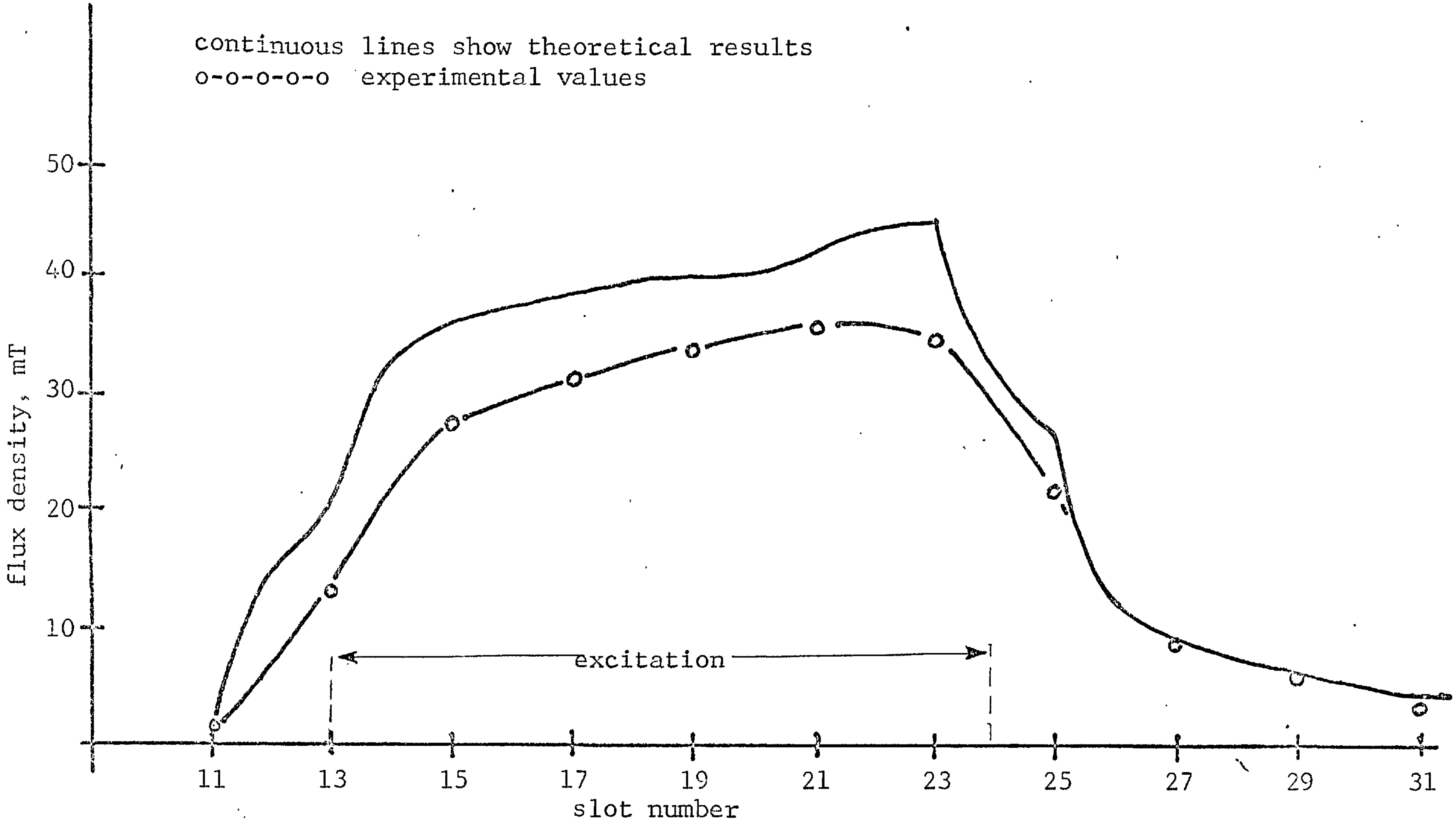

Fig. 5.7 Flux profiles for the sheet rotor motor, at synchronous speed

5.6 Conclusions

The analysis presented in this chapter has been shown to provide excellent correlation with practical results as far as the prediction of the force produced at particular current loading is concerned.

The prediction of input voltage has been shown to be more difficult. In particular the effects of coupling between the stator end windings and the rotor plate give rise to a reduced effective stator leakage reactance. Future work should include the prediction of the effective stator leakage reactance to help account for these effects.

5.7 Appendices

5.7.1 Fourier Analysis of the excitation current sheet in the transverse direction

Fig. (5.2) shows the transverse variation of the current sheet. It can be seen from the figure that the variation represents a symetrical even function of x.

Using Fourier Analysis, this variation may be represented by a series of harmonic components,

$$C_{1m} \cos\left(\frac{m\pi x}{h}\right) \qquad \ldots\ldots\ldots\ldots\ldots\ldots\ldots\ldots\ldots\ldots (5.51)$$

where,

$$C_{1m} = \frac{2}{h} \int_{o}^{h} F(x) \cos\left(\frac{m\pi x}{h}\right) dx$$

The values of F(x) are shown on the figure for the range considered in the integration.

Performing the integration,

$$C_{1m} = \frac{4}{\pi} \left[\frac{1}{m} \sin\left[\frac{m\pi}{h}(C + \xi a) \right] \right] - (A_1 + A_2) \cos\left(\frac{m\pi C}{h}\right)$$

$$+ A_1 \cos\left(\frac{\pi A_3}{2h}\right) + A_2 \cos\left(\frac{\pi A_4}{2h}\right) \qquad \ldots\ldots\ldots\ldots (5.52)$$

$m = 1, 3, 5 \ldots\ldots$

and $C_{1m} = 0$ for $m = 2, 4, 6 \ldots\ldots$

$$A_1 = \frac{\xi a}{h + 2m\xi a}$$

$$A_2 = \frac{\xi a}{h - 2m\xi a}$$

$$A_3 = h + 2m(C + \xi a)$$

$$A_4 = h - 2m(C + \xi a)$$

5.7.2 Derivation of the electric field strength

From equation (5.6),

$$\text{div } J = \frac{\partial J_x}{\partial x} + \frac{\partial J_y}{\partial y} + \frac{\partial J_z}{\partial z} = 0$$

$$J_z = 0 \text{ because } \sigma_z = 0$$

Then, assuming $\sigma_x = \sigma_y = \sigma$, using equations (5.8) and (5.11),

$$\hat{E}_y = \frac{jm\pi}{hk_n}\hat{E}_x \qquad \ldots\ldots\ldots\ldots\ldots\ldots\ldots\ldots(5.53)$$

and $$E_y = \hat{E}_y \sin\left(\frac{m\pi x}{h}\right) \qquad \ldots\ldots\ldots\ldots\ldots\ldots\ldots\ldots(5.54)$$

From equations (5.4) and (5.9),

$$(\text{curl curl } E)_x = -jS_n\omega\mu \ \ (\text{curl } H)_x$$

Then substituting for curl H from equation (5.3) and using equation (5.8),

$$(\text{curl curl } E)_x = -jS_n\omega\mu\,\sigma\, E_x$$

Then using equations (5.7) and (5.11),

$$\frac{\partial^2 E_x}{\partial z^2} - \varepsilon^2 E_x = 0$$

where $\varepsilon^2 = k_n^2 + (\frac{m\pi}{h})^2 + jS_n\omega\mu\,\sigma$

Thus the general solution for E_x is,

$$E_x = \Big[A \cosh(\varepsilon z) + D \sinh(\varepsilon z)\Big] \cos(\frac{m\pi x}{h}) \quad \ldots\ldots\ldots(5.55)$$

5.7.3 <u>Derivation of the magnetic field strength</u>

From equation (5.4),

$$(\text{curl } E)_z = -j\omega\mu H_z$$

Using equations (5.11), (5.12) and (5.13),

$$H_z = \frac{-1}{\omega\mu}\left[\frac{(\frac{m\pi}{h})^2 + k_n^2}{k_n}\right] E_x \qquad \text{...............(5.56)}$$

From equation(5.5),

$$\text{div } B = 0$$

and assuming $\mu_z = \mu_x = \mu$

$$\text{div } H = 0$$

That is, $\frac{\partial H_x}{\partial x} + \frac{\partial H_y}{\partial y} + \frac{\partial H_z}{\partial z} = 0$ ....(5.57)

From equations (5.16), (5.11) and (5.57),

$$H_x = \hat{H}_x \sin(\frac{m\pi x}{h}) \qquad \text{........................(5.58)}$$

$$H_y = \hat{H}_y \cos(\frac{m\pi x}{h}) \qquad \text{........................(5.59)}$$

From equations (5.3) and (5.10),

$$(\text{curl } H)_z = J_z = 0$$

That is, $\frac{\partial H_y}{\partial x} - \frac{\partial H_x}{\partial y} = 0$

Using equation (5.59),

$$\hat{H}_y = \frac{jk_n}{(\frac{m\pi}{h})} \cdot \hat{H}_x \qquad \text{......................(5.60)}$$

From equations (5.60),(5.58) and (5.57),

$$\hat{H}_x = \frac{1}{\omega\mu} \left(\frac{m\pi}{hk_n}\right) \frac{\partial \hat{E}_x}{\partial z}$$

Using equation (5.14),

$$H_x = \left(\frac{m\pi}{hk_n}\right) \frac{\varepsilon}{\omega\mu} \left[A \sinh(\varepsilon z) + D \cosh(\varepsilon z)\right] \sin\left(\frac{m\pi}{h}x\right)$$

$$\text{......................(5.61)}$$

5.7.4 Calculation of the transfer matrix elements

From equations (5.21), (5.22), (5.23) and (5.24),

$$a_L = \cosh(\varepsilon_L g_L) \qquad \text{......................(5.62)}$$

$$b_L = \frac{-j\omega\mu_L}{\varepsilon_L} \sinh(\varepsilon_L g_L) \qquad \text{......................(5.63)}$$

$$c_L = \frac{j\varepsilon_L}{\omega\mu_L} \sinh(\varepsilon_L g_L) \qquad \text{......................(5.64)}$$

$$d_L = \cosh(\varepsilon_L g_L) \qquad \text{......................(5.65)}$$

5.7.5 Surface impedance calculations

From equation (5.35),

$$Z_N = \frac{E_{x,N-1}}{H_{y,N-1}}$$

Substituting for $E_{x,N-1}$ and $H_{y,N-1}$ from equations (5.23) and (5.24),

$$Z_N = \frac{a_{N-1}\, E_{x,N-2} + b_{N-1}\, H_{y,N-2}}{c_{N-1}\, E_{x,N-2} + d_{N-1}\, H_{y,N-2}} \qquad \text{...............(5.66)}$$

Now, from equations (5.33) and (5.25),

$$Z_{N-1} = \frac{E_{x,N-2}}{H_{y,N-2}} \qquad \text{........................(5.67)}$$

Substituting for $E_{x,N-2}$ from equation (5.67) into equation (5.66),

$$Z_N = \frac{a_{N-1}\, Z_{N-1} + b_{N-1}}{c_{N-1}\, Z_{N-1} + d_{N-1}}$$

Rearranging this,

$$Z_{N-1} = \frac{b_{N-1} - d_{N-1}\, Z_N}{c_{N-1}\, Z_N - a_{N-1}} \qquad \text{........................(5.68)}$$

From equation (5.34),

$$Z_2 = \frac{-E_{x,2}}{H_{y,2}}$$

Substituting for $E_{x,2}$ and $H_{y,2}$ from equations (5.23) and (5.24),

$$Z_2 = -\frac{a_2 E_{x,1} + b_2 H_{y,1}}{c_2 E_{x,1} + d_2 H_{y,1}}$$

Substituting for $E_{x,1}$ from equation (5.39) and rearranging,

$$Z_2 = \frac{b_2 - a_2 Z_1}{c_2 Z_1 - d_2} \qquad \text{.........................(5.69)}$$

CHAPTER SIX

REFERENCES

2.1 NIX, G.F. and LAITHWAITE, E.R.: 'Linear induction motors for low-speed and standstill application', Proc. IEE, June, 1966, 113, (6), pp. 1044-1056.

2.2 LAITHWAITE, E.R., EASTHAM, J.F., BOLTON, H.R. and FELLOWS, T.G.: 'Linear motors with transverse flux', ibid, Dec. 1971, 118, (12), pp. 1761-1767.

2.3 WELLS, A.: 'Library program to calculate Bessel functions of general complex argument', King's College Computer Unit Program Library, 1969.

2.4 PIPES, L.A.: 'Matrix theory of skin effect in laminations', J. Franklin Inst., 1956, 262, pp. 127-138.

2.5 GREIG, J. and FREEMAN, E.M.: 'Travelling-wave problem in electrical machines', Proc. IEE, Nov. 1967, 114, (11), pp. 1681-1683.

2.6 CULLEN, A.L. and BARTON, T.H.: 'A simplified electromagnetic theory of the induction motor, using the concept of wave impedance', ibid, 1959, 105C, pp. 331-336.

2.7 POSTNIKOV, I.M.: 'Calculation of the electromagnetic travelling field in a lamellar conducting medium', Elektrichestvo, 1965, 9, pp. 1-7.

2.8 KUYPER, W.W.: 'Pole-face losses in solid rotor turbine generators', Trans. Amer. Inst. Elect. Engrs., 1943, 62, pp. 827-834.

2.9 BARLOW, H.E.M. and TAY, E.S.: 'Power measurement at 10 Mc/s by absorption of the angular momentum of a rotating field', Proc. IEE, 1966, 113, (7), pp. 1253-1255.

2.10 LEVI, E.L. and PANZER, M.: 'Electromechanical power conversion' (McGraw-Hill, 1967).

2.11 FREEMAN, E.M.: 'Travelling waves in induction machines: input impedance and equivalent circuits', Proc. IEE. Dec. 1968, 115, (12), pp. 1772-1776.

2.12 FREEMAN, E.M. and SMITH, B.E.: 'Surface-impedance method applied to multi-layer cylindrical induction devices with circumferential exciting currents', ibid, Oct, 1970, 117, (10), pp. 2012-2013.

2.13 PRESTON, T.W. and REECE, A.B.J.: 'Transverse edge effects in linear induction motors', ibid, June 1969, 116, (6), pp. 973-979, corrigend, 1970, 117, (9), p. 1808.

2.14 FREEMAN, E.M. and LOWTHER, D.A.: 'Transverse edge effects in linear induction motors', ibid, Dec. 1971, 118, (12), pp. 1820-1821.

3.1 SHTURMAN, G.I.: 'An induction motor with an open magnetic circuit', Elektrichestvo, 1946, No. 10, 43 (1946).

3.2 SHTURMAN, G.I. and ATONOV, R.L.: ' "Edge effect" in induction motors with open magnetic field', ibid, No. 2, 54 (1947).

3.3 REZIN, M.G.: 'Armature reaction effects and the mechanical characteristics of a motor with an arc- shaped stator', ibid, 1950, No. 2., p. 51.

3.4 REZIN, M.G.: 'Some peculiarities of the electromagnetic phenomena in a motor with an arc-shaped stator', ibid, 1951, No. 6, p. 25.

3.5 WILLIAMS, F.C., LAITHWAITE, E.R., EASTHAM, J.F. and FARRER, W.: 'Variable-speed induction motors using phase-shift control', Proc. IEE, 108(A), 100 (1961).

3.6 WILLIAMS, F.C., LAITHWAITE, E.R. and PIGGOTT, L.S.: 'Brushless variable speed induction motors', ibid, paper no. 2097, June, 1956 (104A, pp. 102-118).

3.7 WILLIAMS, F.C., LAITHWAITE, E.R. and EASTHAM, J.F.: 'Development and design of spherical induction motors', ibid, paper no. 3036U , Dec. 1959 (106A, pp. 471-484).

3.8 WILLIAMS, F.C., LAITHWAITE, E.R.,EASTHAM, J.F. and PIGGOTT, L.S.: 'The logmotor - a cylindrical brushless variable speed motor', ibid, paper no. 3149U , February 1960 (108A).

3.9 SADLER, G.V. and DAVEY, A.W.: 'Applications of linear induction motors in industry', ibid, vol. 118, no. 6, June 1971, pp. 765-776.

3.10 NIX, G.F. and LAITHWAITE, E.R.: 'Linear induction motors for low-speed and standstill application', Proc. IEE, June 1966, No. 6, pp. 1044-1056.

3.11 U.S. Department of Transportation Study Contract C-145-66/NEG, final report June 1967.

3.12 LAITHWAITE, E.R. and BARWELL, F.T.: 'Application of linear induction motors to high-speed transport system', Proc. IEE, May 1969, No. 5, pp. 713-724.

3.13 BARWELL, F.T. and LAITHWAITE, E.R.: 'Application of the linear induction motors to high-speed transport', Proc. Inst. Mech. Engrs., 1966-67, 181, (3G), (Paper to Convention on Guided Land Transport, 28th Oct. 1966).

3.14 BLAKE, L.R.: 'Conduction and induction pumps for liquid metals', Proc. IEE, Vol. 104A, pp. 49-63, 1967.

3.15 WATT, D.A.: 'The design of electromagnetic pumps for liquid metals', ibid, vol. 106A, pp. 94-103, 1958.

3.16 LAITHWAITE, E.R.: 'Development and new applications of induction motors', Ph.D. Thesis, University of Manchester, 1956.

3.17 TIPPING, D.: 'The analysis of some special-purpose electrical machines', Ph.D. Thesis, University of Manchester, 1964.

3.18 CULLEN, A.L. and BARTON, T.H.: 'A simplified electromagnetic theory of the induction motor, using the concept of wave impedance', Proc. IEE, 1959, 105C, pp. 331-336.

3.19 HESMONDHALGH, D.E. and TIPPING, D.: 'General method for prediction of the characteristics of induction motors with discontinuous exciting windings', Proc. IEE, Vol. 112, no. 9, Sept. 1965, pp. 1721-1733.

3.20 LAITHWAITE, E.R.: 'Induction machines for special purposes', (George Newnes, 1966).

3.21 RUSSELL, R. and NORSWORTHY, K.H.: 'Eddy currents and wall losses in screened-rotor induction motors', Proc. IEE, paper no. 2525U, April 1958.

3.22 EASTHAM, J.F.: 'Behaviour of induction motors with discontinuous stators', M.Sc. Thesis, University of Manchester, 1958.

4.1 LAITHWAITE, E.R.: 'Induction machines for special purposes', (George Newnes, 1966).

4.2 ALTERNBERND, G., BAUSCH, H. and JORDAN, H.: 'Theorie des Einphaseninduktionsmotors mit abgestuftem Luftspalt', Acta Technico Čsav, No. 4, 1963, pp. 403-424.

5.1 RUSSELL, R. and NORSWORTHY, K.H.: 'Eddy currents and wall losses in screened-rotor induction motors', Proc. IEE, paper no. 2525U, April 1958.

5.2 BOLTON, H.: 'Transverse edge effect in sheet-rotor induction motors', ibid, May 1969, <u>116</u>, (5), pp. 725-731.

5.3 PRESTON, T.W. and REECE, A.B.J.: 'Transverse edge effects in linear induction motors', ibid, June 1969, <u>116</u>, (6), pp. 973-979, corrigend, 1970, <u>117</u>, (9), p. 1808.

5.4 VESKE, T.A.: 'Solution of the electromagnetic field equations for a plane linear induction machine with secondary boundary effects', Magnitnaya Gidrodinamika, vol. 1, no. 1, pp. 87-96, 1965.

5.5 GREIG, J. and FREEMAN, E.M.: 'Travelling-wave problem in electrical machines', Proc. IEE, Nov. 1967, <u>114</u>, (11), pp. 1681-1683.

5.6 FREEMAN, E.M.: 'Travelling waves in induction machines: input impedance and equivalent circuits', ibid, Dec. 1968, <u>115</u>, (12), pp. 1772-1776.

5.7 FREEMAN, E.M. and LOWTHER, D.A.: 'Transverse edge effects in linear induction motors', ibid, Dec. 1971, <u>118</u>, (12), pp. 1820-1821.

5.8 FREEMAN, E.M.: Brighton Polytechnic, private communication.

5.9 PIPES, L.A.: 'Matrix theory of skin effect in laminations', J. Franklin Inst., 1956, 262, pp. 127-138.

5.10 CULLEN, A.L. and BARTON, T.H.: 'A simplified electromagnetic theory of the induction motor, using the concept of wave impedance', Proc. IEE, 1959, 105C, pp. 331-336.

5.11 POSTNIKOV, I.M.: 'Calculation of the electromagnetic travelling field in a lamellar conducting medium,' Elektrichestvo, 1965, 9, pp. 1-7.

5.12 KUYPER, W.W.: 'Pole-face losses in solid rotor turbine generators', Trans. Amer. Inst. Elect. Engrs., 1943, 62, pp. 827-834.

5.13 LEVI, E.L. and PANZER, M.: 'Electromechanical power conversion', (McGraw-Hill, 1967).

5.14 BARLOW, H.E.M. and TAY, E.S.: 'Power measurement at 10 Mc/s by absorption of the angular momentum of a rotating field', Proc. IEE, 1966, 113, (7), pp. 1253-1255.

5.15 LAITHWAITE, E.R.: 'Induction machines for special purposes', (George Newnes, 1966).